Creating and Mapping an Urban Heat Island Index for California

CalEPA / Altostratus Inc. Agreement No. 13-001

Principal Investigator: Haider Taha, Altostratus Inc.

FINAL REPORT

Prepared for

Dr. William Dean
California Environmental Protection Agency
And
California Air Resources Board
Sacramento, California

Prepared by

Altostratus Inc.
Martinez, California

April 24, 2015

Haider Taha
Altostratus Inc.
Martinez, California

Travis Freed
Spatial Informatics Group
Pleasanton, California

Contract period: May 1st, 2014 through April 30th, 2015

Altostratus Inc. (contractor):
Tasks: Meteorological modeling, model input data, model modifications and customizations, model validation and performance evaluation, post-processing of meteorological output, definition of UHI reference points, extraction of meteorological fields at census tracts scale, calculations of the urban heat island and the urban heat-island index, meteorological and land-use data analysis, analysis of model results, technical notes, and final report.

Spatial Informatics Group LLC (sub-contractor):
Tasks: Generation of census-tract centroids, land-use/land-cover mapping and development of crosswalks among datasets, recasting USGS Level-II and NLCD datasets, remapping from native projections of LULC datasets to projections used in the models, mapping the urban heat island index onto census tracts, and generation of UHII maps.

DISCLAIMER

This work was supported by the California Environmental Protection Agency (CalEPA). The statements and conclusions in this report are those of the contractor and not necessarily those of the CalEPA. The mention of commercial products, their source, or their use in connection with material reported herein is not to be construed as actual or implied endorsement of such products.

ACKNOWLEDGEMENTS

Gina Solomon and William Dean (CalEPA) are acknowledged for leading this project, guiding its activities, and providing support and pivotal, critical feedback and directives.

David Saah and Jason Moghaddas (SIG) are acknowledged for managing SIG's effort in this project.

The Project Oversight Workgroup (POW) is acknowledged for providing feedback and guidance, in particular Ash Lashgari (ARB), Tom Pyle (Caltrans), Deepak Maskey (Caltrans), Rupa Basu (OEHHA), Walker Wieland (OEHHA), as well as Courtney Smith (ARB), Peter Dirrim (Caltrans), LaNae Van Valen (Caltrans), Michael McCormick (OPR), Paul English (CDPH), Bart Ostro (OEHHA), Max Gomberg (Waterboards), William Farnbach (Caltrans), Nesar Formoli (Caltrans), Augie Rosales (Caltrans), Martha Brook (CEC), John Melvin (CalFire), Amy Dickie (CEA), Erik de Kok (Ascent), David Fink (ClimateResolve), and Brendan Reed (City of ChulaVista).

William Dean (CalEPA), Gina Solomon (CalEPA), Ash Lashgari (ARB), Susan Wilhelm (CEC), Dev Millstein (LBNL), Walker Wieland (OEHHA), Rupa Basu (OEHHA), and Xiangmei Wu (OEHHA) are acknowledged for reviewing the project final report and providing technical comments and constructive suggestions.

This report was submitted in fulfillment of CalEPA Contract No. 13-001 by Altostratus Inc. under the sponsorship of the California Environmental Protection Agency. Work was completed as of April 24th, 2015.

TABLE OF CONTENTS

Abstract - - - - - - - - - - 1

Executive Summary - - - - - - - - - 2

1. Introduction - - - - - - - - - 5

2. Materials and methods - - - - - - - - 6
   - 2.1. Definition of the UHI Index (UHII) - - - - - 7
   - 2.2. Models - - - - - - - - - 10
   - 2.3. Modeling periods and domains - - - - - - 12
   - 2.4. Model input data - - - - - - - 14
   - 2.5. Model modifications and customizations - - - - 24

3. Results - - - - - - - - - - 37
   - 3.1. Initial model tests - - - - - - - 37
   - 3.2. UHI/UHII reference points - - - - - - 40
   - 3.3. Initial model output examples - - - - - - 41
   - 3.4. Model performance evaluation - - - - - - 47
   - 3.5. UHII calculations - - - - - - - 57
     - 3.5.1. UHII tiles and UHI reference points - - - - 57
     - 3.5.2. UHII Calculation results - - - - - 59
   - 3.6. Datasets provided - - - - - - - 66

4. Discussion - - - - - - - - - - 68
   - 4.1. Spatial patterns of the UHII - - - - - - 68
   - 4.2. Archipelagos, surface, and air temperatures - - - - 69
   - 4.3. UHII and the background temperature - - - - - 74

5. Summary and conclusions - - - - - - - 85

6. Recommendations and future research - - - - - - 87

7. References - - - - - - - - - - 88

8. Glossary of abbreviations and acronyms - - - - - - 93

9. Appendices - - - - - - - - - 94

LIST OF FIGURES

ES-1	Urban islands, archipelagos, and heat islands	3
ES-2	Spatial distribution of UHII in the Fresno region	4
1	Framework of the UHII definition	8
2	Conceptual incremental levels of the UHII	10
3	Main model components and data flow	12
4	Study modeling domains and 3-km positions relative to CalEnviroScreen	13
5	1-km domains and positions relative to CalEnviroScreen	14
6	Example LULC map for Sacramento	20
7	Urban land-use classes in USGS Level-II and NLCD for the SFBA	21
8	Urban land-use classes in USGS Level-II and NLCD for California	22
9	Study-modified approach for surface characterization	25
10	Up-scaling of 30-m surface properties	26
11	Meshing of urban physical properties with non-urban land use	27
12	Skin-surface temperature from study-modified approach	29
13	1-km surface albedo and shade factor based on modified approach	32
14	1-km roughness length example	35
15	Simulation marching, re-initializations, and spin-up intervals	37
16	Nighttime and daytime skin-surface temperature from modified approach	38
17	San Francisco-Sacramento-Stockton-Modesto night lights	39
18	Example 2-m air temperature output from modified approach	39
19	UHI/UHII reference points for the Fresno and Sacramento regions	42
20	UHII example for Sacramento region	44
21	UHII example for Fresno region	45
22	UHI/UCI examples at several points in Fresno and Sacramento	46
23	Model performance evaluation domain	47
24	Example 850 mb maps for July 7 and August 23, 2013	55
25	Example of hourly model output and MPE	56
26	UHII-calculation tiles	58
27	UHI reference points	58
28	UHII in west Los Angeles Basin	63
29	Example archipelagos in U.S. and international locations	65
30	Daytime skin-surface temperature in east Los Angeles domain	69
31	Air temperatures in Los Angeles Basin (PRISM data)	70
32	Daytime skin-surface temperature in Santa Clara Valley / San Jose	72
33	Single/multi core UHIs/UHIIs and archipelagos	72
34	DH/day average at UHI reference points and frequency distributions	80

A1 – A40	Appendix A UHII maps	A1 - A43
B1 – B40	Appendix B UHII maps	B1 - B40
C1 – C41	Appendix C UHII and CalEnviroScreen maps	C1 - C42
D1 – D40	Appendix D UHII maps	D1 - D41

.

LIST OF TABLES

Table 1	Phases and tasks of project - - - - - -	6
Table 2	Horizontal domain dimensions - - - - -	13
Table 3	NCEP/NCAR Reanalysis (NNRP) meteorological variables -	15
Table 4	USGS Level-II (GIRAS) classification system - - -	18
Table 5	NLCD classification system - - - - - -	19
Table 6	Summary of crosswalk between urban NLCD and USGS Level-II classes	23
Table 7	Assignment of 200-m albedo - - - - -	30
Table 8	Comparison of the fabric (%) of 4 cities - - - -	32
Table 9	Crosswalk from USGS to NLCD urban classes - - -	34
Table 10	Impervious and roof area for NLCD urban classes - - -	34
Table 11	Modeling periods - - - - - - -	37
Table 12	UHI reference points attributes - - - - -	42
Table 13	Number of observational monitors in model domains - -	48
Table 14	Community-suggested model performance benchmarks - -	51
Table 15	Model performance evaluation metrics - - - -	52
Table 16	Urban heat island index (UHII) - - - - -	60
Table 17	Example microclimate variations in west Los Angeles Basin -	63
Table 18	UHII ranges - - - - - - - -	66
Table 19	DH/day for UHI reference in various regions and time periods -	75
Table 20	Frequency distribution of census tracts in UHII bins - -	83

ABSTRACT

In order to further evaluate the factors that can influence thermal environmental stresses, a characterization of how urban areas affect local microclimates, air temperature in particular, is necessary. To assist the CalEPA in evaluating the thermal impacts of urban areas in California, this study characterizes the urban heat island (UHI) and quantifies an urban heat island index (UHII) for each census tract in a number of urban areas. For this purpose, detailed multi-scale meteorological modeling was carried out and a UHII definition was developed.

The UHII results presented in this report include total degree-hours (DH) over the modeled seasons (June, July, August 2013 and 2006), DH per day averages, as well as other metrics, such as temperature differences. The UHII spatial patterns were analyzed for small, large, inland, urban archipelago, and coastal areas. Since, within each region, there are a large number of census tracts, there is correspondingly a large range of UHI and UHII values. At the lower end of the scale (small urban areas), the UHII ranges from 2 to 20 DH/day (°C.hr/day) whereas at the higher end (larger areas), it reaches up to 125 DH/day or more. The largest average temperature difference (UHI) within each region, ranges from 0.5–1.0°C in smaller urban areas to up to 5°C or more at the higher end, such as in urban archipelagos.

The analysis indicates that the UHI can be exacerbated during warmer weather and that, in turn, can exacerbate the health impacts of heat events in urban areas. Along with other available environmental data, such as from CalEnviroScreen or other region-specific assessments, the UHII can provide information to help identify and prioritize areas for mitigation. This study does not propose mitigation measures or suggest certain control strategies, nor does it assess their potential effectiveness or positive and negative impacts; it only is a characterization of the UHI and UHII in various urban areas in California under existing conditions.

EXECUTIVE SUMMARY

Background

Urban climates can impact local meteorological fields, emissions of heat and pollutants, and photochemical production of ozone. One relatively well-documented characteristic of urban climates is the urban heat island (UHI). UHIs can locally exacerbate the effects of regional and global climates on heat and air quality especially during summer. This exacerbation can have particularly detrimental implications during heat events and heat waves with significant ramifications in terms of public health, from both heat and air-quality pathways. As a result of UHIs, cooling energy demand increases, emissions of pollutants increase, the photochemical production of ozone accelerates, and air quality deteriorates further. Because of these potential negative impacts, efforts at the city and regional levels are being undertaken to better characterize UHIs and propose effective mitigation measures. Pursuant to AB 296, the California Environmental Protection Agency (CalEPA) has initiated an effort to quantify the UHI and develop a UHI Index (UHII) for California.

Methods

In this CalEPA-supported study, the UHI was characterized via detailed meteorological modeling of California. A UHII was then defined and calculated for each census tract in a number of selected urban areas. The ultimate goal of developing the UHII is for use in assessing the potential heat health implications of urban land use and UHI, identifying geographical areas where UHIs can exacerbate environmental health issues, and possibly as an additional layer of information for use with the CalEnviroScreen tool. The UHII is an indicator to the exacerbation of heat by urban areas, as measured by the urban-nonurban temperature difference.

During the initial stages of the study, a definition of the UHII was developed. Several variations of the definition, with various degrees of complexity, were considered and evaluated. Based on directives from CalEPA and the Project Oversight Workgroup (POW), a simple definition of the UHII was adopted:

$$UHII = \sum_{h=1}^{H(JJA)} \left[T_{u,k,h} - min\left(T_{u,k,h}, T_{nu,k,h}\right)\right]$$

where $T_{u,h}$ is the urban temperature at time-step h, $T_{nu,h}$ is the nonurban temperature at time-step h, H is the number of time-steps, and k is the location index (census tract). The calculation yields a cumulative UHII (in degree-hours) over designated periods, in this case June, July, and August 2013 and 2006.

Following the establishment of the UHII definition, the modeling system was prepared for the application. Project tasks included 1) preparing and generating the needed surface and atmospheric input data, 2) characterizing the land use and land cover at fine resolutions throughout the state of California, 3) updating, modifying, and customizing the model parameterizations and urban representations, 4) testing the various components of the model, 5) performing detailed statistical evaluation of model performance against modeling-community-recommended performance benchmarks, 6) applying the models and calculating the UHII for

every census tract in the selected urban areas, and 7) analyzing the results and characterizing and mapping the UHII.

Results

The UHII was calculated for each census tract in terms of total degree-hours (DH) over the modeled seasons, DH per day averages, as well as other metrics such as temperature differences and time series. The UHII spatial patterns were grouped into small, large, inland, urban archipelago[1], and coastal areas, as well as single or multiple-core UHIs (Figure ES-1, A,B). The UHII was characterized under typical summer conditions during the selected periods as well as during excessive heat events such as during the 2006 heat wave. Because of the large number of census tracts analyzed and because of the varying microclimates in California, there is correspondingly a large range of UHI and UHII values in different regions. At the lower end of the scale (in smaller urban areas), the UHII ranges from 2 to 20 DH/day (°C.hr/day) whereas at the higher end (larger urban areas), it reaches up to 125 DH/day or more. The largest average temperature difference (largest average UHI) in each region ranges from 0.5 – 1.0°C at the lower end and up to 5°C or more at the higher end.

Spatial patterns of the UHI were also analyzed. The modeling shows that urban areas with relatively well defined boundaries (i.e., urban islands) typically exhibit single- or multi-core UHIs, e.g., Figure ES-2 (left). On the other hand, large urban archipelagos and coastal regions, such as the Los Angeles Basin and the Santa Clara Valley (Figure ES-1, B) consist of sustained and contiguous urban land use with no well-defined boundaries, except for breaks by topography. In this case, the UHI often peaks in areas near the downwind edges of the archipelago. Thus whereas in urban islands the local UHI is mostly a result of local processes that are strongly dependent on local land-use properties (line 4 minus line 1 in Figure ES-1, A), the local UHI in an archipelago / coastal areas (line 4 minus line 1 in Figure ES-1, B) additionally includes the superimposed effects of on-shore warming (line 2 minus line 1) and upwind urban warming (line 3 minus line 2).

Figure ES-1. Conceptual depiction of localized UHIs, urban archipelago-induced and on-shore warming in urban islands (A) and urban archipelagos (B).

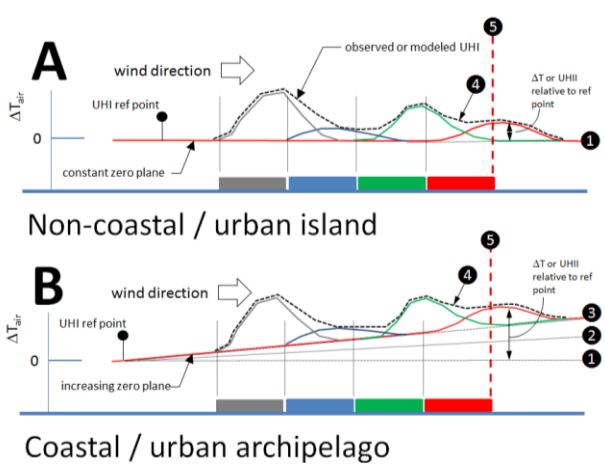

[1] The term "archipelago" is used in this study to refer to large, continuous urban expanses with sustained density of development and urban land use.

The modeling also captures the synergies between the UHI and regional climate. The analysis shows that compared to cooler periods, warmer weather, e.g., during a heat wave, enhances the UHI and shifts the UHII towards larger values. The example in Figure ES-2 for an arbitrary location (Fresno) shows a map of total UHII (DH per 182 days), as well as a frequency distribution of census tracts across a range of UHII bins. It can be seen that the heat wave event of July 16-31, 2006 shifts a number of census tracts towards higher UHII values (bins) relative to a cooler period of time in June 1 – 16, 2006. Several California urban area examined in this study also exhibit this pattern of larger UHII during the heat wave. The implications are that as heat waves become possibly more frequent because of changes in climate, they can intensify the UHIs in many regions, further exacerbating heat stress in urban areas. Thus mitigation measures, such as cool cities and sustainability, will become even more important in the future.

Coastal urban areas with deep basins and catchment zones, such as Los Angeles basin and the Santa Clara Valley, exhibit a slightly different pattern of UHII shift during warmer weather because of stronger local venting during such conditions. In these cases the temperature, while larger in absolute values than during the cooler periods, becomes more uniform across the basin and thus the UHII, by definition becomes more uniform.

Figure ES-2. Left: Spatial distribution of total UHII in the Fresno region. **Right:** Frequency distribution (percent of census tracts in the area) of UHII bins (blue: coolest period, red: heat wave).

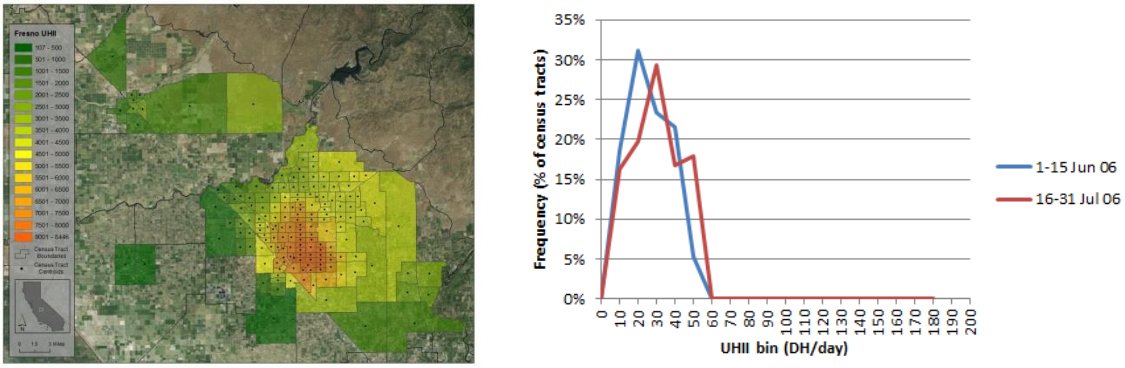

Conclusions

In this study, the UHII was developed and calculated solely for characterizing and quantifying the effects of urban areas in exacerbating heat under existing conditions. As such, the computed UHII can be used to identify vulnerable geographical areas and/or possibly as an additional layer of information for potential use in conjunction with the CalEnviroScreen tool. As discussed in this report, there are several additional levels of UHII beyond what was completed in this study, which can be developed in the future. These include UHII indicators tailored for mitigation purposes and implementation of cool cities or other control measures. It is recommended that these additional levels of the UHII be developed and quantified as part of follow-on research to characterize both positive and negative effects of potential mitigation measures and prioritize their deployments. It is also recommended that the synergies between UHI and heat waves be further studied and quantified in order to assess the benefits of control measures, such as cool cities, in future years.

1. INTRODUCTION

It has been known since decades ago (e.g., Bornstein 1968,1995, Bornstein and Johnson 1977, Oke 1978, Lombardo 1985, Bornstein and Lin 2000) that urban areas create their own climates and modify the local meteorological fields, including temperature, wind, mixing, moisture, convective cloudiness, and precipitation. One relatively well-documented characteristic of urban climates is the urban heat island[2] (UHI) (Oke 1978). UHIs also affect emissions of heat and pollutants, such as oxides of nitrogen (NOx), volatile organic compounds (VOC), and particulate matter (PM), and the photochemical production of ozone (Taha 2007,2008a,b,c, 2015).

UHIs can *locally* exacerbate the effects of regional and global climates on urban heat and air quality (Goggins et al. 2012, Adachi et al. 2012, Tan et al. 2010, Taha 2001). This exacerbation can have further detrimental implications during heat events and heat waves with significant ramifications in terms of public health, from both heat and air-quality pathways (Vanos et al. 2014, Kalkstein et al. 2013). As a result of UHIs, cooling energy demand increases, emissions of anthropogenic and biogenic pollutants (e.g., ozone precursors) increase, the photochemical production of ozone accelerates, and air quality (e.g., O_3, $PM_{10/2.5}$, NO_x) deteriorates (Taha 2013a,2015).

Because of the potential negative impacts, various efforts at city and regional levels have begun addressing and characterizing UHIs. The California Environmental Protection Agency (CalEPA) has initiated efforts to better understand and quantify the UHI and develop a UHI Index (UHII). In this effort, the UHI was characterized via meteorological modeling of California and the index (UHII) was computed based on model results. The purpose of developing the UHII is for use in 1) assessing the heat health implications of urban land use, 2) identifying geographical areas where UHIs can exacerbate environmental health issues (heat and air quality), and 3) possibly as a potential modifier to information in the CalEnviroScreen[3] tool (OEHHA 2013). The specific goal of this study is to develop the UHII and quantify the impacts of urban areas on air temperature, among other meteorological variables, relative to background, non-urban conditions. That is, the UHII is an indicator to the exacerbation of heat by urban areas, as indicated by the urban-nonurban temperature differential.

The scope of the study, per CalEPA directives, is solely to characterize the problem, that is, characterize and quantify the UHI as is, and compute the UHII accordingly. The UHII developed in this study does not incorporate indicators to deployment potentials or the positive and negative effects of mitigation measures. The latter are left for possible follow-on efforts in the future.

The study was organized into eight inter-dependent tasks. During the initial stages of the project, a definition of the UHII was developed. Several variations of the definition with varying levels of complexity were evaluated, as discussed in Section 2. Following the establishment of the UHII definition, the modeling system was updated and prepared for this study. The steps included 1) preparing and generating the needed surface and atmospheric input data, 2) characterizing the land use and land cover at fine resolutions throughout the state of California, 3) updating, modifying, and customizing the model parameterizations for urban representation,

[2] In its simplest form, a UHI is the temperature difference between an urban point, or number of points, and some non-urban reference point.

[3] CalEnviroScreen is a communities environmental health screening tool designed to help identify and assign a score to California communities that are burdened by multiple sources of pollution.

4) testing the various components of the model, 5) performing quantitative evaluation of model performance against modeling-community-recommended performance benchmarks, 6) applying the models and calculating the UHII for every census tract in the selected urban areas, and 7) analyzing the results and characterizing and mapping the UHII.

The modeling and development of UHII in this study is for current conditions (years 2006, 2013). The study makes no assumptions about climate change or its potential regional impacts. Furthermore, the UHII thus derived does not indicate whether mitigation of UHI will locally result in net positive or negative effects; it is not a characterization of the effects of mitigation measures. The latter must be tailored on a region-specific basis to maximize the benefits (Taha 2008a-c,2015) and will require extensive modeling and analysis in the future.

Finally, the modeling domains are configured to capture a variety of urban areas in California, per project requirements of studying a diverse sample of areas with a variety of locations, climates, and geographical properties (size, density, and spatial characteristics). The selected modeling and analysis periods (June, July, and August of 2013 and 2006) also include the California heat wave of July 15 – August 1st, 2006 (Gershunov et al. 2009).

2. MATERIALS AND METHODS

This effort was undertaken to develop a UHI Index (UHII) for California based on mesoscale and meso-urban meteorological modeling. The goal was to develop an index that quantifies the impacts of urban areas on air temperature, among other meteorological variables, relative to background, non-urban conditions. The various phases of modeling and data development in this effort are outlined in Table 1 along with task responsibilities.

Table 1: Phases and tasks of the project

Task	Responsible party (Prime/Subcontractor)
Task 1: Define the Urban Heat Island Index	Prime
Task 2: Identify, Generate, and Obtain Useful Datasets	Prime and Sub-Contractor
Task 3: Update and Customize Model	Prime
Task 4: Provide Sample Results and Refine Model	Prime
Task 5: Validate Model	Prime
Task 6: Calculate Urban Heat Island Index in California Cities	Prime
Task 7: Provide Results of Analysis	Prime and Sub-Contractor
Task 8: Final Report and Analysis	Prime and Sub-Contractor

Prime: Altostratus Inc.
Sub-Contractor: Spatial Informatics Group

During the course of the project, a technical note was produced for each of Tasks 1 - 8 and submitted to CalEPA for review and approval. These standalone technical notes are available upon request. In this final project report, material from these technical notes, as well as new material on analysis of results, has been merged and recast in each of this report's sections.

2.1. DEFINITION OF THE UHI INDEX (UHII)

The initial task in this contract was the development, approval, and application of a UHI Index (UHII). While several forms of the UHII were proposed and evaluated during the early stages of this study, Equations 1 and 2 (Figure 1) represent the general framework of the UHII. Some of the variations in the definition that were considered earlier in the project were: 1) the inclusion of different temperature thresholds (*thsh*), 2) the computation of UHII when urban temperature is higher than non-urban ($T_u > T_{nu}$) or at all times, and 3) weighting by indicators such as population density (CF_p) or technical potential (CF_{tp}).

A criterion that must be met in developing the UHII definition was that it captured both the *severity* (magnitude) and *extent* (duration) of the urban-nonurban temperature differential. The integral approach depicted in Figure 1 was proposed to satisfy this requirement. The various variations and iterations of the UHII were elaborated further by CalEPA and evaluated by the POW.

The initial framework proposed for the UHII, as shown in Figure 1, involved integrating (over all periods) the urban-nonurban temperature difference ($\Delta T_{u\text{-}nu}$), in Equation 1. The term δ_{thsh} in Equation 2 represents the heat advected into a certain location (e.g., census tract) from upwind sources. The ΔT term represents the intensity (or magnitude) and captures both heat- and cool-island effects. However, depending on a user-selected threshold (*thsh*), some temperature differentials are filtered out. The intended use of a threshold temperature (*thsh*) was only as a trigger for the calculations of temperature difference T_u - T_{nu} (in Equation 1) whenever $T_{nu} > thsh$. The threshold value did not, in itself, enter into the UHII calculations. In addition, the threshold was based on non-urban temperature (T_{nu}) as a reference. Thus for each T_{nu} threshold selected, the differential T_u-T_{nu} was calculated regardless of whether T_u was above or below the threshold (as long as T_{nu} was above).

After evaluating several possible formulations, a simpler version of the UHII was recommended by the CalEPA and the POW and adopted as in Equation 3, where $T_{u,h}$ is the urban temperature at time-step h, $T_{nu,h}$ is the nonurban temperature at time-step h, H is the number of time-steps, and k is the location index, i.e., census tract. Note that there are no temperature thresholds in this definition. The calculation simply integrates (sums up) over the designated period, in this case JJA, over all hours including day and nighttime. The inclusion of nighttime hours is important as research shows that heat stress also depends on nighttime temperatures, especially during hot weather episodes. The "min" operator in Equation 3 acts as a filter such that the UHII is computed only when urban temperature is higher than the non-urban UHI-reference temperature.

As discussed in Section 1, it is important to note that the UHII in this study is developed for current climate and land-use conditions (recent years) and is unrelated to potential future-year scenarios, i.e., regional tendencies, urbanization trends, or potential climate change. In addition, the UHII computed as in Equation 3 is a quantification of the <u>existing</u> impacts of urban areas on the ambient environment and does not include predictions as to the potential benefits (positive) or inadvertent (negative) effects of any control measure, including UHI mitigation. As alluded to earlier, the UHII could be devised in several levels or stages that progressively modify it from an index that characterizes the problem, e.g., at top of arrow (in Figure 2), to an index that characterizes the mitigation, at the bottom of the arrow (the arrow direction in Figure 2 shows incremental increase towards characterizing the potential for and benefits from mitigation).

Figure 1: Framework of the UHII definition.

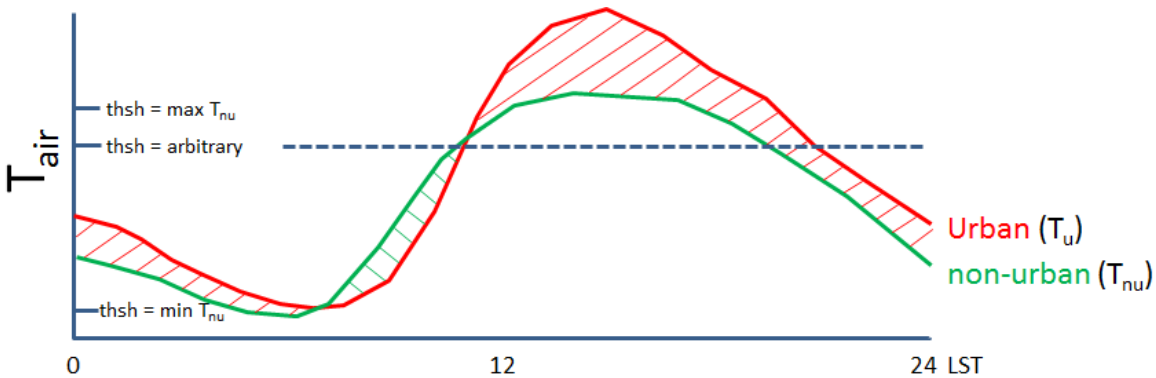

$$UHII'_{thsh}(DH) = \int_{t=0}^{t=end} \Delta T_{u-nu}\, dt\,, \qquad for\ T_{nu} \geq thsh \qquad (1)$$

$$UHII_{thsh}(DH) = \underbrace{\{UHII'_{thsh} - \delta_{thsh}\}}_{\text{Meteorological UHII (tasked to produce per RFP)}} \times CF_p \times CF_{tp} \qquad (2)$$

p = population
tp = technical potential

$$UHII = \sum_{h=1}^{H(JJA)} \left[T_{u,k,h} - min\left(T_{u,k,h}, T_{nu,k,h}\right)\right] \qquad (3)$$

Per CalEPA and POW directives, the focus of developing the UHII in this project was solely for Level 1 (Figure 2). Thus, levels 2-4 could potentially be addressed in possible future efforts. For the sake of this background discussion, however, the four UHII levels are described briefly below (refer to Figure 2).

Level 1: involves characterizing the UHI and computing the UHII as is, that is, regardless of heat transport, on-shore warming, or other factors such as urban archipelago effects. A Level-1 UHII characterizes the existing thermal environment, i.e., what a thermometer would indicate in the real world at various census tract locations (regardless of the causative factors that led to the creation of the local UHI). Thus a Level-1 UHII can be useful as an additional modifier in CalEnviroScreen to further assess burdens and indicators to potential health impacts of urban areas. However, 1) the Level-1 UHII does not assign responsibility for the UHI, i.e., it does not distinguish between effects of local sources of heat and effects of transport from upwind areas; 2) does not provide an estimate as to the potential for mitigation; and 3) does not provide information on response or associated positive/negative effects from potential mitigation measures.

Level-1 UHII was the only level to be modeled and mapped in this project.

Level 2: includes Level 1 with the addition of weighting by population density (CF_p) and by technical potential[4] (CF_{tp}) as shown in Equation 2 (in Figure 1). A Level-2 UHII can provide some additional information in terms of potential effects on population (via population density) and potential for local action (via technical potential). However, 1) the Level-2 UHII is still not corrected for heat transport (δ_{thsh}) or on-shore warming (if the area is coastal) but can provide additional site-specific information, and 2), it still does not assign responsibility for the UHI. And while a level-2 UHII can provide information as to potential local implementation of mitigation measures, i.e., how much surface area (pavements, roofs) is available for modification or can be modified locally (via CF_{tp}), it still does not provide information about the resulting atmospheric impacts and nothing about the potential for mitigation or associated positive / negative effects.

Level 3: includes Levels 1 + 2, with additional, detailed atmospheric modeling to subtract the advected heat (from the UHII) in each area based on quantifying a length scale for fetch effects. The sources of advected heat are 1) on-shore warming in coastal areas and 2) urban archipelago effect. Thus a Level-3 UHII includes computing the term δ_{thsh} in Equation 2 (Figure 1). At this level, the UHII can be used to "assign" responsibility more accurately, that is, allow each census tract or city to estimate the share of their UHI they are actually responsible for and the potential for mitigating the UHII. This will set a more realistic target for mitigation than the Level-2 UHII because it is now corrected for heat transport, but will require a great deal of additional modeling beyond Levels 1 and 2.

Level-3 UHII still does not provide an estimate as to how much of the assigned UHII could actually be mitigated locally at the census tract level nor an estimate of the positive or negative impacts of mitigation measures (or how to tailor such measures in the most optimal way for site-specific conditions in each group of census tracts or a city). One benefit of Level 3 modeling is the ability to determine how much of a temperature differential across an urban archipelago or coastal area is due solely to urban warming / UHI effects and how much of it is due to onshore warming of air from the coast or the bay.

Level 4: includes Levels 1 + 2 + 3 with additional and comprehensive modeling of mitigation measures to evaluate their atmospheric impacts, both positive and negative. Mitigation measures include, for example, cool pavements, cool roofs, control of anthropogenic heating, deployment of solar photovoltaic and thermal technologies, vegetation and urban forests, energy efficiency, green roofs, and runoff control. They can be modeled and evaluated separately and in various combinations (e.g., Taha 2013a,b, Rosenfeld et al. 1996, Rosenzweig et al. 2006, Taha et al. 2011).

A Level-4 UHII can account for both positive and negative impacts of mitigation measures and their interactions / feedbacks. This is important for development of area-specific deployment plans, as several studies have shown that mitigation measures could have both positive (beneficial) and negative (inadvertent) effects both at the local / regional scales (Taha

[4] Technical potential is an indicator to availability of surface area for deployment of measures such as cool roofs and pavements, urban forests, solar photovoltaics, and so on. It is also an indicator to the actual extent such measures can be implemented at, i.e., the amount of albedo increase or change in surface properties.

2007,2008a-c,2013a,b) or at the larger, global scales (Jacobson and TenHoeve 2011, Millstein and Menon 2011). Some of the positive effects include urban cooling, energy demand reduction, emissions reductions, improvements in air quality, thermal comfort enhancement, and reduced radiative forcing. The negative effects, on the other hand, can include warming, reduced mixing, weaker sea-breeze and onshore flow, increased ozone formation, reduced convective cloudiness, and impacts on surface hydrology and runoff. The information that a Level-4 UHII can provide will, in turn, be important in tailoring the mitigation measures and scenarios for site-specific attainment of the UHII, maximizing the positive effects and minimizing the negative ones at census-tract scale. Level-4 UHII will require extensive modeling as it will also account for interactions with upwind and adjacent cities or census tracts with various mitigation scenarios.

Figure 2: Conceptual incremental levels of the UHII.
(Note: Level 1 is the UHII developed in this study).

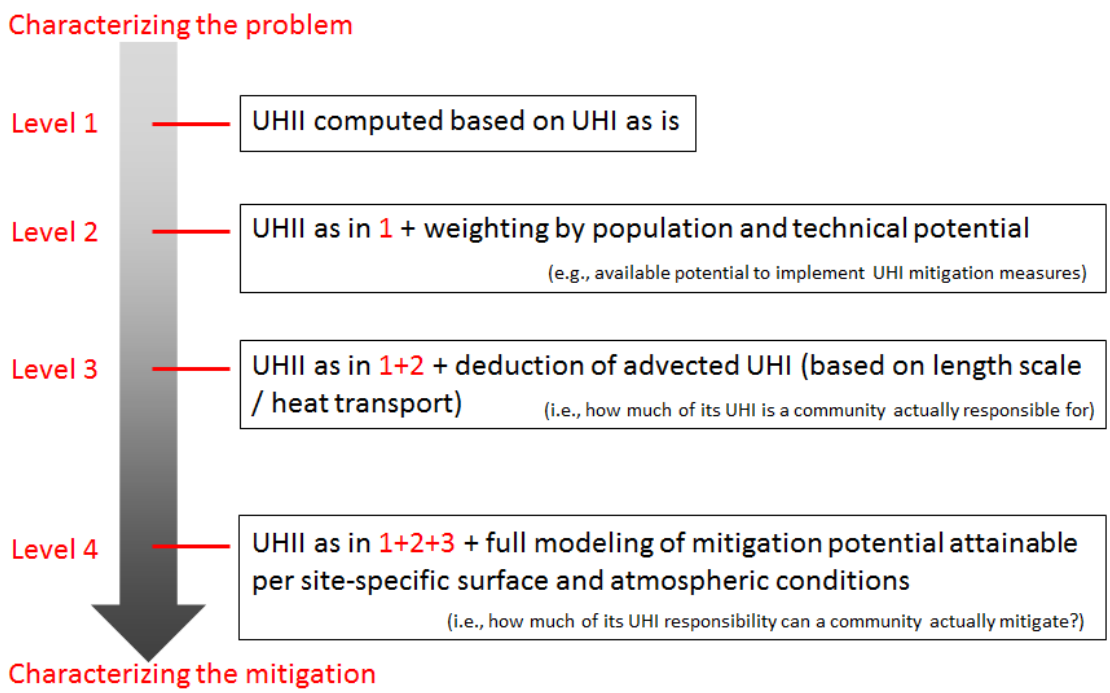

2.2. MODELS

This study was carried out using the WRF-ARW (Advanced Research WRF) suite of models (Skamarock et al. 2008). Some components of the model were modified and customized in this study, as discussed later in Section 2.5, to better suit this particular application in UHI and UHII characterizations.

The WRF model consists of several main components and a large number of modules within each. These include:

- WRF Pre-processing System (WPS) which prepares the meteorological and surface data, defines the model domains and grid nesting structures, prepares the terrain, land-use, and soil-properties input, and interpolates meteorological and surface data to the selected model grids and map projection systems. The WPS also processes several data types including, among others, the USGS LULC system (Anderson et al. 2001), NLCD (MRLC 2014), the MODIS 20-category land-cover data (Zhou et al. 2003), and GRIB2 meteorological data from NCEP, NCAR, and other sources, as well as other static data.
- Dynamic core (WRF ARW) and main model which includes the Advanced Research WRF (ARW) solver. Some of the model's main features include full compressibility non-hydrostatic formulation, Coriolis and curvature terms, nesting with two-way feedbacks including vertical nesting, mass-based terrain-following coordinate system, various map projection systems, Arakawa C stagger of the momentum and mass variables, small time-splitting step for acoustic and gravity wave modes, various top and lateral boundary condition options, four-dimensional data assimilation including both observational and grid nudging, and various physics, land-surface, boundary-layer, radiative transfer, and cumulus parameterization schemes (Skamarock et al. 2008).
- Variational data assimilation system (WRF-DA / 3D- and 4D-VAR). This system allows improvement to reanalysis input, prepared by WPS, by ingesting and assimilating observational data (thus improving the quality of the model's input).
- Post-processing systems and data visualization tools.

In this study, we considered using and evaluated the performance of urbanized WRF modules such as the UCM (Kusaka et al. 2001, Chen et al. 2010) and BEP-BEM modules (Salamanca et al. 2011) along with the boundary-layer scheme of Bougeault and Lacarrere (1989). In terms of urban parameterizations, two of the more recent versions of WRF (3.4.1 and 3.5) contain the urban formulations suitable for fine-resolution modeling. Version 3.5, which was released in August 2013 adds the capability of using built-in NUDAPT urban data (Ching et al. 2009). However, the urban parameterizations in version 3.5 were not sufficiently tested in our UHI applications. Furthermore, around the time this study was planned, NUDAPT data coverage was uneven across various regions in California and the model modifications performed in this study can override the NUDAPT input as discussed in Section 2.5. Thus this study uses version 3.4.1 of WRF along with modifications (Taha 2008a-c) that can provide more even coverage than NUDAPT data at this time for areas throughout California. For this reason, it was also decided to not use the BEP/BEM modules in this application. The UCM, BEP and BEM modules may be more appropriate for use with Level 3 and 4 UHII modeling (see Section 2.1), especially at sub-kilometer resolutions, and where site-specific (cell-specific) surface characteristics are available. Lacking such specificity, the use of urbanized models is sometimes not any better than application of non-urban modules.

Furthermore (as discussed Section 2.5), certain aspects of the modeling system were modified and customized in this study, particularly surface data ingestion in certain surface- and boundary-layer parameterizations and the land-surface model (NOAH), resulting in a simple model update. Taha (2008a-c,2011,2013a,b) used similar modifications in previous studies including those performed for the California Energy Commission (Taha 2007,2013a,b), the Sacramento Metropolitan AQMD (Taha et al. 2011), and San Jose State University (Bornstein et al. 2006). Figure 3 shows the main model components and data flow among them.

Figure 3: Main model components and data flow.

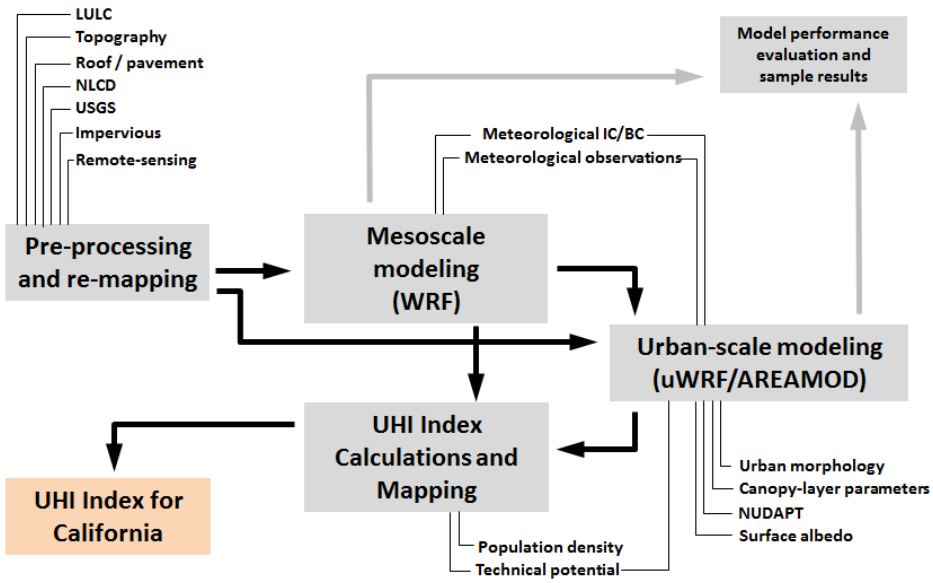

2.3. MODELING PERIODS AND DOMAINS

Modeling periods:

Per CalEPA and POW directives, the modeling periods were selected to encompass the months of June, July, and August (JJA) of 2013, as the most recent representative year. To also evaluate the UHI and UHII under conditions of excessive heat, the JJA period of 2006 was also modeled to capture the impacts of the California heat wave of July 15 through August 1st, 2006 (Trent et al. 2007, Gershunov et al. 2009). For both years, the JJA periods were simulated as series of shorter intervals to reduce model drift by re-initializing over the course of the simulation. This will be explained further in Section 2.5.8.

Modeling domains:

The lower-left part of Figure 4 depicts the structure and configuration of the nested grids (27, 9, 3, and 1 km) in the WRF-ARW meteorological model. Domain D01 has a 27-km resolution; D02 has 9-km resolution, whereas domains D03, D04, and D05 have 3-km resolution. Domains D06 through D10 are at 1-km resolution. The 3- and 1-km model grids are configured in relation to CalEnviroScreen 2.0 top 20%, 10%, and 5% areas so as to focus the finer-scale simulations on these regions (Note: regions with high CalEnviroScreen scores are those with increased health risks and vulnerabilities, thus top 5% areas, for example, have increased vulnerabilities relative to, say top 20% areas).

The right part of Figure 4 depicts the positions of domains D03 through D05 relative to CalEnviroScreen top 20% and 10% areas (OEHHA 2013). These domains capture ~95% of urban areas south of Lake Tahoe's latitude. As shown in Figure 5 (for 1-km domains), domain D06 encompasses the Stockton-Modesto-Patterson area, D07 is Fresno, D08 is Bakersfield, D09

is west Los Angeles basin, and D10 is the east Los Angeles basin. The 1-km domains were positioned so as to include 1) clusters of top 5% census tracts (discarding standalone tracts) and 2) census tracts that are in urbanized areas (not rural or sub-urban). Table 2 lists the resolutions and dimensions of the modeled grids (in units of grid points). The definition of urban and non-urban areas is based on land-use/land-cover classification (see item E in Section 2.4). Furthermore, in the analysis, a population threshold of 50 km^{-2} was also used.

Figure 4. Bottom-left: Study modeling domains. **Right:** Positions of domains D03, D04, and D05 (black-line rectangles) relative to top 10% and 20% areas in CalEnviroScreen 2.0 (red-colored census tracts).

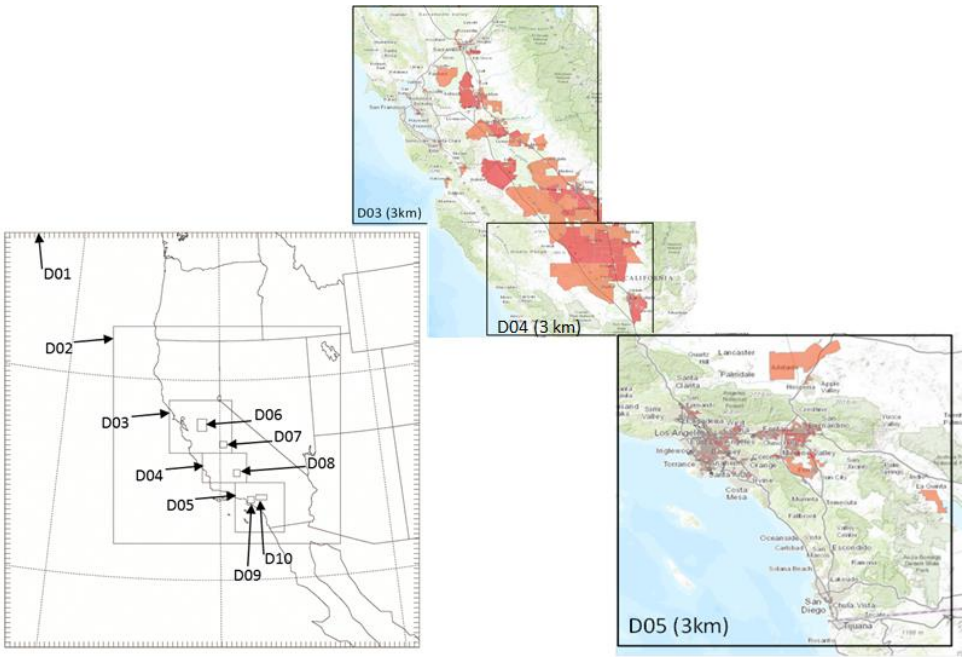

Table 2: Horizontal domain dimensions (grid points) and resolutions

	D01 (27km)	D02 (9km)	D03 (3km)	D04 (3km)	D05 (3km)	D06 (1km)	D07 (1km)	D08 (1km)	D09 (1km)	D10 (1km)
W-E	85	139	115	82	91	52	40	37	37	61
S-N	85	133	97	55	99	67	34	40	37	28

The vertical domain is resolved with 35 levels as an optimum between simulation time and detail. However, the vertical resolution is increased near the surface, e.g., within the urban boundary layer, to better capture the processes of relevance to UHI / UHII characterizations.

Figure 5: 1-km domains and positions relative to CalEnviroScreen top 5% areas

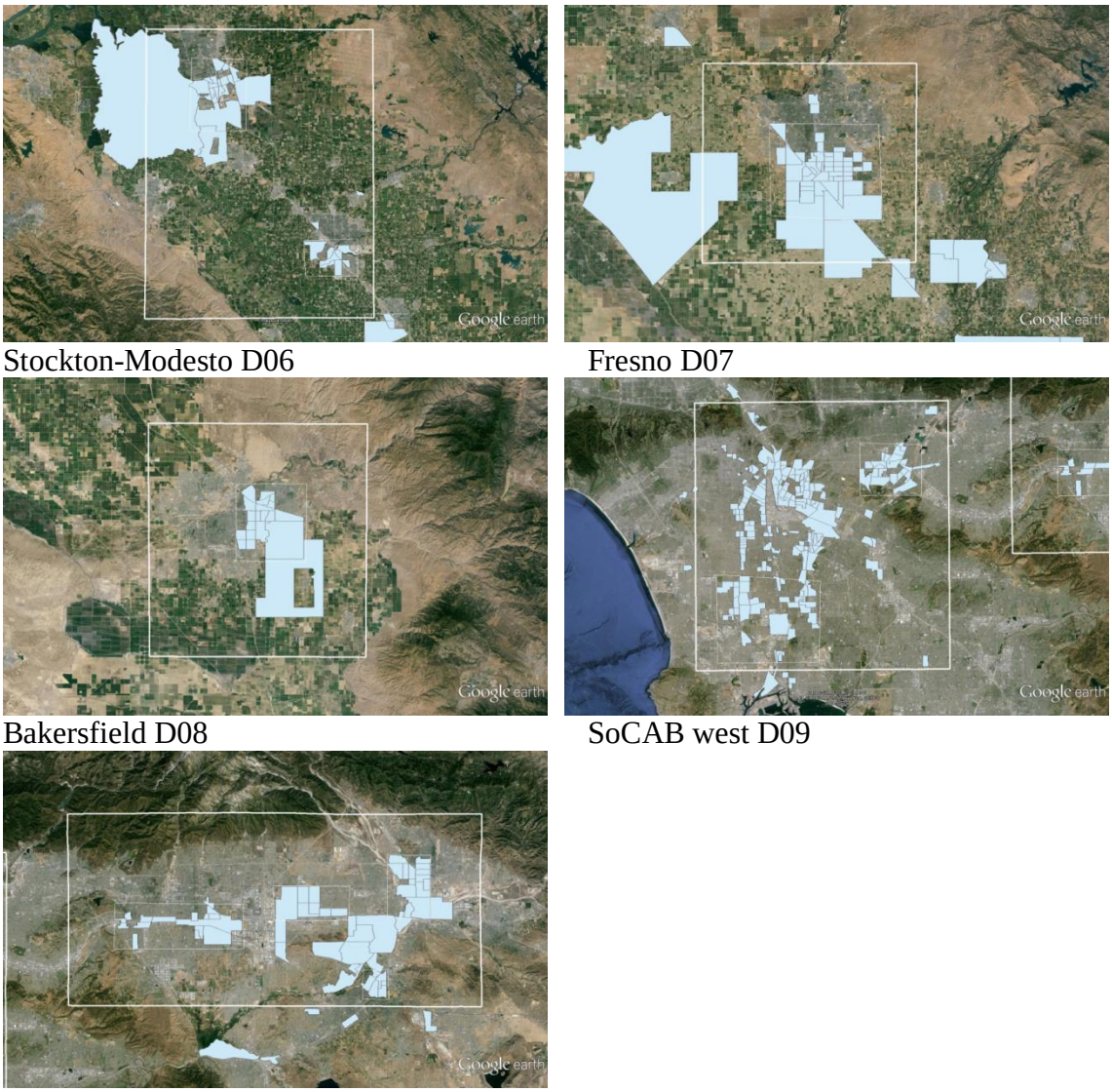

Stockton-Modesto D06

Fresno D07

Bakersfield D08

SoCAB west D09

SoCAB East D10

2.4. MODEL INPUT DATA

At the start of the project, model data needs were assessed and, as necessary, data were updated, generated, or acquired. Model input datasets needed for surface characterizations, atmospheric initial and boundary conditions, and derivations of the UHI Index (UHII) were developed, including:

A. **Meteorological initial and boundary conditions.** Four-dimensional (x,y,z,t) meteorological data were acquired for periods of June, July, and August (JJA) of 2013 and 2006. An additional month of data (May 2013 and 2006) was also acquired for use in model spin up. Thus data for MJJA for each of 2013 and 2006 were pre-processed and

prepared for use in the meteorological model. The data was obtained from the National Center for Environmental Prediction and the National Center for Atmospheric Research (NCEP / NCAR). The NCEP-NCAR Reanalysis Project (NNRP) datasets (Kistler et al. 2001) have 6-hourly temporal and ~200 km horizontal resolutions with 28 vertical (sigma) levels. The data are interpolated to finer resolutions both in space and time with the WRF preprocessor system (WRF WPS) discussed in Section 2.2, as initial and boundary conditions that are further dynamically downscaled by the meteorological model (WRF). The reanalysis data were also used in analysis nudging (four-dimensional data assimilation, FDDA) during model integration. The meteorological variables in these datasets are summarized in Table 3 and are in WMO GRIB format.

Table 3: NCEP/NCAR Reanalysis (NNRP) meteorological variables (Kistler et al. 2001).

Air Temperature	Albedo	Atmospheric Pressure	Atmospheric Stability
Cloud Amount/Frequency	Cloud Base Pressure	Cloud Top Pressure	Convergence/Divergence
Dew Point Temperature	Evaporation	Geopotential Height	Gravity Wave
Heat Flux	Humidity	Hydrostatic Pressure	Ice Extent
Incoming Solar Radiation	Land Cover	Long-wave Radiation	Maximum/Minimum Temperature
Outgoing Long-wave Radiation	Potential Temperature	Precipitable Water	Precipitation Rate
Pressure Tendency	Runoff	Sea Level Pressure	Sea Surface Temperature
Shortwave Radiation	Skin Temperature	Snow Water Equivalent	Soil Moisture/Water Content
Stream functions	Surface Air Temperature	Surface Pressure	Surface Roughness
Surface Winds	Temperature Tendency	Tropopause	Upper Level Winds
Vegetation Species	Vertical Wind Motion	Virtual Temperature	Vorticity

B. **Surface meteorological data.** Surface dataset for the periods MJJA of 2013 and 2006 were obtained from NCEP / NCAR as discussed above. These datasets complement the 4-dimensional reanalysis (item "A" above) and provide necessary 3-dimensional (x,y,t) surface-input information to the models, including such variables as surface temperature, sea-surface temperature, soil moisture, and so on. Other variables included in the datasets are summarized in Table 3.

C. **Observational meteorological data**. Observational meteorology datasets were obtained for the periods JJA of 2013 and 2006 from the National Weather Service (NWS) / National Oceanic and Atmospheric Administration (NOAA / NCDC). The data consists of surface and upper-air meteorological variables and derived quantities. In this modeling study, these observational data were used in carrying out quantitative model performance

evaluation as discussed in Section 3.4. They were also used in station / observational nudging (FDDA) in some of the earlier simulations. Furthermore, some surface-monitor networks, such as NOAA mesonets, WeatherBug, and Weather Underground, can provide high-resolution observational data of reasonable quality for general qualitative comparison with model results.

D. **Synoptic datasets and maps.** Available from NWS / NOAA, this dataset provides additional, semi-quantitative information to evaluate the model's ability in capturing the "big picture" including air-mass characteristics, fronts, high- / low-pressure systems and their migrations, general large-sale flow patterns, temperature, humidity, and other features. This will be discussed further in Section 3.4 on model performance evaluation.

There also exist a number of weather-data outlets and weather centers that further process these large-scale data and, in some cases, provide public-domain tools to produce graphical displays of synoptic maps, such as Unisys. In this project, the vertical levels of interest in upper-air model performance evaluation include those at 500, 700, 800, and 850 hPa (mb), focusing on the latter.

E. Land-use / land-cover (LULC).

a. United States Geological Survey (USGS) Level-II 30-m resolution LULC. This dataset was obtained from the USGS and recast from 30-m to 200-m resolution based on LULC-class majority. The Level-II LULC classification (Anderson et al. 2001) includes 37 categories, 7 of which are urban (categories 11 – 17) and represents years prior to 2000. The classification scheme is summarized in Table 4.

b. National Land Cover Data (NLCD) 30-m resolution LULC. This dataset was also recast to 200-m resolution based on class majority. In the NLCD classification system, there are 20 categories, 4 of which (21 – 24) are "developed" or urban. The data obtained for use in this study is NLCD 2011 (to represent most recent conditions and updates). The data was obtained from the Multi-Resolution Land Characteristics Consortium (MRLC 2014). The NLCD classification scheme is summarized in Table 5.

Whereas the basis for the USGS Level-II urban classification is relatively more functional, i.e., based on land-function typing (e.g., residential, commercial, industrial, etc.), the basis for the NLCD "developed" classification is relatively more physical, i.e., based on the extent or density of urban development (e.g., extent of impervious cover).

Because the NLCD 2011 data is more recent than the USGS Level-II data (pre-2000), there is, as expected, a difference in the size of urban areas represented in each dataset. As a result of growth since the late 1990s, the size of urban areas in the NLCD dataset is larger than that represented in the Level-II dataset. For example, in Figure 6 for Sacramento, California, the red/purple colors depict the Level-II extent of urban areas whereas the dark-grey colors represent those newer urban additions captured by NLCD data but not represented in the Level-II data. Figures 7 and 8 are additional examples that

highlight the different spatial extents of urban land use as represented in these two datasets.

Since the USGS Level-II classification scheme is relatively more resolved (functional) and thus more suitable for UHI-related modeling, the new, outlying NLCD-captured urban areas were mapped (in this study) into Level-II urban classes based on a cross-walk between the two classifications. The crosswalk was developed from our analysis of a domain encompassing the entire state of California with 498,060,234 cells (of 30 m resolution) representing 110,766,027 acres (slightly higher than the total area of California 104,765,440 acres because of a 10 km buffer used in the analysis). A compact summary of the crosswalk results is provided in Table 6, which represents the makeup of NLCD urban categories in terms of corresponding Level-II categories.

The LULC data prepared in this modeling effort were then remapped and referenced relative to latitude 37.0 and longitude -120.5 (with true latitudes of 30.0 and 60.0 and standard longitude of -120.5 in Lambert Conformal Projection to match the meteorological model's grid configurations).

Table 4. USGS Level-II classification system (Anderson et al. 2001).
Yellow highlights are urban classes cross-walked to NLCD urban classes listed in Table 5.

Level I	Level II
1 Urban or Built-up Land	11 Residential
	12 Commercial and Services
	13 Industrial
	14 Transportation, Communications, and Utilities
	15 Industrial and Commercial Complexes
	16 Mixed Urban or Built-up Land
	17 Other Urban or Built-up Land
2 Agricultural Land	21 Cropland and Pasture
	22 Orchards, Groves, Vineyards, and Ornamental Horticultural
	23 Confined Feeding Operations
	24 Other Agricultural Land
3 Rangeland	31 Herbaceous Rangeland
	32 Shrub and Brush Rangeland
	33 Mixed Rangeland
4 Forest Land	41 Deciduous Forest Land
	42 Evergreen Forest Land
	43 Mixed Forest Land
5 Water	51 Streams and Canals
	52 Lakes
	53 Reservoirs
	54 Bays and Estuaries
6 Wetland	61 Forested Wetland
	62 Non-forested Wetland
7 Barren Land	71 Dry Salt Flats.
	72 Beaches
	73 Sandy Areas other than Beaches
	74 Bare Exposed Rock
	75 Strip Mines Quarries, and Gravel Pits
	76 Transitional Areas
	77 Mixed Barren Land
8 Tundra	81 Shrub and Brush Tundra
	82 Herbaceous Tundra
	83 Bare Ground Tundra
	84 Wet Tundra
	85 Mixed Tundra
9 Perennial Snow or Ice	91 Perennial Snowfields
	92 Glaciers

Table 5. NLCD classification system (modified from source: MRLC 2014). Yellow highlights are "developed" classes cross-walked to USGS Level-II urban classes listed in Table 4.

	Class	Classification Description
Water	11	Open Water - generally with less than 25% cover of vegetation or soil.
	12	Perennial Ice/Snow - perennial cover of ice and/or snow, generally greater than 25% of total cover.
Developed	21	Developed, Open Space - mixture of constructed materials, but mostly vegetation in the form of lawn grasses. Impervious surfaces account for less than 20% of total cover. Large-lot single-family units, parks, golf courses, and vegetation planted in developed settings.
	22	Developed, Low Intensity - mixture of constructed materials and vegetation. Impervious surfaces account for 20% to 49% percent of total cover. Single-family housing units.
	23	Developed, Medium Intensity –mixture of constructed materials and vegetation. Impervious surfaces account for 50% to 79% of the total cover. Single-family housing units.
	24	Developed High Intensity -highly developed areas where people reside or work in high numbers. Apartment complexes, row houses and commercial/industrial. Impervious surfaces account for 80% to 100% of the total cover.
Barren	31	Barren Land (Rock/Sand/Clay) - bedrock, desert pavement, scarps, talus, slides, volcanic material, sand dunes, strip mines, gravel pits. Vegetation accounts for less than 15% of total cover.
Forest	41	Deciduous Forest - dominated by trees greater than 5 meters tall, and greater than 20% of total vegetation cover. More than 75% of the species shed foliage in response to seasonal change.
	42	Evergreen Forest - dominated by trees generally greater than 5 meters tall, and greater than 20% of total vegetation cover. More than 75% of the species maintain their leaves all year.
	43	Mixed Forest - dominated by trees generally greater than 5 meters tall, and greater than 20% of total vegetation cover. Neither deciduous nor evergreen species are greater than 75% of total tree cover.
Shrubland	51	Dwarf Scrub - Alaska only areas
	52	Shrub/Scrub - dominated by shrubs; less than 5 meters tall with shrub canopy typically greater than 20% of total vegetation.
Herbaceous	71	Grassland/Herbaceous - dominated by herbaceous vegetation, greater than 80% of total vegetation.
	72	Sedge/Herbaceous - Alaska only areas
	73	Lichens - Alaska only areas
	74	Moss - Alaska only areas
Planted	81	Pasture/Hay – grasses, legumes planted for livestock grazing or the production of seed or hay crops. Pasture/hay vegetation accounts for greater than 20% of total vegetation.
	82	Cultivated Crops –used for the production of annual crops, and also perennial woody crops. Crop vegetation accounts for greater than 20% of total vegetation.
Wetlands	90	Woody Wetlands - forest or shrubland vegetation accounts for greater than 20% of vegetative cover and the soil or substrate is periodically saturated with or covered with water.
	95	Emergent Herbaceous Wetlands - perennial herbaceous vegetation accounts for greater than 80% of vegetative cover and the soil or substrate is periodically saturated with or covered with water.

Figure 6. Example LULC map for Sacramento, California showing 1) census-tract centroids (green dots), 2) USGS Level-II urban areas (red/pink), and 3) newer developed urban areas captured by NLCD datasets (dark grey).

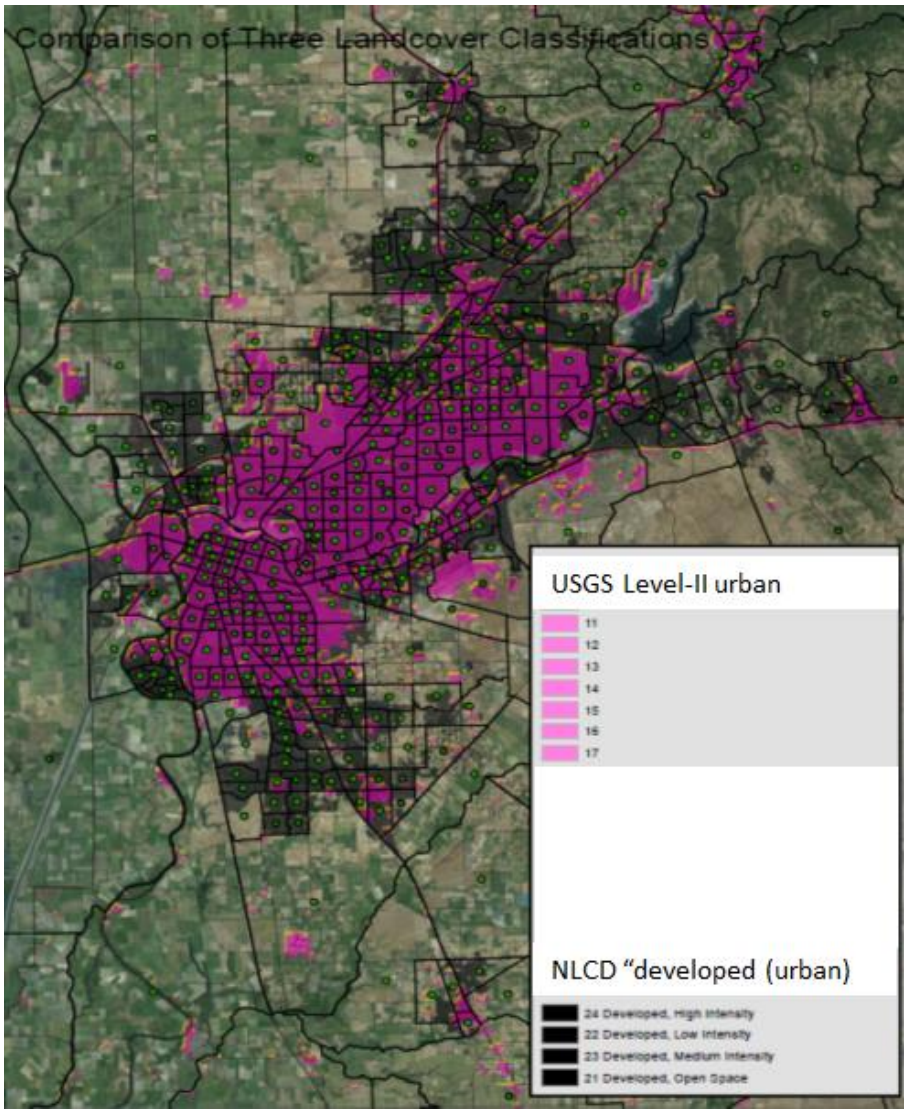

Figure 7. Urban land-use classes in USGS Level-II and NLCD for the San Francisco Bay Area – Sacramento region.

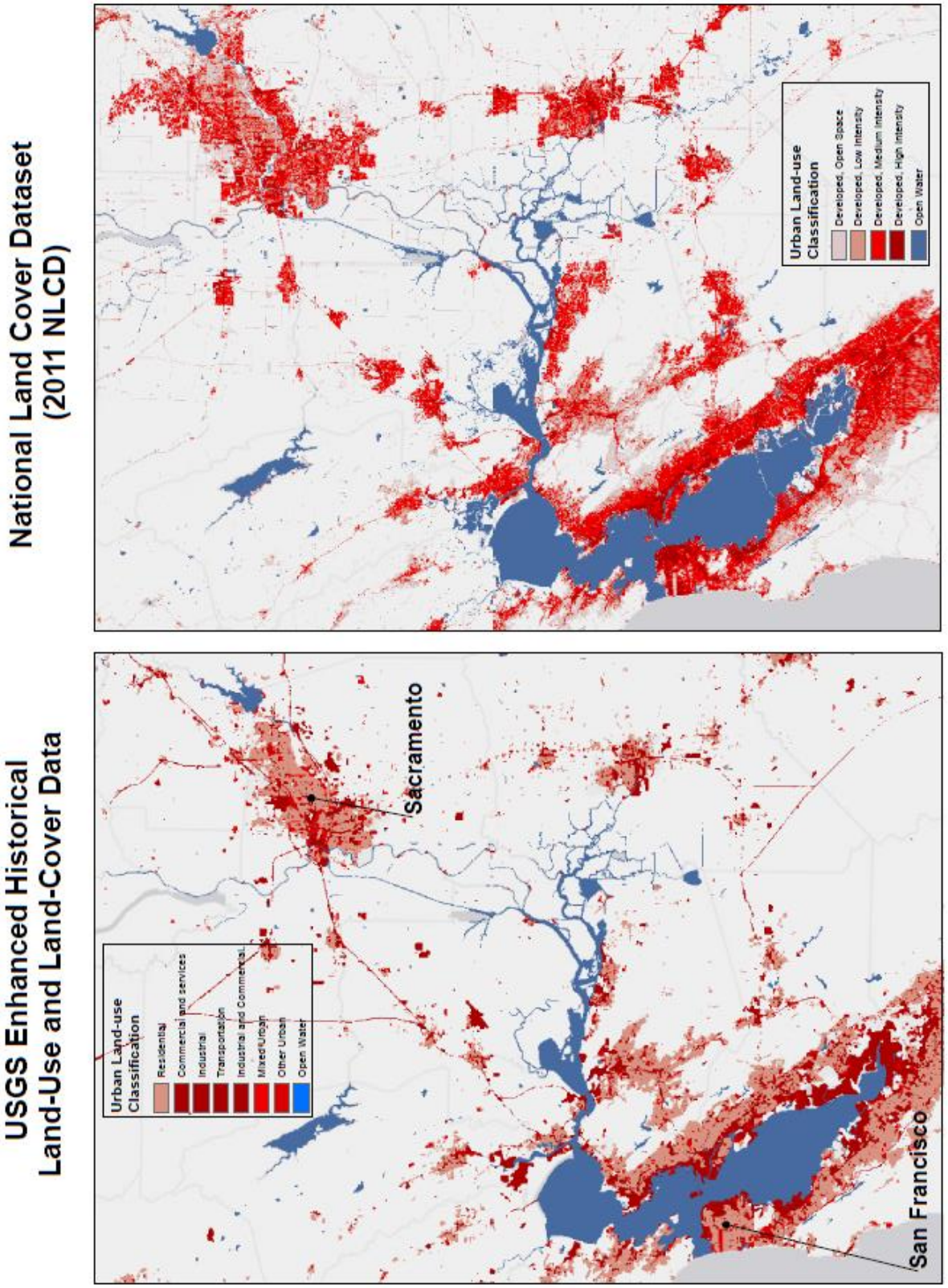

Figure 8. Urban land-use classes in USGS Level-II and NLCD for California.
Of note the urban archipelagos in Santa Clara Valley and Los Angeles (particularly west basin).

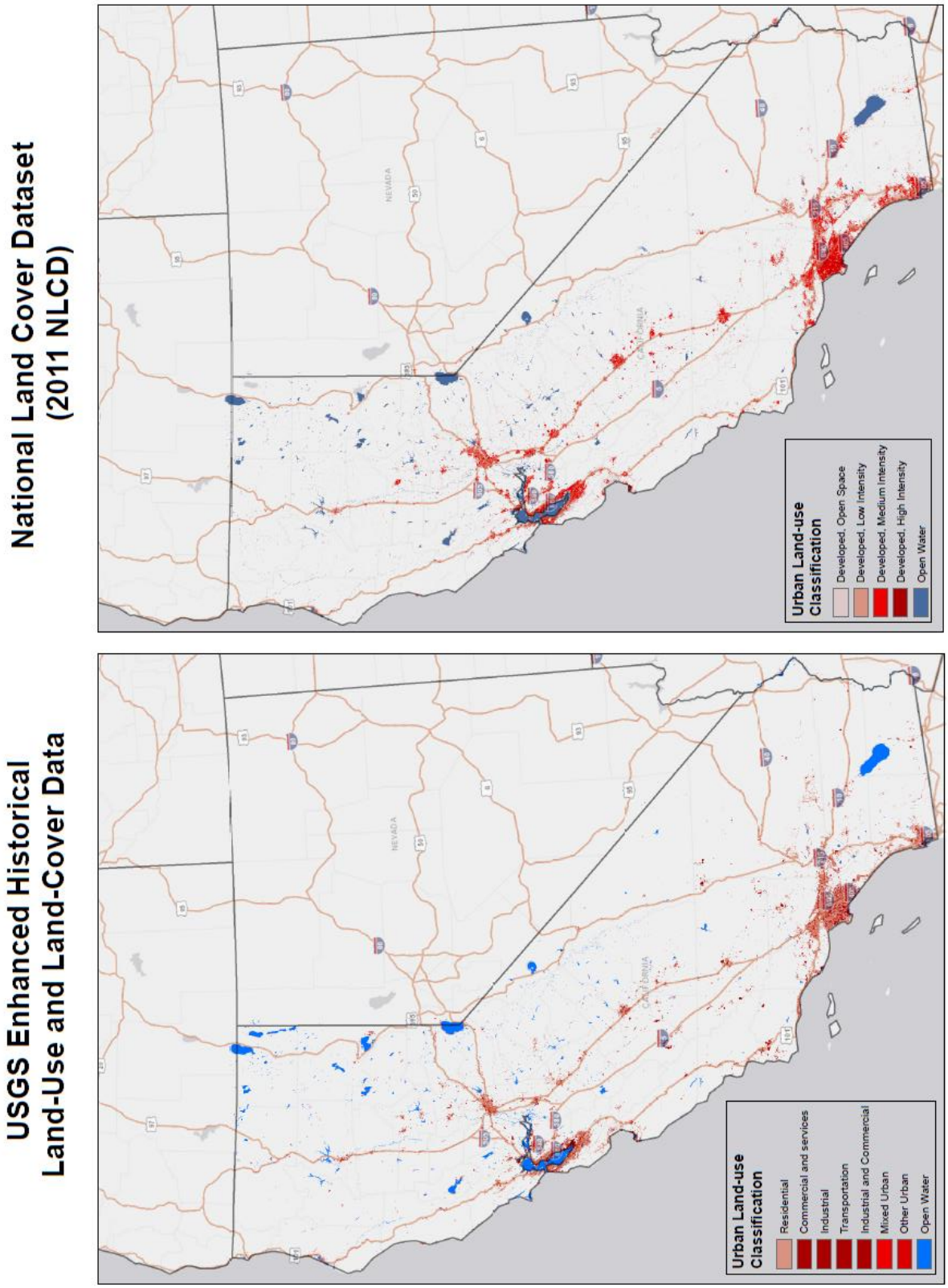

Table 6. Summary of crosswalk between urban NLCD and USGS Level-II classes in California.

		Urban USGS Level-II classes (L2)						
	crosswalk	11 resid	12 comm/srv	13 industr	14 transp.	15 ind/com	16 mixed	17 other
k↓	**Urban NLCD classes**	$f_{j,k}$						
21	Developed, open space	0.58	0.11	0.07	0.08	0.00	0.01	0.13
22	Developed, low intensity	0.73	0.11	0.04	0.07	0.00	0.01	0.05
23	Developed, med. intensity	0.64	0.19	0.06	0.06	0.01	0.01	0.04
24	Developed, high intensity	0.25	0.36	0.22	0.09	0.02	0.02	0.03

In areas with urban NLCD data but no urban USGS Level-II data, the characterization is based on a crosswalk from NLCD to USGS Level-II urban classifications as in Table 6. Thus characterizing a physical parameter (*P*) in NLCD based on Level-II (*L2*) classification is done as:

$$P(NLCD_k) = \sum_{j=11}^{17} \{P(L2_j) \times f_{j,k}\} \qquad (4)$$

where *k*: 21, 22, 23, 24; *j*:11, 12, 13, 14, 15, 16, 17; and *f*: fraction as a function of *j* and *k*, and given in Table 6.

F. **Census tract centroids.** In order to establish a spatial referencing system whereby output from the meteorological model can be assigned to each census tract in California, centroids (central coordinates) were computed in this study for each tract. As seen in the Sacramento example in Figure 6, the green dots represent the computed centroids for each tract in the region. These centroids were used (see Section 3.5) to map and color-code the output from the meteorological model based on assigned UHII value and ranges (model variables were extracted at each centroid).

G. **Population.** Based on most recent data (year 2012), population density was re-projected to model coordinates and re-gridded at 1 km resolution per model grid configuration and relative to the domain's central latitude and longitude. As discussed later in Section 3.5, population density was used as a threshold for mapping the UHII on census tracts.

H. **Morphology crosswalk.** This dataset provides additional geometrical information used to develop certain parameters for the 1-km simulation domains. These include roughness

length and drag coefficients, as well as effective albedo. The urban morphology crosswalk for California was based on a combination of NUDAPT data supplemented by Google Earth data, using a methodology developed by Taha (2008a-c) in prior studies. Following this approach, morphological parameters were derived, as necessary, based on the USGS Level-II and NLCD classifications discussed in item "E" above. The main morphological parameters of interest include, both for buildings and vegetation canopies, fine-resolution horizontally- and vertically-varying plan-area densities, frontal-area densities, top-area densities, sky-view factors, roof-to-plan ratios, top-to-plan ratios, wall-to-plan ratios, and street orientations.

I. **Satellite data of surface albedo**. Although ultimately not used in this study, we also acquired at the beginning of the project remotely-sensed surface albedo data developed by the Lawrence Berkeley National Laboratory in an ARB-sponsored study (Ban-Weiss et al. 2014). The reason for not using this data was that it characterizes roof albedo but not that of other land cover (i.e., a partial characterization) whereas the model requires albedo characterizations over entire grid cells and modeling domains, including other land cover. Thus, direct comparisons of grid-cell albedo and roof albedo are not feasible.

2.5. MODEL MODIFICATIONS AND CUSTOMIZATIONS

In this section, model customizations carried out in this study are discussed. It is to be noted that the model configurations and modifications selected for this application may not nessecarily be the best options but the most optimal ones to ensure even and uniform applicability across all areas in California.

2.5.1. Modifications to land-surface model

There are a number of parameterizations and modules in the Weather Research & Forecasting model (WRF) that have relatively more relevance to modeling and analysis of urban climates, in this case, quantifying urban heat islands (UHI) and deriving the UHI Index (UHII). These modules parameterize the urban surface-atmosphere exchanges of momentum, heat, moisture (Dupont et al. 2005), turbulent kinetic energy (Dupont et al. 2004, Martilli et al. 2002, Bougeault and Lacarrere 1989), and urban-specific fluxes such as anthropogenic heating (Sailor and Lu 2004, Fan and Sailor 2005).

One relevant module in relation to this project's application is the NOAH land-surface model (Pleim et al. 2001), where most urban surface-atmosphere heat and moisture fluxes and exchanges are parameterized. In this study, some aspects of this model were modified. One customization was to modify the process of LULC and thermo-physical characterization of the lower boundary / surface at various domain levels for input to the NOAH LSM, particularly in areas designated as urban. The goal of this modified approach is to preserve the fine-scale urban features and details of the surface as much as possible (which is important in better characterization of the UHI and computing the UHII at finer scales). Thus characterization is

done at fine resolution independently at each grid level (for each nest). Furthermore, unlike in the standard WRF processing where surface characterization is done by association with the dominant land-use / land-cover class (LULC majority), two modifications were carried out in this study:

a. For the 1-km domains (D06-D10), up-scaling was done from 30 m to 200 m via LULC majority (via dominant LULC), then from 200 m to 1 km by physical characterization (averaging or weighing physical properties), see Figure 9a; and

b. For the 3-km domains (D03-D05), up-scaling was done from 30 m to 200 m to 1 km by LULC majority (via dominant LULC), then from 1 km to 3 km by physical characterization, see Figure 9b.

Figure 10 summarizes these different up-scaling pathways and characterizations of the model's lower boundary (surface / urban areas) in terms of required parameters such as albedo, soil moisture, roughness length, canopy cover, and others. This approach can provide better resolution (since it assigns physical properties starting at the 200-m level). In assigning thermo-physical properties in this study, the basis was prior urban-fabric analysis by Akbari et al. (1999), Rose et al. (2003), and Taha (2007,2008a-c, 2013a,b).

Figure 9: Study-modified approach. **a)** Up-scaling of 200-m LULC to 1-km thermo-physical characterization, example: D06; **b)** Up-scaling of 1-km LULC to 3-km thermo-physical characterization, example: D03.

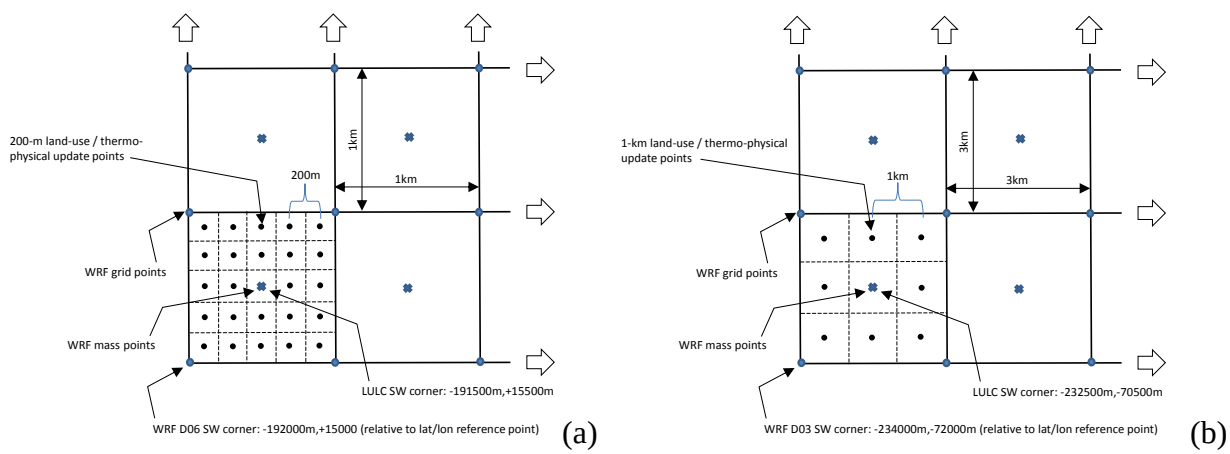

Figure 10: Up-scaling of 30-m properties and development of surface thermo-physical characterizations for the model's 1- and 3-km domains as in this study's modified approach.

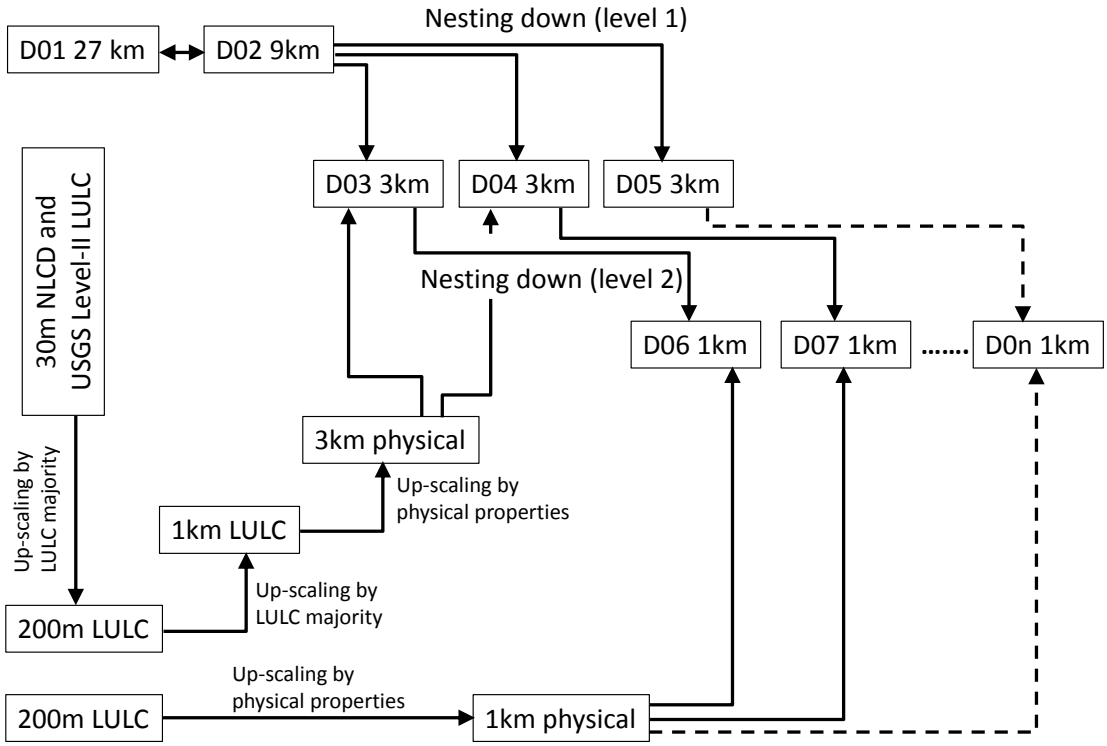

Following that process, the properties of urban points in each grid cell were meshed with those of their non-urban surroundings, i.e., portions of cells that are non-urban, by weighing the respective physical properties by the fractions *urbfra* and *1-urbfra*, where *urbfra* is defined as in Figure 11. This is an improvement over the way urban and non-urban land uses within urban grid cells are characterized by default in WRF. In the WRF urban parameterizations, the non-urban part of an urban grid cell is reverted to a single default category. When an urban module such as UCM is used, the non-urban part of each urban grid cell is assigned a single land-cover category which, in the USGS LULC system, is classified as "cropland/grassland mosaic" regardless of what existed in that grid cell originally. In the modified approach, the *1-urbfra* characteristics are those of the land use/land cover originally in that grid cell, meshed with the properties of the *urbfra* part which comes from the updated characterizations performed in this study. This is clarified further in Figure 11.

Figure 11: Meshing of urban physical properties (from this study's datasets) with WRF non-urban physical properties. The shaded area represents the LULC that exists in WRF (for a given grid cell) and the dots represent data points from the study-derived urban parts of the cell and their physical properties.

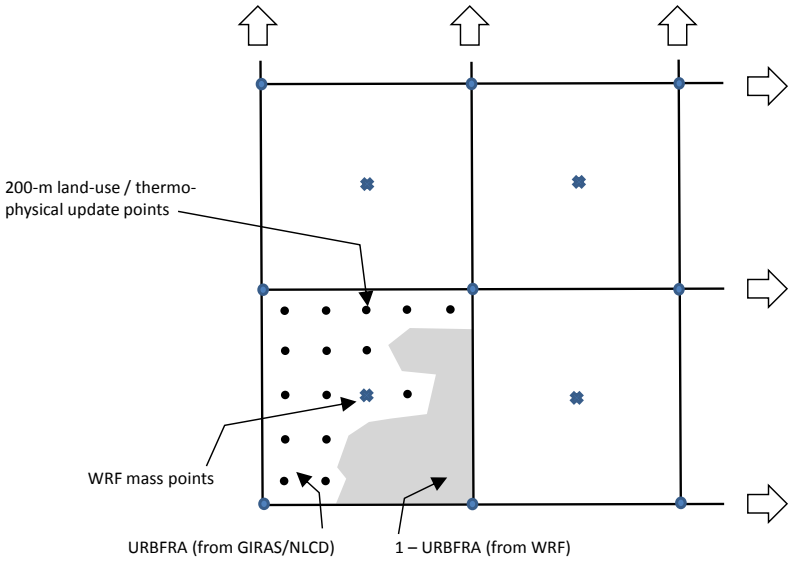

The effects of urban areas in the model are typically characterized via specification of certain physical parameters including 1) effective albedo, 2) roughness length, 3) vegetation cover (canopy cover / shade factor), 4) soil moisture content, 5) plan-area and frontal-area densities for buildings and vegetation, 6) emissivity, and 7) anthropogenic heating. These parameters were assigned to urban LULC based on in-house data from prior field studies and fabric analysis which we have undertaken in the past, as discussed above. Furthermore, in implementing these modifications in the NOAH LSM, a distinction was made in this study between 1) "above-canopy" and "below-canopy" vegetation cover, as discussed in Section 2.5.3 below. The former mainly affects shading whereas the latter mostly affects soil moisture.

2.5.2. Downscaling and input to sub-domains

A nest-down (WRF NDOWN) approach was adopted for the finer grids of the configuration shown in Figure 4. Domains D01 and D02 were run with two-way feedback as well as analysis nudging 4-dimensional data assimilation (FDDA). Domains D03 through D10 were downscaled with WRF's NDOWN procedure that was modified in this study for the specifics of ingesting USGS Level-II and the more recent NLCD urban data as shown in Figure 10. Thus, the modeling was configured in two "tiers": 1) Downscaling from D02 to D03, D04, and D05; and 2) Downscaling from D03 to D06 and D07; from D04 to D08; and from D05 to D09 and D10.

The purpose of using NDOWN in this manner is to allow for generation of urban input for each sub-domain separately (as discussed above and shown in Figure 10), that is, using a bottom-up approach. There are some benefits in adopting this approach relative to more standard WRF input processing. These include:

1. The modified approach provides significant control over LULC input to and physical properties characterizations in the model which allows the simulation of scenarios that are exactly as specified by the modeler;
2. The modified approach allows, if necessary, to simulate the effects of upwind re-construction of urban areas to characterize the length-scale / fetch effect for UHII adjustment to transport of heat (which is needed in Level-3 and Level-4 UHII modeling discussed in Section 2.1);
3. The modified approach establishes the basis and a reference state (in the code) for possible future modeling of UHI mitigation measures (e.g., cool cities / cool communities) which will allow for adjusting the UHII calculations to include mitigation potential. This will require specification of physical properties for modification, such as changes in albedo, vegetation cover, or others, on a cell-by-cell or census tract-by-tract basis which will be difficult to undertake with the standard WRF processing;
4. The modified approach, as discussed above, helps preserve fine-resolution details of the surface / urban areas better (e.g., Figure 12);
5. The modified approach allows for the application of specialized urban WRF modules (e.g., UCM/BEP/BEM), if desired, on a selective basis (user-specified) that can be run along with those areas where default/lookup urban LULC triggers the urban schemes (e.g., for Levels 3 and 4 UHII modeling and where site-specific surface characterizations are available); and
6. In future work, and if so desired, the modified approach will allow perturbing or modifying a single census tract, or selected tracts, to evaluate the potential for mitigation of the local UHI, i.e., to show the potential for UHII attainment. This can be done by selectively triggering the urban models or the new parameterizations in the modified approach.

These features of the modified approach, such as No. 3 and 6, are useful in allowing for flexibility to modify land-use and surface physical properties and evaluate the benefits of mitigation pathways under various scenarios.

Several modules were modified to accept the modified input data developed in this effort. Figure 12 shows examples of model-produced skin-surface and air temperatures (of relevance to UHII), and perturbations thereof, generated with the modified approach (for an arbitrary test domain over the San Francisco Bay Area). Of note, changes in skin-surface temperature are presented in this example because these changes are more closely tied to perturbations in surface properties than are changes in air temperature. However, all UHI and UHII calculations and characterizations in this study and all final products are in terms of air temperature.

Figure 12a shows that relative to standard WRF processing of LULC, the modified approach produces slightly higher skin-surface temperatures due to enhanced urban land-use characterization. It also captures fine-scale urban detail better (e.g., highways and towns). The scale on the figure is intentionally constructed so as to show only contrasts and not a range of values. The goal is to depict details that can be captured with the modified approach. Thus in Figure 12a, the light green color represents roughly the areas classified as urban in standard WRF processing (temperature difference is between 0 and 1.5°C). On the other hand, the dark-

green color represents additional areas classified as urban in the modified approach (temperature difference of 2-4°C). Figure 12b shows the corresponding difference in terms of air temperature between the modified approach and the standard WRF.

Figures 12c and 12d depict the changes in skin-surface and air temperatures, respectively (both produced by the modified approach), that would result from a hypothetical scenario of increased urban albedo. The goal was simply to test the model modifications' functionality and to examine the areas affected by changes in temperature.

Figure 12. **a)** Skin-surface temperature difference (C°) **B – A** at 1300 PDT, 8 Jul 1999, San Francisco Bay Area – Stockton domain; **b)** 2-m air-temperature difference (C°) **B – A** at same hour. In this case, **A:** temperature from NDOWN using standard configurations; **B:** temperature from study-specific model customization in addition to NDOWN (1-km resolution); **c)** Skin-surface temperature difference (C°) **C – B** at 1100 PDT, 8 Jul 1999; **d)** 2-m air temperature difference (C°) **C – B** at same hour. In this case, **C:** temperature from hypothetical test case with 50% albedo increase on urban surfaces (study modifications+NDOWN). Compare with Figure 17, domain D06_SFBA.

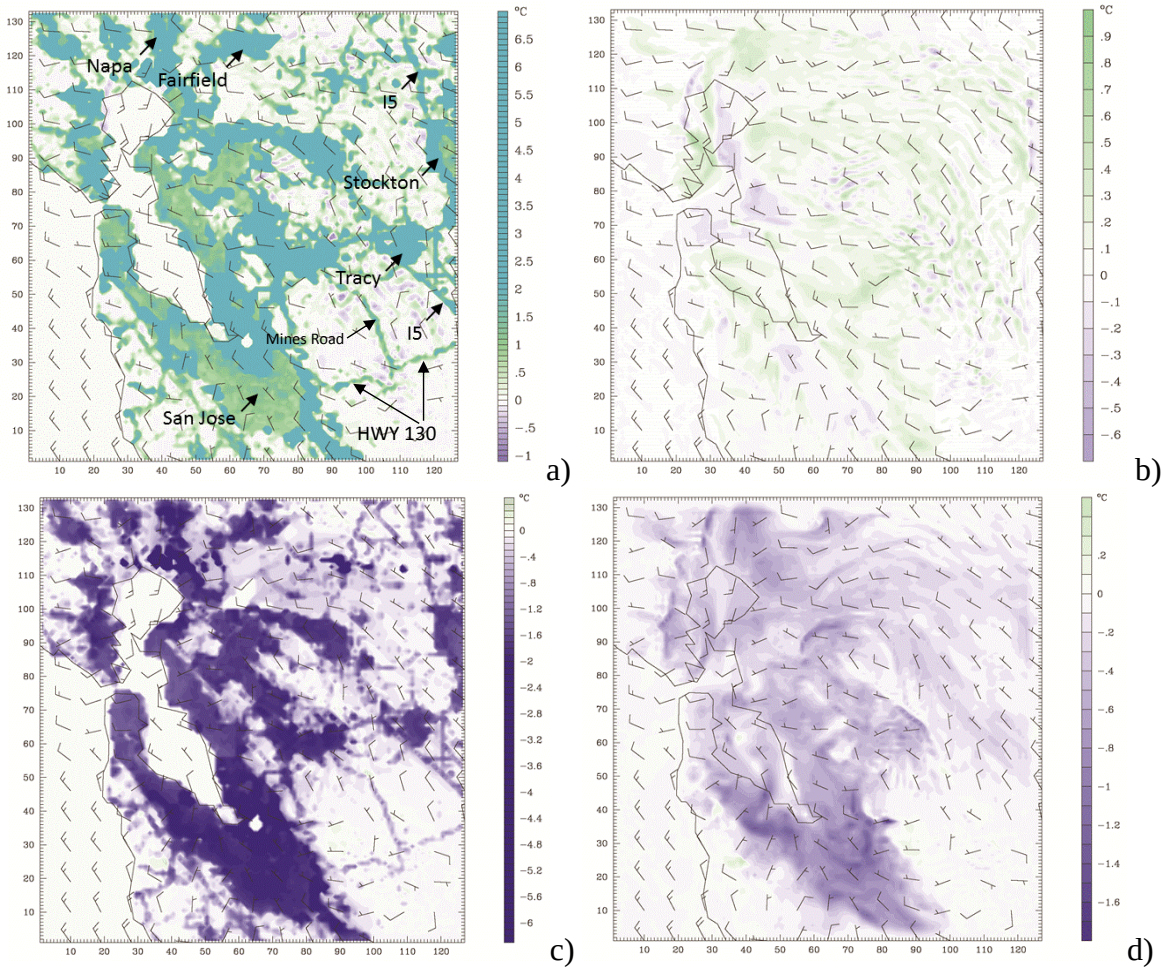

The modified approach, applied to the NOAH LSM as discussed above, was used with WRF modules and options including: 1) NNRP reanalysis input along with NOAA/NWS observations; 2) analysis nudging (FDDA) in coarse grids (27+9 km); 3) microphysical options with simple ice scheme; 4) rapid radiation-transfer model (RRTM) for long-wave radiation; 5) Dudhia shortwave radiation scheme; 6) Janjic ETA Monin-Obukhov surface-layer physics scheme; 7) boundary-layer scheme of Mellor-Yamada-Janjic (ETA TKE scheme); 8) cumulus parameterizations using the Kain-Fritsch (ETA) scheme; 9) 6th order numerical diffusion scheme (when using urbanized modules), 10) 5th order horizontal advection scheme, and 11) positive-definite moisture advection scheme.

These technical concepts, schemes, and their scientific basis are discussed in detail in the WRF documentations (Skamarock et al. 2008) and are not repeated in this report. Additionally, related information can be found in Dudhia (1993), Grell et al. (1991,1994), Hong and Pan (1996), Liang et al. (2012), Pan and Mahrt (1987), Stensrud (2007), and Kalnay (2003).

2.5.3. Modified albedo and canopy-cover representations

a. Albedo. As discussed above, the thermo-physical characterizations at the 3-km and 1-km levels were carried out in a multi-tiered approach (Figure 10). The starting point is the assignment of physical properties at the 30- and 200-m resolutions level.

   For the purpose of UHI modeling, physical properties are assigned at the 200-m level by taking into account the surface and fabric makeup at that scale and properties (e.g., albedo, roughness length, soil moisture, thermal inertia, emissivity, etc.) for each surface type within a 200-m cell. These are then weighted by respective land cover to develop a 200-m representative characterization. The analysis involves surface characterization including, for example, roofs, pavements, streets, parking lots, vegetation canopy (with various underlying surfaces), ground cover, green roofs, water, pools, barren land, and so on (Akbari et al. 1999, Rose et al. 2003). The physical properties are then mapped to 200-m resolution and cross-walked to the USGS Level-II classification. For albedo, the values from the California analysis are as in Table 7. As discussed in Section 2.5.1, these values are assigned to each LULC point (Figure 11) and then weighted by the corresponding *urbfra* and *1-urbfra* fractions in each urban cell.

Table 7: Assignment of 200-m albedo

USGS Level II urban LULC	Effective albedo
11	0.157
12	0.139
13	0.152
14	0.117
15	0.145
16	0.134
17	0.142

b. Canopy cover. In the field, canopy cover is usually characterized with in-situ measurements of the stand's geometry and attributes. This approach, while accurate and very site-specific, is also tedious and limited in aerial extent. A more generalized approach relies on using remote-sensed data, such as characterizing vegetation cover using NDVI (Normalized Difference Vegetation Index). This approach has limitations as well, e.g., possible errors in distinguishing among different surface types. Furthermore, these canopy characterizations are not correlated to certain LULC classifications, which is important for even characterization of large areas in California, as in this study, and in developing mitigation scenarios, e.g., cool cities, for modeling and assessment of benefits in the future.

Thus in this study, vegetation cover was also characterized based on the work of Akbari et al. (1999) and Rose et al. (2003) as discussed above for albedo. By calculating the difference between "below-the-canopy" and "above-the-canopy" perspectives, the above-ground canopy cover was quantified. For example, in a fully urbanized area (completely urbanized 30-m cell), the typical shade factor in California is 0.05. This is then weighted by the shade factor of various other land covers and urban areas and the fractions of non-urban LULC in each urban grid cell.

For the sake of comparison, the value of 0.05 for full-urban shade factor is similar to 1) urban-assigned value in WRF NOAH modules (e.g., noahlsm.F), 2) as an approximate value to those assigned to urban LULC in WRF vegetation parameterizations (vegparm.tbl) and land-use parameters (landuse.tbl), and 3) similar to values in Rose et al. (2003) where cover for above- and below-canopy fabric for several U.S. cities (including California) was characterized (above-minus-below canopy cover was found to be about 4-6% on average). That detailed fabric analysis for several U.S. cities also found a relatively narrow range of fabric makeup variability across similar land uses. Table 8 provides example characterizations of a few surface types in four U.S. regions. Figures 13a and 13b show the albedo and shade factor fields resulting from the modified approach for the San Francisco Bay area domain as an example.

Table 8. Comparison of the fabric (%) of Salt Lake City UT, Sacramento CA, Chicago IL, and Houston TX areas (Rose et al. 2003).

City	Vegetation	Roofs	Pavements	Other	A-B**
Above-the-canopy					
Metropolitan Salt Lake City	40.9	19.0	30.3	9.7	7.6
Metropolitan Sacramento	28.6	18.7	38.5	14.3	8.3
Metropolitan Chicago	30.5	24.8	33.7	11.0	3.8
Metropolitan Houston	38.6	21.4	29.0	10.9	1.5
Residential Salt Lake City	46.6	19.7	25.3	8.5	8.0
Residential Sacramento	39.2	19.4	25.6	15.8	6.4
Residential Chicago	44.3	25.9	25.7	4.1	8.5
Residential Houston	48.9	20.5	24.7	6.0	1.5
Under-the-canopy					
Metropolitan Salt Lake City	33.3	21.9	36.4	8.5	-
Metropolitan Sacramento	20.3	19.7	44.5	15.4	-
Metropolitan Chicago	26.7	24.8	37.1	11.4	-
Metropolitan Houston	37.1	21.3	29.2	12.4	-
Residential Salt Lake City	38.6	23.9	31.6	6.0	-
Residential Sacramento	32.8	19.8	30.6	16.8	-
Residential Chicago	35.8	26.9	29.2	8.1	-
Residential Houston	47.4	21.1	23.9	7.6	-

****A-B** is the difference computed as "above the canopy" minus "below the canopy" vegetation cover. This is a proxy for shade factor ("shdfac") and is similar in magnitude to the value used in this study.

Figure 13. a (left): 1-km surface albedo based on the modified approach and meshed with WRF albedo, **b (right)**: 1-km shade factor based on modified approach and meshed with WRF shade factor. Example shown for the SFBA domain (Figure 17, domain D06_SFBA).

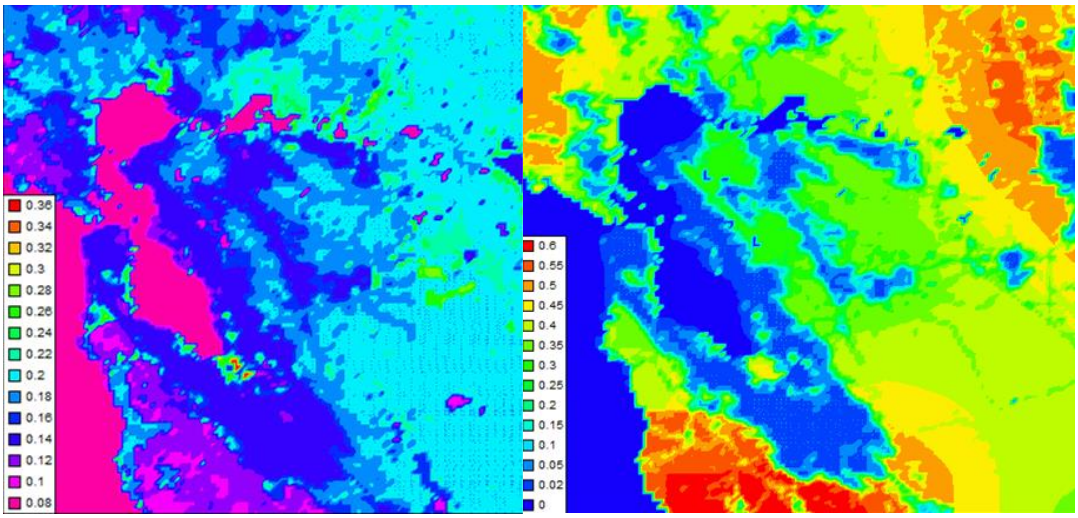

2.5.4. Roughness length parameterizations

For the aerodynamic roughness-length parameter (Z_0), three approaches were evaluated: 1) the WRF Z_0 assignment per LULC lookup; 2) study-modified Z_0 calculations based on LULC-properties weighting; and 3) study-modified hybrid Z_0 formulation.

a. The first approach relies on using Z_0 values that are assigned as functions of LULC categories and specified in lookup tabulations in the model. These values are based on literature data and field measurements.

b. In the second approach, Z_0 was computed at the 200-m level for various LULCs and the final grid-cell-level Z_0 was computed as (Taha 1999):

$$\overline{Z_0} = \prod Z_{0i}^{Ai/A} \qquad (5)$$

where the overbar indicates grid-cell level roughness length (e.g., at 200 m or 1 km) for the urban part of the cell, Z_{0i} is roughness length for urban LULC "*i*", A_i is the area occupied by urban LULC "*i*', and *A* is the total urban area within a grid cell (non-shaded area in Figure 11). Equation 5 is then applied again to weight by urban (*urbfra*) and non-urban (*1-urbfra*) parts of an urban grid cell (Figure 11).

c. In the third approach, Z_0 was computed based on frontal-area and plan-areas indexes and drag coefficient, using a formulation by MacDonald et al. (1998) and weighted by urban and non-urban fractions as above. First, Z_0 was computed as follows:

$$\frac{Z_d}{Z_h} = 1 + \alpha^{-\lambda p}(\lambda p - 1) \qquad (6)$$

$$\frac{Z_0}{Z_h} = \left(1 - \frac{Z_d}{Z_h}\right) \exp\left[\!\left[- \left\{0.5\,\beta\,\frac{C_d}{k^2}\left(1 - \frac{Z_d}{Z_h}\right)\lambda f\right\}^{-0.5}\right]\!\right] \qquad (7)$$

where Z_d is displacement height, Z_h is roughness element height, α is a constant, λp is plan-area density, β is a constant, C_d is drag coefficient, k is von Karman constant, and λf is frontal-area density. Roughness length computed with equations 6 and 7 was then weighted, as discussed in Section 2.5.1, by urban and non-urban fractions of each urban cell (Figure 11).

For approach *c*, the source of plan-area density parameter (λp) was NUDAPT, Google Earth, and other morphology information discussed earlier in Section 2.4 (item H). However, the sparse coverage of NUDPAT data was one factor against use of such approach in this study. And while the original source of frontal-area density (λf) data is Burian et al. (2003a,b), λp was derived in this study from the data itself. First, the makeup of each urban USGS Level-II class was characterized in terms of urban NLCD composition based on the crosswalk from USGS Level-II classes, as in Table 9. Then based on the NLCD urban characterizations, the impervious cover was characterized as in Table 10. In this table, the range of impervious cover (2nd column) is from the NLCD/USGS data description (Table 5).

Table 9: Crosswalk from USGS to NLCD urban classes.

	NLCD 21 (Developed, Open space)	NLCD 22 (Developed, Low intensity)	NLCD 23 (Developed, Medium intensity)	NLCD 24 (Developed, high intensity)
USGS Level II				
Residential	0.203	0.317	0.433	0.047
Commercial / Services	0.141	0.170	0.448	0.241
Industrial	0.207	0.129	0.316	0.348
Transp., Comm., Util.	0.256	0.255	0.340	0.149
Industrial / commercial	0.017	0.061	0.476	0.447
Mixed urban	0.193	0.212	0.391	0.204
Other urban	0.449	0.218	0.270	0.063

Table 10: Impervious and roof area for NLCD urban classes.

NLCD urban	Impervious	Average impervious	Resulting roof area (or λp)
21	≤ 20%	10%	5%
22	20% - 50%	35%	16%
23	50% - 80%	65%	58%
24	≥ 80%	90%	44%

An average impervious cover for each NLCD urban class was defined as the midpoint of the corresponding range in Table 10. Then, the ratio of roof area to total impervious area was derived from the fabric analysis of several cities (Rose et al. 2003, Akbari et al. 1999, Taha 2007,2008a-c). For California, typical roof-to-impervious area ratios are: 43% for USGS LULC 11; 28% for LULC 12; 45% for LULC 13; 5% for LULC 14; 30% for LULC 15; and 42% for LULC 16 and 17. These ratios applied to each NLCD class in Table 9 (and weighted by USGS classes) result in a factor, which when multiplied by the average impervious percentages yield the λp values in the last column of Table 10 (for example, for the first NLCD category in Table 9, we compute 0.43×0.203 + 0.28×0.141 + 0.45×0.207 + 0.05×0.256 + 0.30×0.017 + 0.42×0.193 + 0.42×0.449 = 0.5075, which, when multiplied by 10% in Table 10, results in λp of 5%). For the purpose of calculating roughness length for buildings, roof area fraction was used as an indicator to plan-area index.

The three approaches (a, b, and c) were tested and the results show a range of roughness length values. Such variations were also noted, for example, by Grimmond and Oke (1999) and Carter et al. (2012). During initial model performance evaluations (also discussed in Section 3.4) it was noted that performance was best with the first approach (a), thus it was used in the final simulations. Figure 14 depicts the roughness length parameter for the San Francisco Bay Area domain, as an example.

Figure 14: 1-km roughness length (m) in the example SFBA domain D06_SFBA.

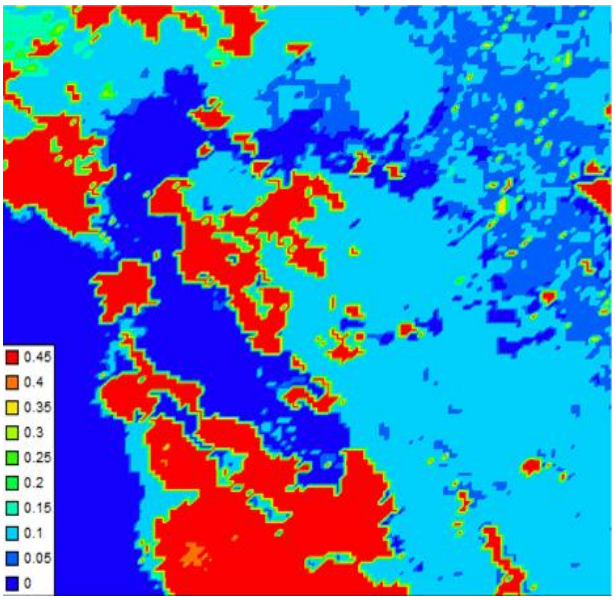

2.5.5. Development of selective application of uWRF

A procedure was developed to selectively trigger the application of urban WRF sub-models in user-selected grid cells. The process was tested with the urban canopy model (UCM) but the approach is equally applicable with other uWRF sub-models. In the standard WRF, urban modules are applied (triggered) at certain grid cells that meet the trigger criterion, i.e., encountering a cell that is classified as "urban" in the old system or as NLCD categories 21, 22, 23, or 24 in the new system (Table 5), if available.

In the study-modified approach, the trigger was set to 1) any grid cell (or group of cells) manually defined by the user and/or 2) whenever the model encounters any user-specified LULC categories from the USGS Level-II or NLCD classifications (e.g., up-scaled characterizations in Figure 10). Thus in this approach, the user has more control over where to apply the urban modules or combinations of modules. This is useful in the assessment of length scale (where urban areas are re-constructed upwind), and in the modeling of cool-city scenarios (in the future) where additional control over surface properties is important. The modified approach also allows for perturbation (modification) of a single census-tract, if so desired, or any arbitrary group of tracts for UHII mitigation modeling. Also, since the input is customized for each nest separately, as discussed in Section 2.5.1, it is possible to trigger the urban parameterizations in different manners in different nests to further optimize the simulations.

This approach is useful for Levels 3 and 4 UHII modeling as additional means to examine the effects of various surface perturbation scenarios. It can trigger the application of UCM in parallel to application of other urbanized modules or the modified approach of this study.

2.5.6. Test of modified approach versus selective UCM

Thus with respect to model modifications to improve representation of urban areas, two customizations were evaluated. These were:

A. The modified approach discussed in Sections 2.5.1 through 2.5.4, and
B. Selective trigger of UCM (discussed in Section 2.5.5)

In approach A, and in addition to the customizations discussed above, other parameters were used based on standard WRF lookup values, including soil moisture and emissivity.

Comparison of model results showed that the daytime predicted fields, e.g., skin-surface and 2-m air temperatures (of relevance to UHI/UHII) were very similar in approaches A and B, with a maximum deviation of ± 0.2°C in skin-surface temperature and much less in air temperature. However, the nighttime fields showed a cold bias in approach "B", with a maximum deviation of ~ -3°C in skin-surface temperature. Air temperature cold bias in approach B was ~0.5°C larger than in approach A. The bias was detected mostly in areas with NLCD and Level-II LULC but not in areas with the older, single category urban class. Thus the cold bias is also affected by how the urban model uses the new NLCD data. Because there was no added benefit from using approach "B", the modified approach "A" was used.

2.5.7 Interpolation procedure

In order to compute the UHI and derive the UHII at any number of points (e.g., census-tract centroids), post-processing of WRF output and interpolating the meteorological fields to the correct location (within a census tract) and elevation was required. For this purpose, the RIP4 interpolation and mapping program of Stoelinga (2009) was used. The application of RIP4 in this study was tailored to extract data at each census-tract centroid and output them in a manner that is conducive to computing the UHI and UHII based on time-varying upwind temperature reference points (which will be discussed in Sections 3.2 and 3.5).

The RIP4 interpolation scheme was applied to 1) compute upstream wind speed and direction around specified urban areas, 2) define upwind temperature reference based on computed wind approach direction in step 1, 3) compute the UHI at census-tract centroids relative to the temperature reference point defined in step 2, and 4) derive the UHII accordingly.

2.5.8. Configuration of modeling periods

As discussed in Section 2.3, the target modeling periods were JJA of 2013 and JJA of 2006. These modeling periods were broken down into 15-day intervals (plus 2 spin-up days for each) for re-initialization so as to minimize any possible drift in model performance. The modeled intervals, including the extra days for spin-up, are as in Table 11 (UTC time). Figure 15 depicts the marching of the simulation.

Table 11: Modeling periods (including spin-up days)

YEAR 2013			
Interval 1:	2013-05-30_00:00	through	2013-06-16_00:00
Interval 2:	2013-06-14_00:00	through	2013-07-01_00:00
Interval 3:	2013-06-29_00:00	through	2013-07-16_00:00
Interval 4:	2013-07-14_00:00	through	2013-08-01_00:00
Interval 5:	2013-07-30_00:00	through	2013-08-16_00:00
Interval 6:	2013-08-14_00:00	through	2013-08-31_00:00
YEAR 2006			
Interval 7:	2006-05-30_00:00	through	2006-06-16_00:00
Interval 8:	2006-06-14_00:00	through	2006-07-01_00:00
Interval 9:	2006-06-29_00:00	through	2006-07-16_00:00
Interval 10:	2006-07-14_00:00	through	2006-08-01_00:00 **
Interval 11:	2006-07-30_00:00	through	2006-08-16_00:00
Interval 12:	2006-08-14_00:00	through	2006-08-31_00:00

** Interval 10 corresponds to the California heat wave, July 15 through August 1st, 2006 (Trent 2007, Gershunov et al. 2009).

Figure 15: Simulation marching, re-initializations, and spin-up intervals.

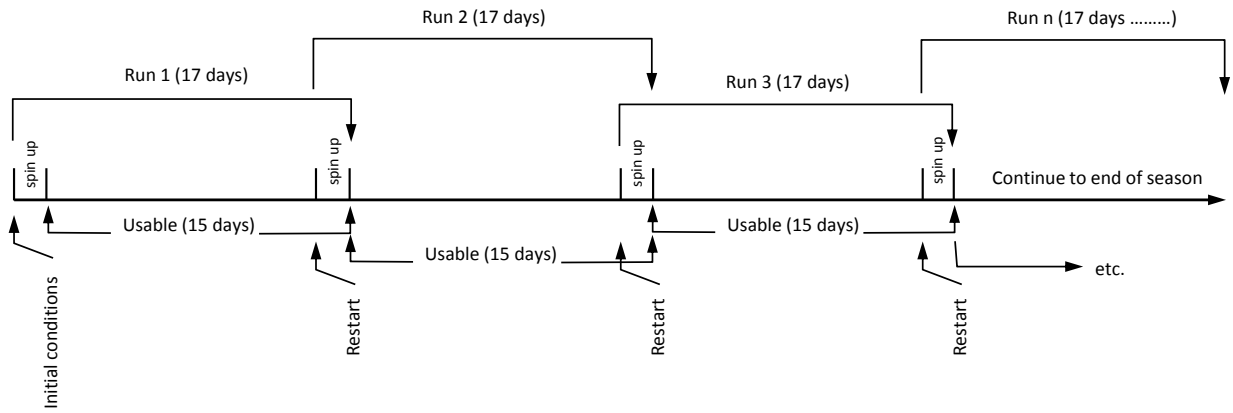

3. RESULTS

3.1. INITIAL MODEL TESTS

After the model updates and customizations discussed in Section 2.5 were implemented, an initial set of model runs was undertaken to test functionality and evaluate the first results. The initial runs showed that the modified approach allows the model to capture fine-scale features of interest. Figures 16a-16d show sample output from arbitrary 3-km and 1-km domains (D03 and D06). Note that what is shown in these figures is skin-surface temperature (not air temperature) for the purpose of initial model evaluation.

As seen in Figures 16a-16d, the modifications produce relevant detail at the 3- and 1-km levels. For example, the model produces well-defined urban heat islands as well as a detailed outlines of the major highways in each domain, particularly in the 1-km grids. Because of the bottom-up characterization of the surface at fine resolutions, e.g., 200 m (Figure 10), the simulations retain some of the fine features. It is interesting to compare these with a snapshot of night lights observed from space (Figure 17). Figure 18 shows an example of modeled air temperature (2 m AGL) in this domain, again displaying a distinct pattern of heat islands.

Figure 16. a: Nighttime skin-surface temperature in domain D03 at 2100 PDT on 3 June 2013, **b**: Daytime skin-surface temperature at 1400 PDT on 3 June 2013. Both figures depict higher urban temperatures than in non-urban areas. Sacramento is at top center of figure; Fresno is a bottom right. **c**: Nighttime skin-surface temperature in domain D06 (1km) at 2100 PDT on 3 June 2013, **d**: Daytime skin-surface temperature at 1400 PDT on 3 June 2013. Figures depict higher urban temperatures in the region from Stockton to Patterson and the high fidelity of the modified approach in capturing some fine temperature detail throughout the area, for example the temperature effects of highways 5, 33, 132, 580, 99, 108 (marked on figure) and many others. Compare with Figure 17 domain D06.

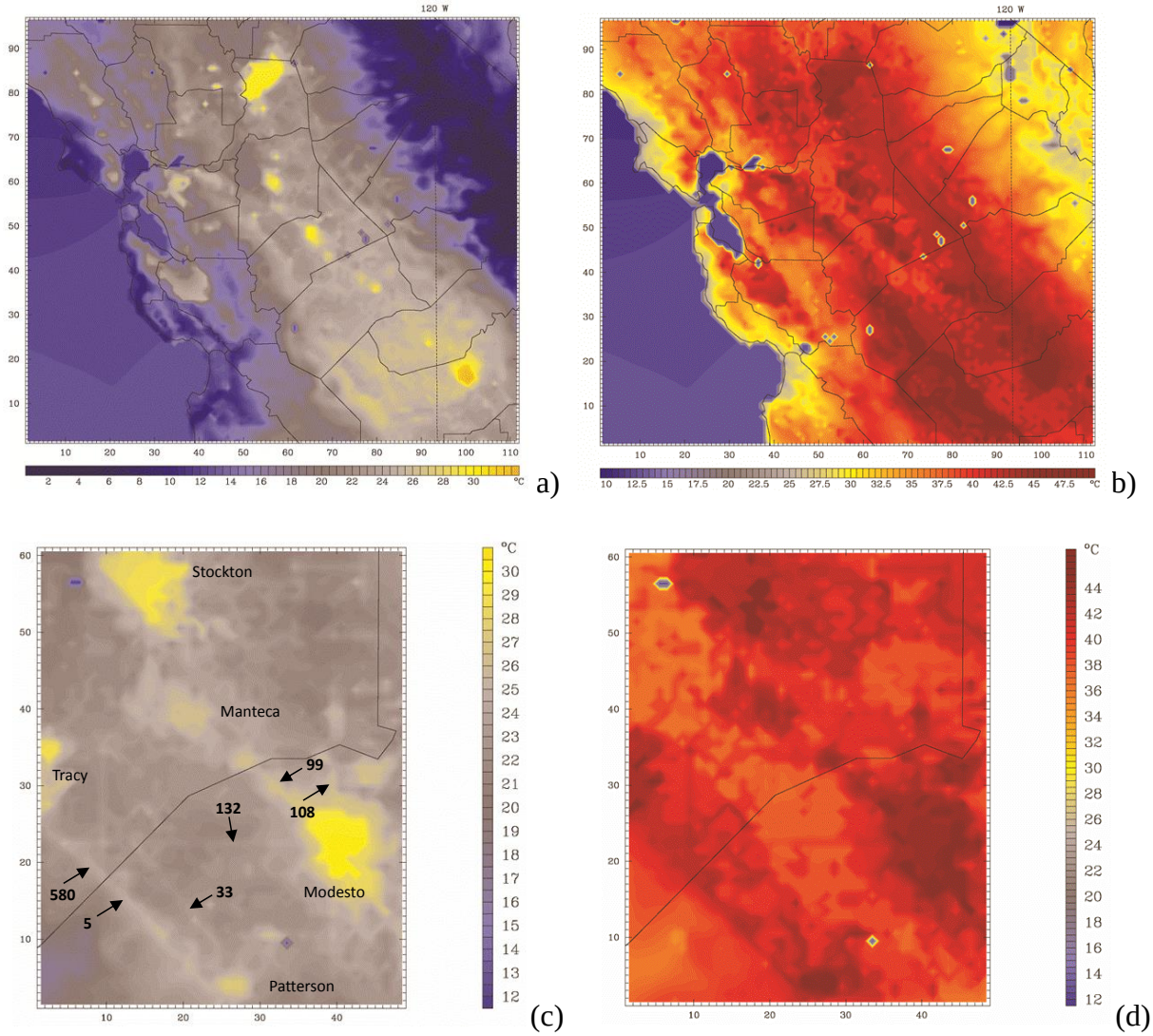

Figure 17: San Francisco – Sacramento – Stockton – Modesto night lights show the extent of urbanization in the region. Photograph credits: Keith Cowing, spaceref.com (2013) and NASA (International Space Station).

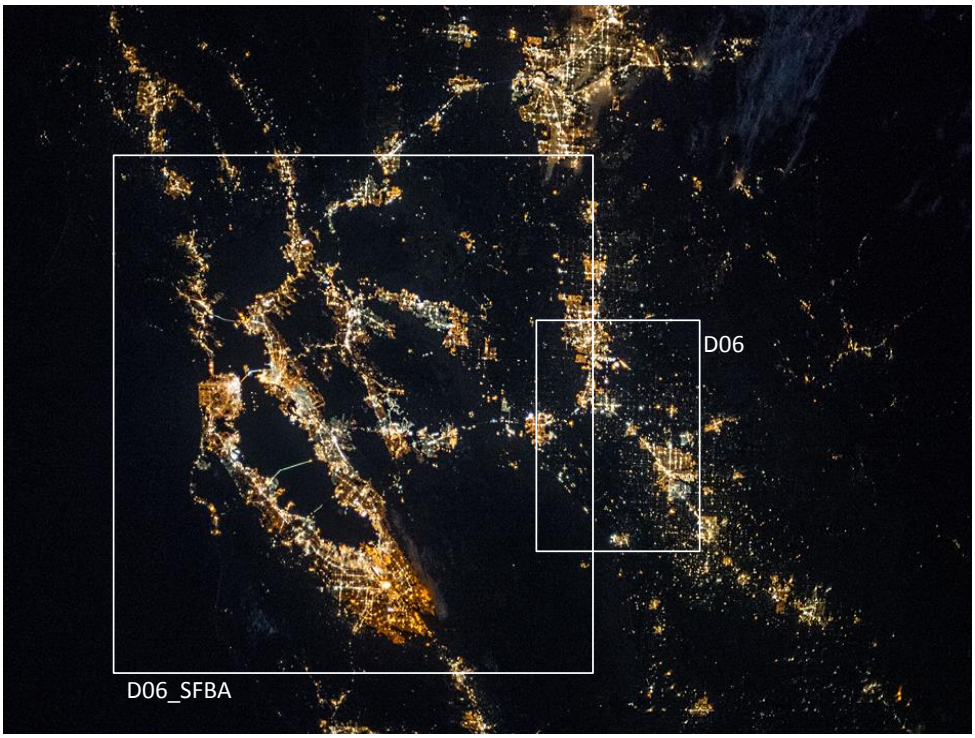

Figure 18: Daytime example for D03 showing air temperature (2 m AGL) at 1400 PDT on 7 June 2013. Notice the well-developed air-temperature UHIs over Sacramento to Elk Grove, Stockton, Modesto, Merced, and Fresno as well as the East and South Bay (in the San Francisco Bay Area).

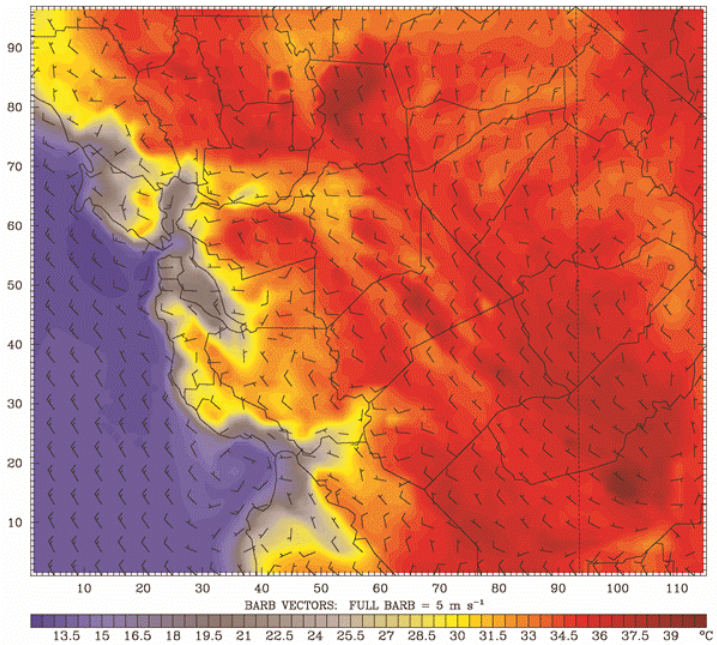

3.2 UHI/UHII REFERENCE POINTS

It is known from observations and numerical modeling studies that the UHI circulation interacts with the background, synoptic-scale flow (Boucouvala and Bornstein 2003, Kim and Baik 2005, Taha 2008a). This interaction, in turn, determines the local flow patterns. For an urban area, there is generally a wind speed threshold that determines the impact of background flow relative to that induced by the UHI. This wind-speed threshold has been shown to be a function of city size (population) as well as location-specific attributes. For example, Oke and Hannell (1970) and Oke (1973) proposed that the wind-speed threshold for UHI be characterized by:

$$U = -11.6 + 3.4\, log_{10}\, P \qquad (8)$$

where U is in m s^{-1} and P is population. In this UHII study, the threshold is diagnosed for each region based on model data.

Thus, the flow pattern must be accounted for in calculating the UHI. Unlike in simpler approaches, where the UHI is computed relative to a single fixed-in-space reference point, this modeling study computes the UHI based on time-varying, wind-dependent UHI reference points in each area. That is, the UHI is quantified dynamically based on varying wind direction, such that the reference points are upwind of the urban area.

For the purpose of deriving the UHII in this project, the calculations of the hourly (or sub-hourly) UHI / UCI proceed as follows:

I. When the background wind speed is larger than the threshold, the synoptic flow induces a pattern of consistent wind direction through an urban area. In this case, the UHI temperature reference points are those at the leading edge of the urban area (upwind).

II. When background wind speed is below the threshold, the UHI circulation dominates and thus determines the local flow pattern which tends to become convergent. In addition, when an area is under the influence of a high-pressure system or stagnant conditions, wind flow can become disorganized. Under these conditions, the UHI reference temperature is taken as the average of temperatures at all UHI reference points or the points closest to the UHI calculation location.

Dynamic selection of UHI reference points

Thus a simple post-processing code was written to evaluate wind-flow patterns in each region and at each hourly interval of the simulated periods. It diagnoses the UHI reference points from a set of pre-selected points (see “Pre-selected UHI reference points” below) based on wind direction and whether the flow is uniform or disorganized. It then computes the UHII based on the diagnosed reference points. Thus referring to Figure 19a (Fresno), for example, if the synoptic wind is dominant and northwesterly (i.e., northwesterly at points 1, 2, 3, and 4, then the UHI temperature reference point 2 is used. If the wind is consistent and southwesterly at all four points, then UHI reference point 1 is used, and so on. During conditions when UHI circulation dominates or the flow is disorganized, the reference temperature is the average of temperatures at points 1, 2, 3 and 4 or the average of temperatures at the reference points nearest to the UHII calculation point. Note that the number of upstream UHI reference points varies from one area to another depending on size and geographical / topographical properties.

Following these steps, the code then extracts from the meteorological output field the variables at the specific census-tract centroids developed in this study using the method discussed in Section 2.5.7.

Pre-selected UHI reference points

The calculation of UHI/UHII was carried out at each census-tract relative to UHI reference points dynamically allocated as discussed above. Prior to this dynamic selection, a number of reference points were established a priori. For each UHII tile, the static selection of UHI temperature reference points was made while considering the following general factors:

- The characteristic and dominant flow patterns in the area (e.g., based on wind climatology for each tile, see example wind roses in Figures 19a and 19b);
- Availability of consistent and relatively large contiguous areas (i.e., relative to the size of the urban area) of non-urban land-uses that are representative of natural / non-urban cover in the region of interest and that can serve as a source of UHI reference points;
- Similar elevations relative to those of census tracts where UHII calculations are desired;
- As close as possible to leading edges of urban areas, yet remote enough to not be affected by urban heat plumes (downwind) when flow is reversed; and
- In areas with lower skin-surface temperature than urban areas as predicted by the meteorological model. This helps identify contiguous non-urban areas that can be used to site the UHI reference points.

As will be discussed further in Section 3.5, one criterion in selecting UHII-calculation areas (tiles) and UHI reference points is to minimize the effects of natural, background variations in climate. Large metropolitan areas or clusters of urban areas can cover vast expanses over which the background climate varies, for example from coast to inland and north to south. In such cases, the UHII calculation tiles were selected to break the urban areas into smaller regions to minimize the signal from background climate variations in the UHII. In addition, different UHI reference points were assigned to different parts of large urban regions so as to capture the UHI signal as correctly as possible and minimize the background climate signal.

3.3 INITIAL MODEL OUTPUT EXAMPLES

As part of the initial model tests, as well as early evaluations of the post-processing system and computation of the UHII, two arbitrary output examples were provided to CalEPA for review (Sacramento and Fresno). In this section, these examples are discussed briefly. Figures 19a and 19b depict the locations of non-urban, upstream UHI reference points for each of the Fresno and Sacramento regions, respectively, selected for providing this sample output.

Table 12 provides additional information on these reference points. The Grid X and Grid Y coordinates (in grid point units) are relative to the origin of each respective grid, that is, domains D07 or D03, respectively (see Figure 4).

Table 12: UHI reference points attributes

Fresno area (Figure 19a):

ID	Location	Grid X	Grid Y	Latitude	Longitude
1	SW	15.0	8.5	36.68	-119.86
2	NW	10.5	28.0	36.86	-119.91
3	NE	33.5	24.0	36.82	-119.64
4	SE	32.0	11.0	36.70	-119.66

Sacramento area (Figure 19b):

ID	Location	Grid X	Grid Y	Latitude	Longitude
A	SW	46.0	77.00	38.43	-121.67
B	NW	48.0	86.00	38.68	-121.60
C	NE	61.1	83.46	38.62	-121.14
D	SE	57.5	80.20	38.53	-121.26

Figure 19a: UHI/UHII reference points for the Fresno region. Not to scale. (Map background credit: Google Earth. Wind-rose credit: NOAA/NCDC)

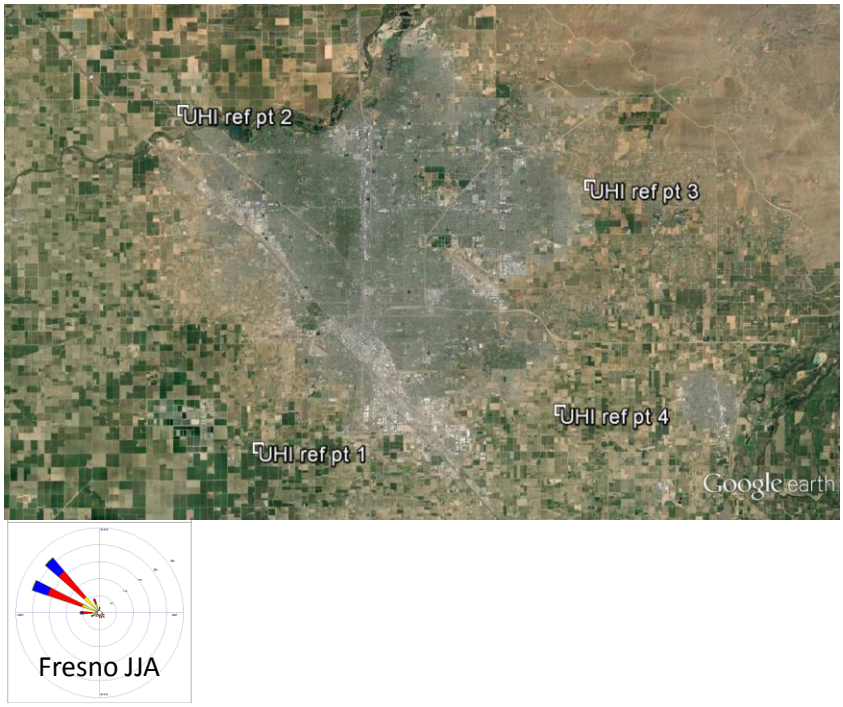

Figure 19b: UHI/UHII reference points for the Sacramento region. Not to scale. (Map background credit: Google Earth. Wind-rose credit: NOAA/NCDC)

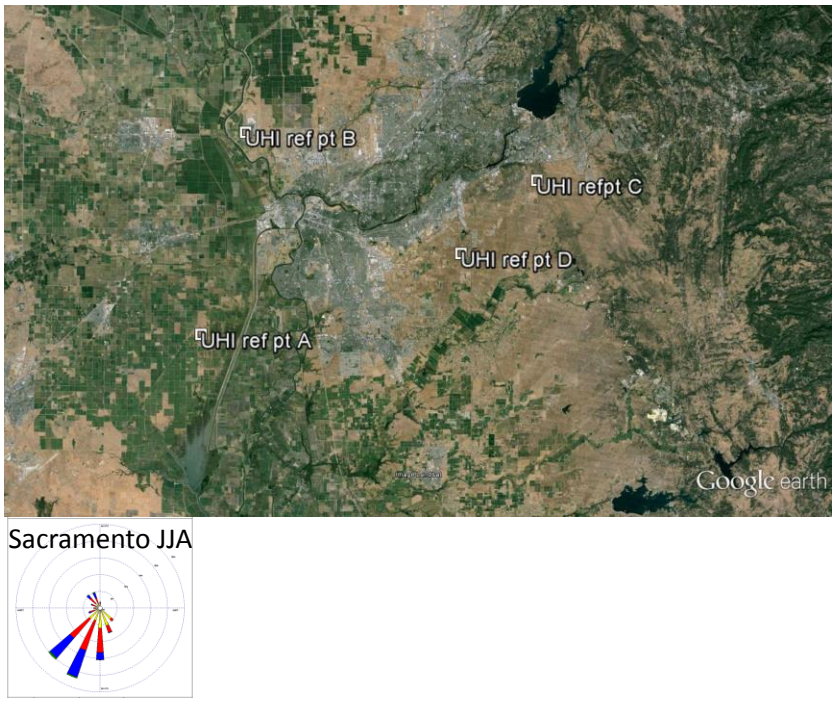

For the initial UHII test calculations (e.g., shown in Figures 20 and 21), the following assumptions were made:

I. A population-density threshold of 1000 km^{-2} was used as a filter to reduce the number of census tracts plotted in these examples (a threshold of 50 km^{-2} was used in the final UHII calculations presented later in Section 3.5);

II. The sample UHII was computed only for the first 15 days of JJA 2013 (UHIIs from other periods are different and the total UHII is much larger over the entire JJA periods, as will be discussed in Section 3.5);

III. The UHII values were computed relative to each region's UHI reference points and were not related to any absolute temperature thresholds. In other words, the UHII values in the two sample regions (Sacramento and Fresno) can be compared in terms of relative UHII magnitudes but cannot be compared directly against each other in terms of absolute temperature.

In this initial test, two slight variations of Equation 3 (Figure 1) were evaluated: with and without the "min" operator in the equation. In the latter, all temperature differences $T_u - T_{nu}$ (positive and negative) were included in the UHII. At each census tract, there can be hours with negative (UCI) as well as hours with positive (UHI) temperature differences, although the overwhelming majority is positive. Regardless, when totalized, the UHII is overwhelmingly positive, but a small number of census tracts can have a negative total UHII. In the Sacramento example, there

are only 4 census tracts in the west and southwest areas (out of 293 tracts shown in Figure 20) that have small negative values. In the Fresno domain, no negative UHII values were found. However, once the UHII definition is applied by including the "min" operator in Equation 3, all negative UHI values vanish both at the hourly level and at the total UHII level. Figures 20 and 21 show the results of applying Equation 3 with the "min" operator, which is the basis for all subsequent calculations and maps in this report.

The maps in Figures 20 and 21 show that the largest UHII are generally in high-intensity urban areas and downwind of the urban core. For example, in Sacramento, the largest UHIIs are found in the northeast part of the urban region (as the dominant wind direction is southwesterly). In Fresno, the largest UHIIs are found to the south and southeast of the urban center (as the dominant flow is from the northwest).

Figure 20: UHII (**DH/15 days**) computed for census tracts in the Sacramento region. Sample period is June 1st through 15th, 2013.

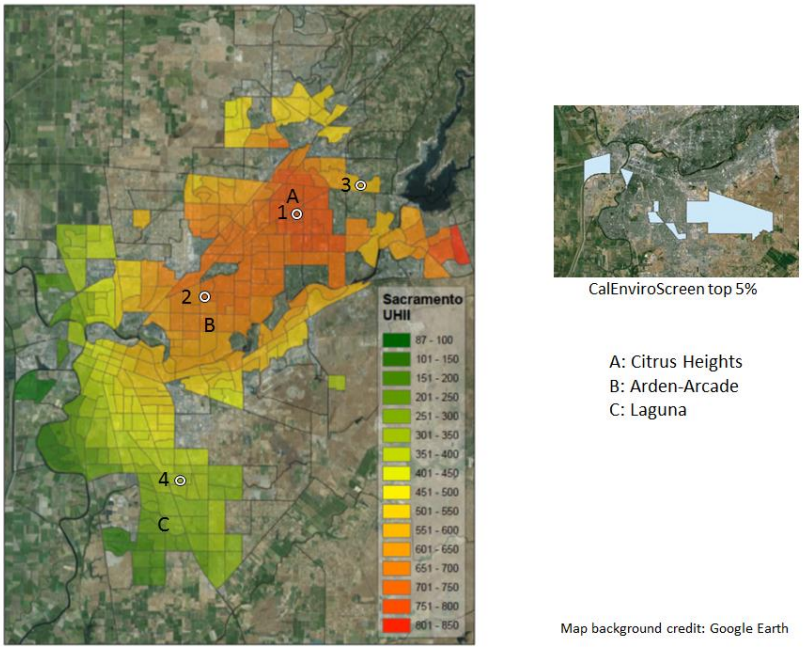

Figure 21: UHII (**DH/15 days**) computed for census tracts in the Fresno region. Sample period is June 1st through 15th, 2013.

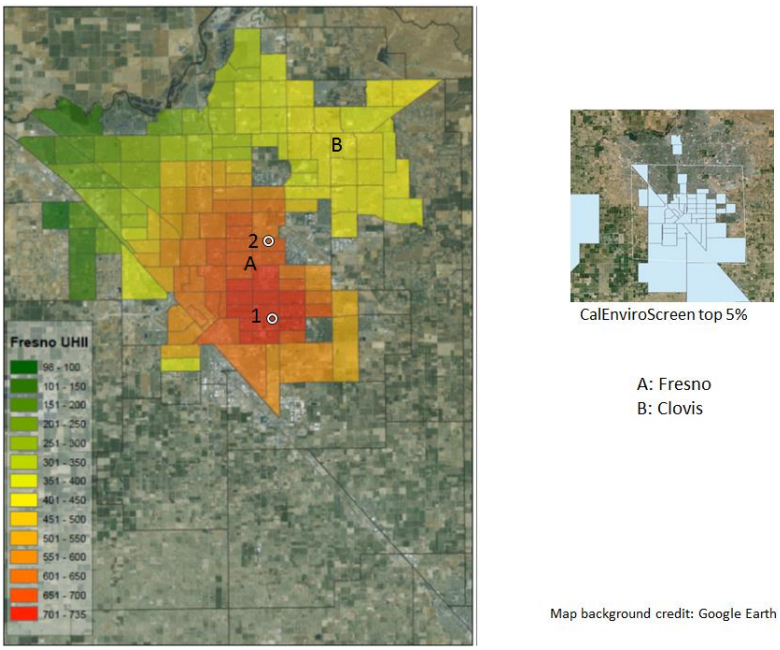

Figure 22 (a-e) depicts time series of the UHI at every hour during the sample period 1–15 June 2013, for arbitrary locations indicated with white circles in Figures 20 and 21. The data shows the temperature-difference spread at each hour of the day (across all 15 days). Figure 22a for Fresno shows the UHI resulting from applying Equation 3 without the "min" operator. Thus one can see a small cool island (UCI) of about 0.2 to 0.4°C between the hours of 0730 and 1000 PDT. On the other hand, Figure 22b results from applying Equation 3 with the "min" operator, thus showing the same data without the UCI. Figures 22c,d,e show the UHI in three locations in the Sacramento region (with the "min" operator). In Figures 22b – 22e, the UHI reaches up to about 4-7°C at night and up to about 2-8°C during the day. Predominantly, the mid-day UHI reaches up to about 2°C in the arbitrary example locations discussed here. These locations also show the classical definition of the UHI with the rapid cooling of non-urban areas beginning at about 1900 PDT (thus higher urban temperatures at night).

However, there is a large variability in the UHI profile across the various regions in California and the large number of census tracts within each. Some regions have larger daytime UHIs, other have equal daytime and nighttime UHIs. Some have larger UHIs during the afternoon (such as the Sacramento examples in Figures 22c and 22d). Thus the purpose of Figure 22 is to illustrate some examples and it should be noted that other locations have different diurnal profiles and magnitudes of UHI than shown here. Furthermore, the sample results provided here are only for June 1-15, 2013. Other periods have different UHI/UHII profiles and magnitudes as well.

Figure 22a: UHI/UCI (C°) at Fresno point 1 (see Figure 21) including all positive and negative temperature differences.

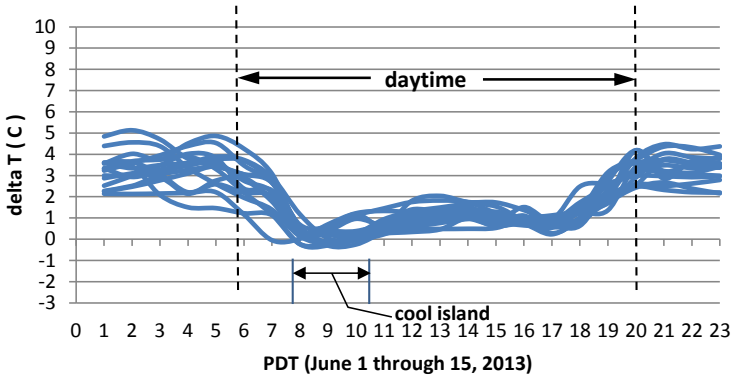

Figure 22b: UHI (C°) at Fresno point 1 (see Figure 21) including only positive temperature differences.

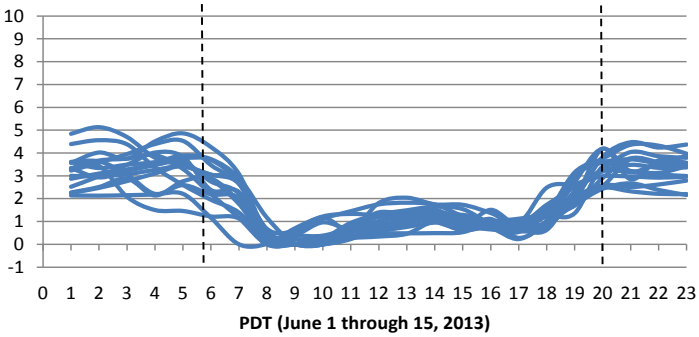

Figure 22c: UHI (C°) at Sacramento point 2 (see Figure 20) including only positive temperature differences.

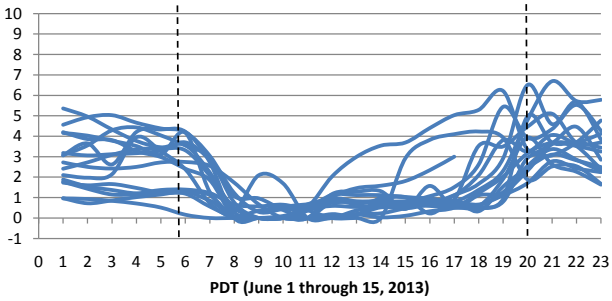

Figure 22d: UHI (C°) at Sacramento point 3 (see Figure 20) including only positive temperature differences.

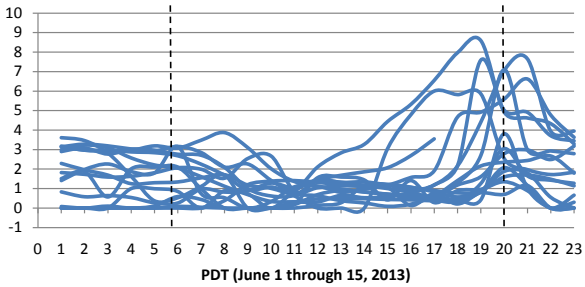

Figure 22e: UHI (C°) at Sacramento point 4 (see Figure 20) including only positive temperature differences.

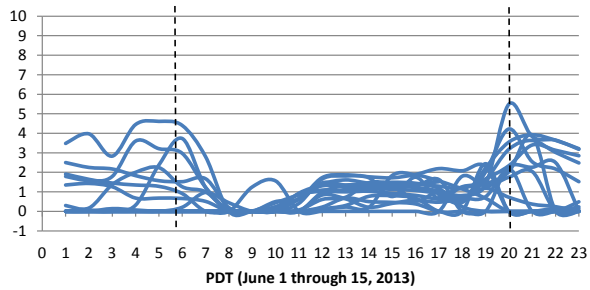

3.4 MODEL PERFORMANCE EVALUATION

In order to carry out thorough model performance evaluation (MPE), periods and geographical domains were defined where observational and modeled meteorological fields were subsequently compared. In this effort, the MPE periods are JJA 2013 and JJA 2006 and the MPE geographical domain corresponds to D02, shown with a red line in Figure 23, and its sub-domains. Domain D02 encompasses the entire states of California and Nevada as well as the western halves of Utah and Arizona. However, the observational data are heavily concentrated in California. All sub-domains of D02, i.e., domains D03 through D10, were also evaluated separately and in combination in this MPE. Figure 23 also depicts the locations of observational monitors (white arrows) that were "windowed" from the NCAR ds472 observational dataset to correspond to domain D02. The number of monitors in D02 through D10 is given in Table 13. Because domains D06 through D10 are small, there are a correspondingly smaller number of ds472 monitors within their boundaries.

Figure 23: Model performance evaluation domain. Map background source: Google Earth.

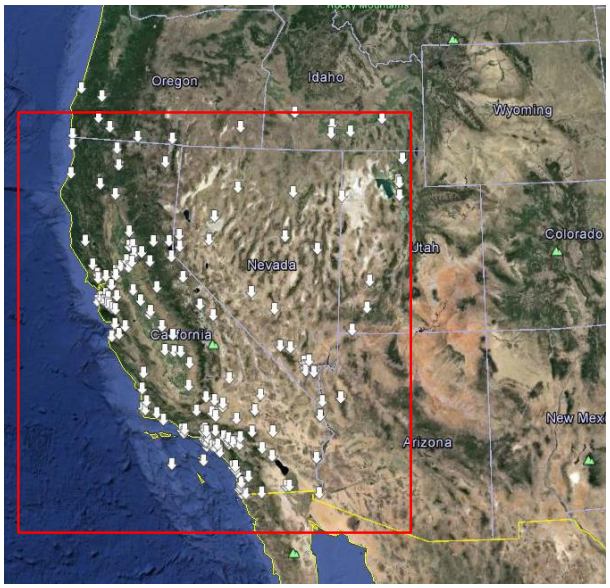

Table 13: Number of observational monitors in model domains.
(Most relevant domains are shaded).

Domain	Number of ds472 monitors
D02	151
D03	40
D04	6
D05	42
D06	2
D07	1
D08	1
D09	4
D10	3

There are a number of possible different combinations of physics and dynamics configurations available in the WRF model. Several such combinations are usually evaluated at the start of any modeling study and, as such, were also evaluated at the beginning of this application. Some model options were selected earlier on partly based upon experience with past modeling studies of UHI (e.g., Taha 2005, 2007, 2008a-c,2013a,b). Following establishment of the initial configurations of models based on those optimal options, two influential physics configurations remained to be tested. These were: 1) the planetary boundary-layer physics scheme and 2) the urban physics parameterizations. Thus, three approaches were tested in light of MPE: 1) MYJ versus BouLac PBL schemes (Janjic 2002, Bougeault and Lacarrere 1989), 2) modified approach versus modified+UCM model (Kusaka et al. 2001, Chen et al. 2010), and 3) MYJ and modified approach without urban modules.

In the initial model performance evaluation, the following was carried out:

- Compared the performances of the Mellor-Yamada-Janjic ETA (Janjic 2002) "MYJ" and Bougeault and Lacarrere (1989) "BouLac" boundary-layer parameterization schemes for the purpose of this application. Both MYJ and BouLac are TKE, 2.5/1.5 order, local-closure schemes that account for counter-gradient transport with a counter-gradient term in the vertical diffusion equation (BouLac) and in the thermal variance equation (MYJ). While other PBL schemes are available in WRF, MYJ and BouLac are the parameterizations currently linked to and often used with 1) the NOAH land-surface model (which is where surface modifications and model customizations were performed as discussed in Section 2.5.1) and 2) the UCM urban module, as discussed earlier.

  The initial analysis of model performance in this case indicated that whereas wind speed, direction, and humidity statistics were similar between the two schemes, temperature statistics using the MYJ scheme were better in this application (0.5-0.75°C better than BouLac in attaining the gross error benchmarks).

- Compared the modified approach against the combined modified + UCM approach. The Urban Canopy Model (UCM) is described in Kusaka et al. (2001) and Chen et al. (2010), whereas the study modifications were described earlier. The initial performance analysis

suggested that the modified approach alone (with NOAH LSM) performs better than with the UCM as the latter produced some negative temperature bias at night in this application, as discussed in Section 2.5.6.

- Compared the MPE of the final selected options (modified approach, NOAH LSM, no UCM, and all prior configurations discussed above) against MPE from prior UHI studies, as well as against community-suggested benchmarks (listed below). With respect to prior similar studies (e.g., Taha 2005, Taha et al. 2011), model performance in this application was found to be similar or better. Relative to benchmarks, the discussion below suggests that model performance is acceptable with the selected configurations and customizations in this study.

The remainder of this section presents the MPE statistics for the final model configurations, including the modifications and customizations discussed earlier in Section 2.5. This MPE is based on evaluation of several metrics including mean bias (B), gross error (E), root mean square error (RMSE), index of agreement (IOA), and related variables over regions in the modeling domains. The metrics so computed are then evaluated against benchmarks suggested by the modeling community (e.g., Tesche et al. 2001). In this MPE, wind speed, wind direction, temperature, and humidity were evaluated. Other meteorological variables including precipitation, for example, were not examined as they were not applicable to the modeled periods. Following Tesche et al. (2001), the MPE metrics and their ranges are listed below, where P is a predicted (model) variable, O is corresponding observation, and I and J are the space and time indices:

1. *Bias* (B) is the mean difference in prediction-observation pairs over a given analysis region and for a given time period.

$$B = \frac{1}{IJ} \sum_{j=1}^{J} \sum_{i=1}^{I} \left(P_j^i - O_j^i\right) \qquad (9)$$

2. *Gross error* (E) is the mean of the absolute difference in prediction-observation pairs for each region and analysis period of interest.

$$E = \frac{1}{IJ} \sum_{j=1}^{J} \sum_{i=1}^{I} \left|P_j^i - O_j^i\right| \qquad (10)$$

3. *Root mean square error* is the square root of the mean squared difference in prediction-observation pairs.

$$RMSE = \left[\frac{1}{IJ} \sum_{j=1}^{J} \sum_{i=1}^{I} \left(P_j^i - O_j^i\right)^2\right]^{1/2} \qquad (11)$$

4. *Systematic Root Mean Square Error* (RMSEs) is the square root of the mean squared difference in regressed prediction-observation pairs where the regressed prediction (*rP*) is estimated from a least square regression of *P* against observation *O*. The RMSEs estimates the model's linear (or systematic) error and, thus, the better the regression between predictions and observations, the smaller the systematic error.

$$RMSEs = \left[\frac{1}{IJ} \sum_{j=1}^{J}\sum_{i=1}^{I}\left(rP_j^i - O_j^i\right)^2\right]^{\frac{1}{2}} \qquad (12)$$

5. *Unsystematic Root Mean Square Error* (RMSEu) is the square root of the mean squared difference in prediction and regressed-prediction pairs where, again, *rP* is estimated from a least-square fit. The unsystematic difference is a measure of how much of the discrepancy between estimates and observations is due to random processes outside the legitimate range of the model.

$$RMSEu = \left[\frac{1}{IJ} \sum_{j=1}^{J}\sum_{i=1}^{I}\left(P_j^i - rP_j^i\right)^2\right]^{1/2} \qquad (13)$$

Thus a good model performance exhibits a small RMSE, a small RMSEs that is tending closer to zero, and a RMSEu that is tending towards RMSE values. Note that

$$(RMSE)^2 = (RMSEs)^2 + (RMSEu)^2 \qquad (14)$$

6. *Index of agreement* is the ratio of the total RMSE to the sum of two differences – between each prediction (*P*) and the observed mean (M_o), and each observation (*O*) and the observed mean (M_o). Index of Agreement (IOA) thus is a compact indicator of performance and a good measure of the match between the departure of each prediction from the observed mean (M_o) and the departure of each observation from the observed mean (M_o). Accordingly, an IOA value of 1 suggests a perfect agreement between predictions and observations.

$$IOA = 1 - \left[\frac{IJ\,.\,RMSE^2}{\sum_{j=1}^{J}\sum_{i=1}^{I}\left|P_j^i - M_o\right| + \left|O_j^i - M_o\right|}\right] \qquad (15)$$

Table 14 lists the modeling-community-suggested benchmarks for comparison of metrics. As Tesche et al. (2001) point out, these benchmark values are not meant as “pass/fail” criteria for a certain modeling application but, rather, to provide a common basis for comparing model performance.

Table 14: Community-suggested model performance benchmarks

Variable	Bias (*B*)	Gross error (*E*)	*RMSE*	*IOA*
Wind speed	$\leq \pm 0.5$ m s^{-1}		≤ 2.0 m s^{-1}	≥ 0.6
Wind direction	$\leq \pm 10^{o}$	$\leq 30^{o}$		
Temperature	$\leq \pm 0.5$ K	≤ 2 K		≥ 0.8
Humidity	$\leq \pm 1$ g kg^{-1}	≤ 2 g kg^{-1}		≥ 0.6

For those variables where both bias and error benchmarks exist, it may be more useful to use the error metric since it brackets the range (bounds) of performance rather than simply pointing to direction of bias. Regardless, all metrics are presented in the following discussion. The results from MPE were provided to the CalEPA for review and approval, including daily and hourly statistics and time series for the modeled periods. In the discussion below, the performance summaries for near-surface fields are provided along with an example of the daily and hourly statistics (these are not included here because of length). Furthermore, the summaries are often the most useful indicators to a model's performance overall.

Thus in a compact manner, Table 15 represents results from this MPE. The dark-green color in the tables represents those instances where model performance in this study exceeds the suggested benchmark values in Table 14, that is, model performance is better than the benchmarks. The light-green color represents those instances where model performance is close to the suggested benchmarks and is acceptable. The white color indicates instances where model performance deviates from the benchmark value, albeit still reasonable in most cases. Again, it is reiterated that these are not pass/fail criteria but, rather, a common basis for comparison.

Table 15a shows the metrics averaged over the 3-km domains for JJA 2013 and JJA 2016 combined. In this case, the light green values are 25% over attainment for wind-direction gross error (37.39° versus 30°), 50% over attainment for temperature bias (0.78°C versus 0.5°C), and 28% over attainment for temperature gross error (2.56°C versus 2°C). These values are very reasonable in absolute terms, as further indicated by the IOA which is significantly greater than 0.8, the IOA benchmark for temperature. The results in Table 15a indicate that model performance is acceptable.

Of note, Table 15a is likely the most relevant "take away" summary since the calculation of UHII is based on output from these domains. And whereas Table 15b (discussed next) provides an assessment of model performance over the entire D02 domain (all of California and neighboring states), it is not directly relevant to the derivation of UHI and UHII in California.

Thus Table 15b summarizes model performance for D02 for JJA 2013, JJA 2006 separately and combined (All). The table shows that while wind direction gross error (~47°) deviates from the suggested 30° benchmark, the 17° deviation is small by comparison to several other modeling studies of California (where error reached 60-70°) and is deemed acceptable for this application. It should be noted that 1) most of the deviations in wind direction occur during periods of low wind speed, e.g., at night or during stagnation events when wind-direction sensors (vanes) can practically point in any direction and it becomes relatively more difficult for a model to reproduce the observations, and 2) one reason why wind direction metrics can appear poorer than they actually are is that near north, very large and very small wind direction values are in reality

very close. For example, a modeled wind at 357° (very large number) is very close to observed wind at 1° (very small number). Such instances can affect MPE but are not of real concern. This will be seen again in the sample daily and hourly statistics provided further below. Furthermore, these deviations in wind direction (in Table 15b) occur mostly outside of California, and thus have no bearing on the results and calculations of the UHII.

Tables 15c through 15f provide additional breakdown details to the summaries in Tables 15a and 15b. Table 15c provides further breakdown by domains D02 through D10. For each domain, the statistics in are combined (for 2013 and 2006). Table 15d further expands Table 15c by showing JJA 2013 and JJA 2006 separately as well as combined for the 3-km domains (D03, D04, and D05). Finally, Tables 15e and 15f expand Table 15c further, by providing the corresponding metrics for the 1-km domains (D06 through D10).

Examination of the metrics in Table 15 shows that model performance predominantly exceeds the benchmarks (good model performance) and that in instances where the benchmarks are not fully met, performance is still reasonable.

Table 15a: Combined performance metrics (for 3-km domains) and JJA 2013/2006

Wind Spd	Bias	(m/s)	0.08
Wind Spd	RMSE	(m/s)	1.73
Wind Spd	Sys RMSE	(m/s)	0.71
Wind Spd	Unsys RMSE	(m/s)	1.56
Wind Spd	IOA		0.78
Wind Dir	Bias	(deg)	0.92
Wind Dir	Gross Error	(deg)	37.39
Temprtr	Bias	(K)	0.78
Temprtr	Gross Error	(K)	2.56
Temprtr	IOA		0.93
Humdity	Bias	(g/kg)	-0.89
Humdity	Gross Error	(g/kg)	1.47
Humdity	IOA		0.65

Table 15b: Performance metrics for domain D02 (9 km)

D02			JJA 2013	JJA 2006	All
Wind Spd	Bias	(m/s)	0.21	0.08	0.14
Wind Spd	RMSE	(m/s)	2.15	2.13	2.14
Wind Spd	Sys RMSI	(m/s)	1.00	0.93	0.97
Wind Spd	Unsys RM	(m/s)	1.90	1.91	1.90
Wind Spd	IOA		0.70	0.68	0.69
Wind Dir	Bias	(deg)	0.00	0.73	0.36
Wind Dir	Gross Erro	(deg)	46.55	48.57	47.56
Temprtr	Bias	(K)	-0.95	-0.63	-0.79
Temprtr	Gross Err	(K)	2.74	2.80	2.77
Temprtr	IOA		0.94	0.94	0.94
Humdity	Bias	(g/kg)	-0.45	-0.96	-0.70
Humdity	Gross Erro	(g/kg)	1.47	1.78	1.62
Humdity	IOA		0.78	0.74	0.76

Table 15c: Combined performance metrics for domains D02 through D10

		Domain average over JJA 2013 and 2016								
		D02	D03	D04	D05	D06	D07	D08	D09	D10
Wind Spd	Bias (m/s)	0.14	0.04	-0.12	0.31	0.41	-0.27	-0.35	0.20	0.68
Wind Spd	RMSE (m/s)	2.14	1.81	1.59	1.80	1.60	1.43	1.46	1.26	1.66
Wind Spd	IOA	0.69	0.76	0.78	0.79	0.66	0.68	0.69	0.74	0.80
Wind Dir	Bias (deg)	0.36	0.25	-0.72	3.24	0.83	10.04	11.91	0.26	-0.38
Wind Dir	Gross Erro (deg)	47.56	36.28	37.30	38.59	27.48	41.90	39.58	37.51	30.51
Temprtr	Bias (K)	-0.79	1.16	1.47	-0.30	1.58	0.65	0.31	0.38	1.53
Temprtr	Gross Err (K)	2.77	2.54	2.73	2.40	2.21	1.96	1.79	1.80	2.39
Temprtr	IOA	0.94	0.94	0.94	0.91	0.95	0.96	0.95	0.88	0.91
Humdity	Bias (g/kg)	-0.70	-0.62	-0.66	-1.41	-1.09	-1.59	-1.00	-1.36	-1.96
Humdity	Gross Erro (g/kg)	1.62	1.24	1.28	1.90	1.45	1.93	1.58	1.57	2.23
Humdity	IOA	0.76	0.63	0.62	0.70	0.45	0.46	0.42	0.35	0.38

Table 15d: Separate 3-km domains performance metrics

		D03			D04			D05		
		JJA 2013	JJA 2006	All	JJA 2013	JJA 2006	All	JJA 2013	JJA 2006	All
Wind Spd	Bias	0.12	-0.04	0.04	-0.13	-0.11	-0.12	0.40	0.22	0.31
Wind Spd	RMSE	1.83	1.78	1.81	1.61	1.56	1.59	1.83	1.77	1.80
Wind Spd	Sys RMSE	0.80	0.72	0.76	0.81	0.70	0.75	0.68	0.57	0.62
Wind Spd	Unsys RMSE	1.63	1.62	1.62	1.37	1.38	1.37	1.69	1.67	1.68
Wind Spd	IOA	0.76	0.76	0.76	0.79	0.77	0.78	0.78	0.79	0.79
Wind Dir	Bias	1.12	-0.62	0.25	-0.71	-0.73	-0.72	4.18	2.30	3.24
Wind Dir	Gross Error	36.94	35.63	36.28	35.77	38.83	37.30	37.74	39.43	38.59
Temprtr	Bias	0.85	1.46	1.16	0.72	2.23	1.47	-0.33	-0.27	-0.30
Temprtr	Gross Error	2.49	2.58	2.54	2.39	3.06	2.73	2.32	2.48	2.40
Temprtr	IOA	0.94	0.94	0.94	0.95	0.93	0.94	0.92	0.90	0.91
Humdity	Bias	-0.54	-0.69	-0.62	-0.30	-1.01	-0.66	-1.03	-1.79	-1.41
Humdity	Gross Error	1.16	1.31	1.24	1.04	1.53	1.28	1.59	2.22	1.90
Humdity	IOA	0.69	0.57	0.63	0.70	0.54	0.62	0.74	0.65	0.70

Table 15e: Separate 1-km domains performance metrics (D06, D07, D08)

		D06			D07			D08		
		JJA 2013	JJA 2006	All	JJA 2013	JJA 2006	All	JJA 2013	JJA 2006	All
Wind Spd	Bias	0.61	0.21	0.41	-0.35	-0.18	-0.27	-0.18	-0.52	-0.35
Wind Spd	RMSE	1.63	1.57	1.60	1.41	1.45	1.43	1.48	1.45	1.46
Wind Spd	IOA	0.66	0.66	0.66	0.68	0.68	0.68	0.67	0.71	0.69
Wind Dir	Bias	-1.69	3.36	0.83	12.42	7.67	10.04	8.75	15.07	11.91
Wind Dir	Gross Error	26.61	28.36	27.48	40.44	43.36	41.90	39.86	39.31	39.58
Temprtr	Bias	1.70	1.45	1.58	0.00	1.30	0.65	-0.35	0.96	0.31
Temprtr	Gross Error	2.32	2.10	2.21	1.89	2.03	1.96	1.75	1.84	1.79
Temprtr	IOA	0.94	0.96	0.95	0.96	0.96	0.96	0.95	0.95	0.95
Humdity	Bias	-0.99	-1.18	-1.09	-1.38	-1.80	-1.59	-0.40	-1.60	-1.00
Humdity	Gross Error	1.32	1.58	1.45	1.70	2.16	1.93	1.18	1.98	1.58
Humdity	IOA	0.46	0.44	0.45	0.47	0.45	0.46	0.45	0.39	0.42

Table 15f: Separate 1-km domains performance metrics (D09, D10)

		D09			D10		
		JJA 2013	JJA 2006	All	JJA 2013	JJA 2006	All
Wind Spd	Bias	0.47	-0.07	0.20	0.76	0.60	0.68
Wind Spd	RMSE	1.30	1.22	1.26	1.67	1.66	1.66
Wind Spd	IOA	0.72	0.76	0.74	0.80	0.80	0.80
Wind Dir	Bias	0.99	-0.47	0.26	-0.57	-0.19	-0.38
Wind Dir	Gross Error	38.38	36.64	37.51	31.24	29.78	30.51
Temprtr	Bias	0.66	0.10	0.38	1.51	1.55	1.53
Temprtr	Gross Error	1.81	1.78	1.80	2.34	2.44	2.39
Temprtr	IOA	0.89	0.86	0.88	0.92	0.91	0.91
Humdity	Bias	-1.24	-1.49	-1.36	-1.46	-2.46	-1.96
Humdity	Gross Error	1.37	1.76	1.57	1.87	2.60	2.23
Humdity	IOA	0.34	0.35	0.35	0.44	0.31	0.38

In addition to the statistical MPE of near-surface meteorology summarized in Table 15, a qualitative evaluation of upper-air model performance was also undertaken. This evaluation exercise, not included in this report (large number of maps), involved examining upper-air meteorological fields produced by the model against observational synoptic upper-air maps at 0000Z and 1200Z for each day of the modeled periods. These maps were obtained from NWS, NOAA, and Unysis, as described in Section 2.4. The goal was to evaluate the model's ability in reproducing observed synoptic-scale features such as highs, lows, and their migration, as well as large-scale features in terms of pressure, flow patterns, temperature, humidity, and other meteorological fields.

An example of upper-air observational and model-produced maps is shown in Figure 24. In this qualitative component of MPE, several levels were evaluated (including 850, 700, and 500 hPa, among others) with focus on 850 hPa. The reason is that the 850-hPa altitude is sufficiently removed from the surface (generally outside of the boundary layer) so as to not be too influenced by detailed surface features yet low enough to capture regional and local effects and features, which is relevant to local model performance evaluations.

The upper-air variables considered in this MPE included 1) pressure heights, 2) temperature, 3) humidity, 4) wind vector field, and 5) locations of pressure systems and fronts. The qualitative evaluations indicated that the model captured the spatial patterns of the pressure heights reasonably well, as well as the general patterns of flow and temperature fields within the modeling domains across the state. The model also captured regional meteorological tendencies and fluctuations, including the 2006 heat wave (July 15-August 1st, 2006). The model also correctly reproduced geopotential heights (within a few meters) at several levels, e.g., 850 and 700 hPa.

Figure 24: 850 mb maps (for 00Z) on arbitrary days July 7 and August 23, 2013). Top maps (credits: NOAA) are the observational fields at 850 mb whereas the bottom figures are model-produced fields corresponding the same pressure level and times.

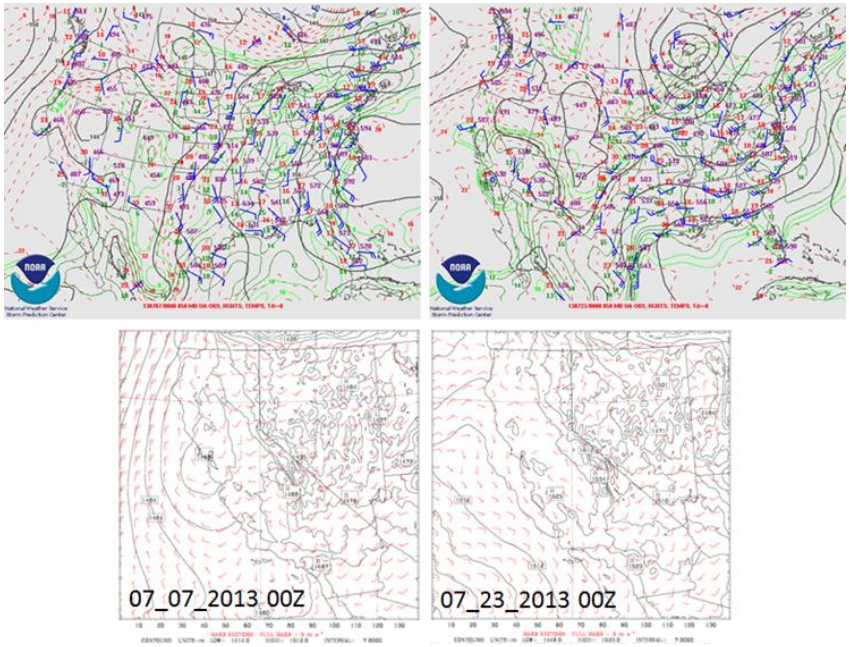

Figure 25 depicts another example of model statistics that were provided to CalEPA for review during the course of the project (but are not included in this report due to size). These hourly statistics of near-surface meteorology form the basis for the daily and overall summary statistics presented earlier in Tables 15a–15f. The statistics in Figure 25 provide information on the model's ability to reproduce the observed hourly fields of temperature, humidity, wind speed, and wind direction.

As seen in this example, in the top graph of Figure 25a, the model captures very well the hourly fluctuations in wind speed, ranges, magnitudes, and tendencies from day to day. This is also reflected in the other metrics, e.g., bias and RMSE. The relatively high IOA values (> 0.6) indicate a good fit. The two bottom graphs in Figure 25a depict wind-direction statistics. These graphs show a very good match between predicted and observed wind even capturing those abrupt changes in wind direction such as on June 1st, 8th, and 14th. Note that while the directions appear to be opposite, they are in fact extremely close (since very large angles around 360° and very small angles around 1° represent essentially the same wind direction, as discussed earlier). The wind direction bias (overwhelmingly smaller than 10°) seen in the last graph in Figure 25a, shows very good agreement with observations.

Figures 25b and 25c depict the hourly statistics for temperature and humidity, respectively. As seen in the top graphs in each of these figures, the model captures well the hourly and daily fluctuations, magnitudes, and tendencies in air temperature and humidity. This is also reflected in the other metrics, especially the high values of the IOA (index of agreement).

Figure 25a: Example of hourly model output and MPE (wind speed and direction).

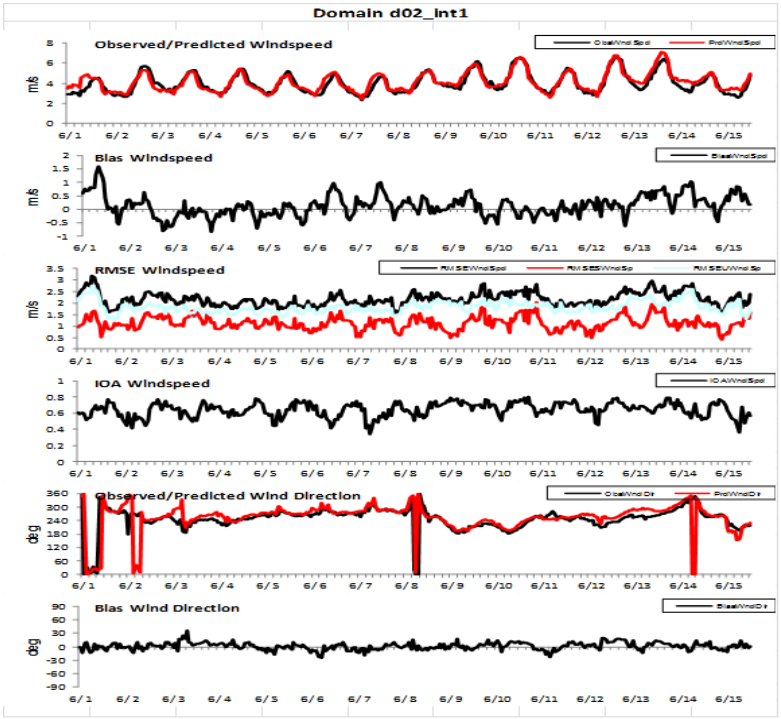

Figure 25b: Example of hourly model output and MPE (temperature).

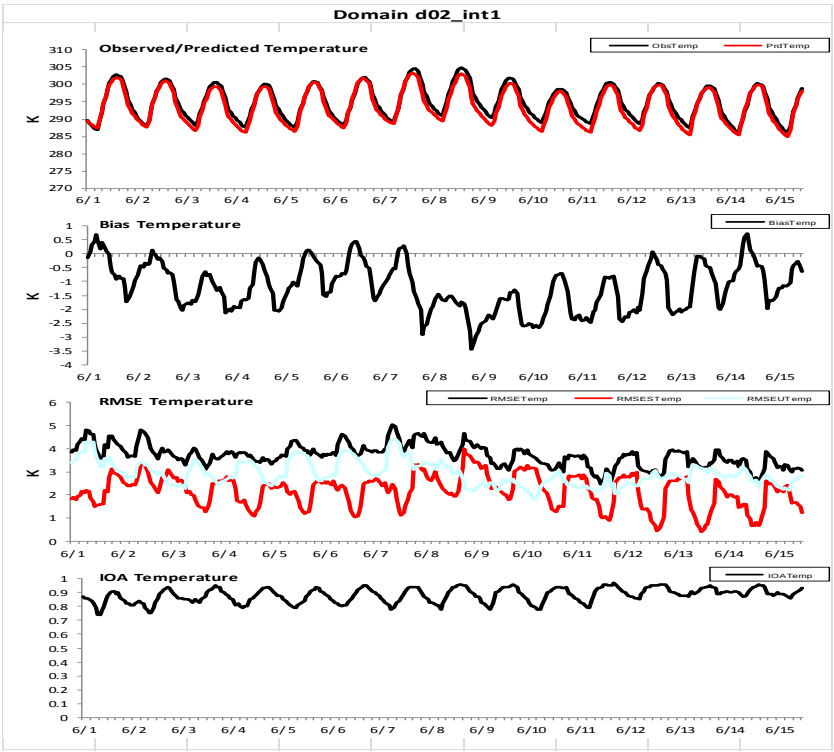

Figure 25c: Example of hourly model output and MPE (humidity).

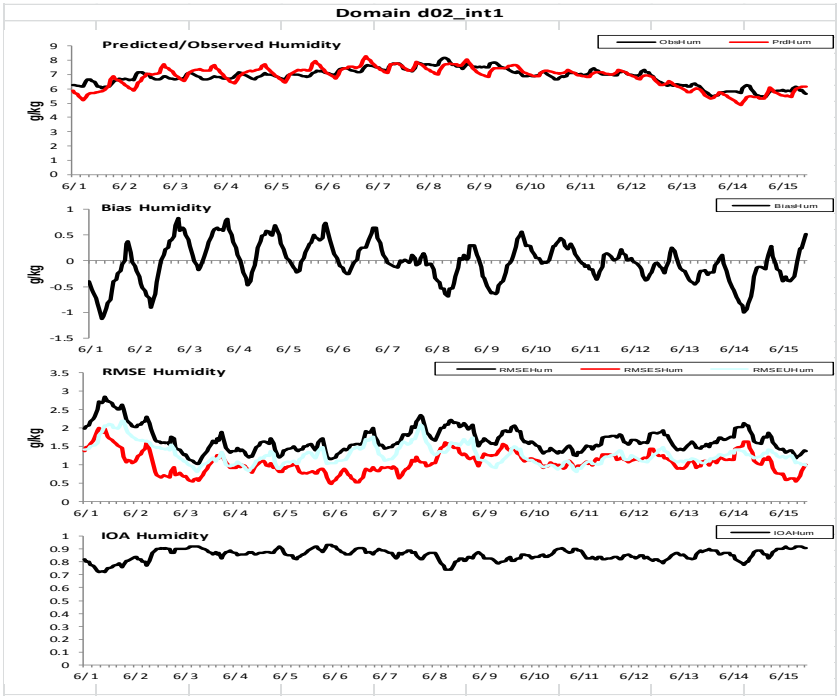

3.5 UHII CALCULATIONS

3.5.1 UHII tiles and UHI reference points

For the purpose of UHII calculations, various regions (UHII tiles) in California were selected based on consideration of several factors including size of urban areas, climate zone, dominant wind direction, topography, and natural barriers. Furthermore, the selection of UHII tiles also depended on whether an urban region is a well-defined island (UI) or a large, continuous archipelago (UA) (Shepherd et al. 2013) as well as the land use / land cover properties in urban and surrounding non-urban areas (Stewart and Oke 2009).

Model output was also perused as guide in selecting UHII tiles and corresponding UHI reference points. Features evaluated from model output included: 1) breaks in the UHI (discontinuities) in each region and 2) lower skin-surface temperatures, both of which are indicative of discontinuities in urban land use. For example, the San Francisco Bay Area archipelago can be broken down into several subzones: 1) the SF Peninsula (Golden Gate bridge to Dumbarton bridge, 2) East Bay (from Pinole to Fremont), 3) San Jose / Santa Clara Valley (areas south of Milpitas and south of Palo Alto), 4) Walnut Creek area, 5) Antioch, and 6) Dublin / Livermore. Similarly, the Los Angeles Basin archipelago can be broken down into 1) west and 2) east basins joined at the cities of San Dimas and Pomona. This is also in part based on the typical daytime penetration of the sea breeze. This area (San Dimas, Pomona, and west of San Gabriel Mountains) was also identified by Boucouvala and Bornstein (2003) as a location where convergence of easterly and westerly flows occurs in the Los Angeles basin (leading to

maximum ozone concentrations in that area). Additionally, the Los Angeles archipelago can be broken down into 3) San Fernando Valley, 4) Mission Viejo, 5) Simi Valley, and 6) Santa Clarita areas.

Another criterion considered when defining UHII tiles and UHI reference points is to minimize the effects of natural, background variations in climate (as also discussed in Section 3.2). This is particularly important in situations where large metropolitan areas cover vast expanses over which the climate varies, for example from west to east (coast to inland) and north to south. Such situations include the San Francisco Bay area with its coastal and inland regions, and the Los Angeles Basin and its coastal and inland desert regions. Other urban expanses in California also exhibit this pattern. To compensate for these effects, the UHII calculation tiles were selected to "break" the continuity, that is, several tiles were used to split large urban areas into smaller zones with their own UHI reference points. This helps minimize the signal from background climate variations.

According to the above general guidelines, several UHII tiles were selected as in Figure 26 and listed in Table 16. The tiles were also selected to encompass a variety of sizes, locations, and climates, which was one of this contract's requirements in choosing a diverse sample of urban areas for calculating the UHII. In addition, Table 16 also lists the dominant wind direction in each UHII tile. This information, along with the UI / UA characterizations discussed above, was used to select UHI reference points in relation to the dominant wind directions within each tile based on wind climatology (e.g., NOAA, www.aviationweather.gov/adds/metars/).

The UHI reference-points selection was additionally constrained to: 1) being part of the same air basin or "catchment" area as the census tracts being characterized, 2) at the same elevation as the census tracts, and 3) at least ~1 km from the downwind edge of urban areas for small areas (for the same reason discussed above in defining UI/UA urban areas) and more for larger areas. However, this is simply a precaution as the UHI reference points are always upwind of the urban area, as discussed in Section 3.2 on static and dynamic selection of UHI reference points. The UHI reference points are shown in Figure 27. The corresponding latitudes and longitudes are also listed in Table A1.

Figure 26: UHII-calculation tiles (also listed in Table 16).

Figure 27: UHI reference points

3.5.2 UHII calculation results

The UHII, defined as in Equation 3, was computed for the regions listed in Table 16. It was computed for each census tract in each of these UHII tiles based on reference temperatures from several non-urban points, as discussed in Section 3.5.1. The UHII was first computed for 182 days (JJA 2013 + JJA 2006) and totalized as degree-hours per 182 days (DH/182). A conversion to DH/day is also provided in column 6 of Table 16. As seen in the 5th and 6th columns of the table, there is a range of UHII in each region – the reason being the large number of census tracts and varying microclimates. A population threshold of 50 km^{-2} was applied in calculating and mapping the UHII.

As discussed in Section 2.1, the UHII listed in Table 16 and all subsequent maps in this report is a Level-1 UHII. It is also important to re-iterate that the UHII values were computed with no reference temperature thresholds. That is, the UHII was computed regardless of the absolute ambient air temperature as long as urban temperature was higher than non-urban ones, unlike in some applications where degree-hours are computed above defined temperature thresholds.

In Table 16, the second and third columns provide information on the dominant wind directions for each region based on wind climatology (NOAA/NCDC). The fourth column identifies a region either as an urban island or collection of islands (UI), or as an urban archipelago (UA). Finally the last column in Table 16 represents the temperature difference between the census tracts of higher UHIIs and the tracts of lower UHIIs within each region. Thus the last column is an indicator to the largest (dominant) heat islands in each UHII tile. Since this was computed backward by dividing UHII by 182 days and then by 24 hours, it represents an all-hours, all-times averaged UHI. In the datasets provided with the final report, temperature difference at each census tract is also provided, not only the maximum value as in Table 16.

Of note, the temperature difference for the largest UHI values in the last column in Table 16 does not necessarily occur at the corresponding city named in column 1. We recall, as discussed earlier, that the city name simply refers to a region that typically includes many other urban and non-urban areas. It is also to be noted that this temperature difference is not relative to non-urban open areas, but relative to the urban areas with lower UHII. The usefulness of comparing to another urban area is that it compensates, to some extent, for the onshore warming effects in coastal areas.

Finally, it is important to reiterate that the UHII was computed separately for each tile and was not meshed with UHII from other areas (no common UHI reference points or temperature thresholds were used). In other words, the absolute temperatures cannot be inter-compared across different UHII tiles, but the relative values of the UHII and the largest ΔT can.

Table 16: Urban heat island index (UHII)
(UI: urban island, UA: urban archipelago)

Region	Dominant JJA winds		Type	UHII range DH/182 days (°C.hr/182) (1)(4)	DH/day range (°C.hr/day) (1)(2)(4)	Largest ΔT (C°) (2)(3)
	Dominant 1	Dominant 2				
Davis	SW	S	UI	904 - 6433	5 - 35	1.3
Fairfield	SW		UI	133 - 20477	1 - 113	4.6
Napa	SW	W,S	UI	131 - 12631	1 - 69	2.8
Sacramento	SW	S	UI	640 - 13792	4 - 76	3.0
San Rafael	SE		UI	218 - 7855	1 - 43	1.7
Santa Rosa	SE		UI	116 - 10780	1 - 59	2.4
Fresno	NW		UI	107 - 8446	1 - 46	1.9
Hollister	NW		UI	109 - 4834	1 - 27	1.1
Lodi	W		UI	375 - 3525	2 - 19	0.7
Manteca	NW	W	UI	301 - 9794	2 - 54	2.2
Merced	NW		UI	1032 - 8270	6 - 45	1.7
Modesto	NW	N	UI	251 - 8126	1 - 45	1.8
Morgan Hill	NW		UI	1142 - 7508	6 - 41	1.5
Watsonville	SW	S,SE	UI	1617 - 10895	9 - 60	2.1
Livermore	W		UI	16 - 7142	0 - 39	1.6
Los Banos	NW		UI	718 - 1400	4 - 8	0.2
Newman	NW		UI	2675 - 4106	15 - 23	0.3
San Francisco	NW	W	UA	11 - 22259	0 - 122	5.0
San Jose	NW		UA	418 - 9000	2 - 49	2.0
Vallejo	SW	W,S	UI	202 - 15020	1 - 83	3.4
Walnut Creek	SW	W,NW	UI	214 - 17514	1 - 96	3.9
Antioch	W	SW	UI	180 - 8319	1 - 46	1.9
Bakersfield	NW	N	UI	85 - 6206	0 - 34	1.4
Coalinga	NW	N	UI	730 - 4542	4 - 25	0.9
East Bay	NW		UA	37 - 22089	0 - 121	5.0
Lancaster	SW	W	UI	574 - 4651	3 - 26	0.9
Mission Viejo	SW		UI	13 - 19891	0 - 109	4.6
Oceano	NW		UI	1186 - 7852	7 - 43	1.5
Oceanside	SW		UA	58 - 22717	0 - 125	5.2
Ramona	W	NW	UI	1851 - 5264	10 - 29	0.8
Salinas	W	SW,NW	UI	409 - 5731	2 - 31	1.2
San Diego	W	NW,SW	UA	131 - 22669	1 - 125	5.1
San Fernando	SE		UA	144 - 7668	1 - 42	1.7
San Luis Obispo	NW	W	UI	1636 - 10606	9 - 58	2.0
Santa Clarita	S	W,NW	UI	331 - 4523	2 - 25	1.0
Santa Cruz	SW	S,SE	UI	436 - 7622	2 - 42	1.6
Simi Valley	W	SW,NW	UI	50 - 10735	0 - 59	2.4
Victorville	SE	W	UI	1321 - 3202	7 - 18	0.4
Wasco	NW		UI	391 - 3033	2 - 17	0.6
Los Angeles East	W		UA	15839 – 49352 §	§ 87 - 271	§ 6.0-8.0
Los Angeles West	W (coast)	S,SW,SE	UA	5 – 33153	0 - 182	

Notes on Table 1:

(1) The UHII entries in columns 5 and 6 can be inter-compared vertically in the table, i.e., across regions, but cannot be inter-compared in terms of absolute temperatures (i.e., different reference temperatures).

(2) The UHII (DH/day) and temperature difference appear to be large in some instances because they also include onshore warming and archipelago effects (see Section 4.2)

(3) Largest ΔT (column 7) is between the warmer and cooler urban areas, not with respect to UHI reference points. Rounded to nearest tenth of a degree C. In the submitted datasets, a ΔT is provided for each census tract in every UHII tile.

(4) Rounded to nearest degree C.

§ This assumes that the east Los Angeles basin is continuous in UHII values with respect to west Los Angeles basin. However, if the UHII values for east Los Angeles basin are assumed separate (discontinuous) from west Los Angeles Basin and based on different UHI reference points, then the UHII range for east Basin is 22 – 19180 DH/182 days. Of note, the larger values (>260 in Table 16 and Figures A40, B40, and D40) may not all be representative of the east Los Angeles basin.

The results from UHII calculations are presented in four sets of maps:

- **Appendix A** includes UHII maps for the regions in Table 16 in units of DH/182 days. That is, the UHII is totalized over the entire modeled periods in 2013 and 2006. In this set of maps, the ranges, intervals (bins), and color coding differ from one region to another to allow for better discrimination of the fine-scale UHII variations within each region (at the census-tract scale).
- **Appendix B** contains the same set of maps as in Appendix A, but with the following differences: 1) the UHII is mapped in units of DH/day average (rather than a total of DH/182 days), and 2) similar color codes, ranges, and intervals (bins) are used for all regions in California. As a result, there is less discrimination of the variations in the UHII within each region compared to maps in Appendix A. This set is more useful for general inter-comparison (not absolute) across various areas in the state but less useful for evaluating the variations of the UHII within each region.
- **Appendix C** is similar to Appendix A (in showing total DH/182 days and varying UHII ranges, bins, and color codes), but with the addition of maps from CalEnviroScreen 2.0. For each UHII map, there is a corresponding CalEnviroScreen map to allow for visual comparison of the two sets of indicators. Each pair of maps in Appendix C includes numbers (1-4) to allow for visual geo-referencing between the two maps. In Appendix C, it can be seen that the highest CalEnviroScreen scores also correspond to some high levels of UHII and that in some cases the high UHIIs correspond to the top 5% score.
- **Appendix D** contains the same set of maps as in Appendix B, but with a different, expanded color-coding scale. The reason for including this additional set of maps is to circumvent the difficulty of discriminating the details of UHII variations in each region

while at the same time using common color coding, ranges, and intervals (bins) across all UHII tiles (regions in California).

The UHII spatial patterns can be grouped into 1) small areas, where the UHI is not very well developed and/or small, 2) single-core areas where the UHI is well-developed and can be displaced downwind by the dominant flow in the area, 3) multiple cores, where several well-developed and well-defined UHIs can be seen in a region, and 4) urban archipelagos where the entire area can be considered as one large and relatively uniform UHI. Examples of areas in each category are as follows (in no particular order):

i. Small areas: Hollister, Los Banos, Newman, Napa, Coalinga

ii. Single cores: Fresno, Davis, Fairfield, Lodi, Merced, Morgan Hill, Livermore, Vallejo, Antioch, Bakersfield, Lancaster, Simi Valley, San Diego

iii. Multiple cores: Sacramento, San Rafael, Santa Rosa, Manteca, Modesto, Salinas, Walnut Creek, Oceanside

iv. Archipelagos: San Francisco – South Bay, Santa Clara Valley (San Jose area), East Bay, San Fernando Valley, Los Angeles basin

The majority of areas (UHII tiles) exhibit single- or multi-core characteristics in UHII (types ii and iii). Out of the 41 tiles examined in this report, 29 exhibit this behavior. Another 6 regions exhibit small UHII patterns (type i). Finally, 6 large regions exhibit the archipelago characteristics (type iv) discussed above. More information is provided in Section 4.1.

While a quantitative model performance evaluation (MPE) was carried out to validate the model against observational data from operational-grade monitors (NOAA) throughout California, as was discussed in Section 3.4, the fine-resolution UHII magnitudes and spatial distributions were also compared qualitatively against fine-resolution observed temperatures in each tile (e.g., data from NOAA mesonet, WeatherBug, or Weather Underground monitors). The comparison shows that the UHII patterns are similar to patterns of observed temperatures, including in areas with urban archipelagos, where the UHII's spatial patterns can become somewhat counter-intuitive.

In urban archipelagos that are also coastal regions, the range of UHII is large and so are the map (bin) intervals. Because of that, large swaths of these regions appear as if uniform in UHII values over large portions of the maps (see Figure 28 for west Los Angeles Basin as an example). In reality, however, the model captures variations in temperatures and UHIs at fine scales throughout the regions in addition to the onshore warming and urban archipelago effects. Figure 28 is provided as an example to examine the variations in UHII in arbitrary areas in the west Los Angeles basin. Points (census tracts) numbered 1-5 are in the Compton area, points numbered 6-8 are in Downtown Los Angeles, points 9-11 are in the San Pedro area, and points 12-15 are in the Anaheim-Orange area. These sample census tracts are also listed in Table 17. The purpose is to show that micro-scale variations in small areas are captured by the model despite the sometimes-overriding signal of archipelago and on-shore warming (the numbers assigned here to the census tracts are solely for the purpose of discussing Figure 28 – they are not actual tract ID numbers).

Figure 28: UHII in west Los Angeles Basin

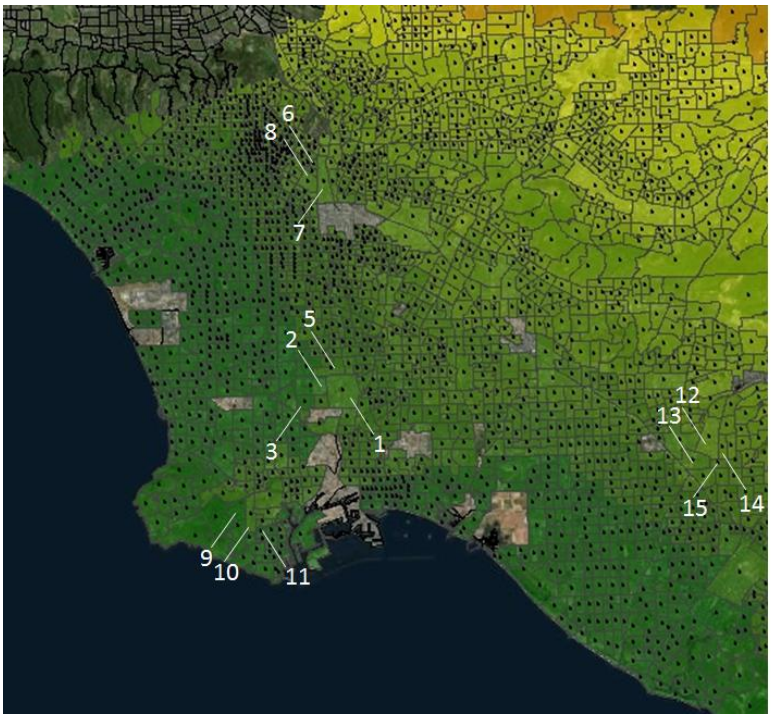

Table 17: Arbitrary samples (microclimate variations) in west Los Angeles Basin (see Figure 28 for tract locations).

Compton			Downtown Los Angeles			San Pedro			Anaheim - Orange		
Tract	DH/day	UHI	Tract	DH/day	UHI	Tract	DH/day	UHI	Tract	DH/day	UHI
1	18.50	0.77	6	40.46	1.68	9	11.44	0.47	12	46.06	1.91
2	13.14	0.54	7	39.80	1.65	10	25.08	1.04	13	37.86	1.57
3	12.48	0.52	8	32.63	1.35	11	19.13	0.79	14	45.74	1.90
4	15.00	0.62							15	40.95	1.70
5	17.38	0.72									

Note: the DH/day and UHI entries are averages over the entire modeled periods.

Among the group of five census tracts in the Compton area, the largest UHII is found at point 1 and the smallest at points 2 and 3. The corresponding average UHIs are 0.77, 0.54, and 0.52°C, respectively. This represents a localized temperature difference (localized UHI) of 0.25°C across a small distance of 1 km or less between these tracts. Tract 1 (with highest UHII) is an industrial-commercial land use, whereas tracts 2 and 3 (lowest UHII) are residential land use with higher vegetation cover than in tract 1.

In Downtown Los Angeles, financial district census tract 6 (high-rise area of downtown) has the largest UHII among the three tracts considered. The high-rise area is 0.33°C warmer than tract 8 (South Park, a commercial area), which is just 1 km to the south. The high-rise area in downtown

is also similar to or slightly warmer than tract 7 (Arts district) despite the latter being 1) downwind of downtown and 2) an industrial-commercial area.

In the San Pedro area, census tract 10 has a larger UHII than tracts to the west of it (tract 9, upwind) as well as to the east of it (tract 11, downwind). Both tracts 9 and 10 are residential, however, tract 9 is lower density development than tract 10 and has significantly higher vegetation cover. Tract 10 is a high-density development with lower vegetation cover. As a result, tract 10 has a larger UHII than tract 9. Tract 11 is near golf courses with slightly higher vegetation cover, and thus is cooler than tract 10. Just a few hundred meters south of tract 11, in a golf-course area, the UHII is 12.75 DH/day and is thus 0.5°C cooler than tract 10 despite being downwind and less than 1 km away.

Furthermore, the Compton area is "counter-gradient" relative to San Pedro. In other words, whereas Compton can be expected to be warmer than San Pedro, due to being further inland, it is actually cooler (thus counter gradient). It is also interesting to note that relative to the west basin's UHI reference points, the downtown area (tract 6) while relatively inland has an average UHI of 1.68°C whereas tract 10 has an average UHI of 1.04°C despite being close to the coast. This highlights the influence of land-use and land-cover properties as well as the ability of the model to detect these fine-scale effects that are embedded within the signal of onshore warming and urban archipelago.

In the Anaheim-Orange area, the largest UHIIs among the four tracts examined as an example are 46.06 DH/day in tract 12 and 45.74 DH/day in tract 14. Relative to the lowest UHII of 37.86 at tract 13, this represents a localized average temperature difference of 0.34°C across a distance of ~1 km. Tract 12 is industrial-commercial with lower vegetation cover than the surrounding tracts and, thus, has the highest UHII. Tract 13 is residential, with significantly larger vegetation cover and, thus, the lowest UHII in this sample area. Tract 14 is also residential and is vegetated but is downwind of tract 12, hence the large UHII, but still slightly smaller than in tract 12. Finally, tract 15 is mixed residential and commercial with significant vegetation cover and, thus, lower UHII.

In urban archipelagos such as Los Angeles basin and Santa Clara Valley, urban heat is continuously injected into an air mass advecting across the urban area (regardless of the compounding effect of on-shore warming). As a result, an air mass warms up continuously, masking localized rises and falls in temperature along the trajectory (Figure 28) even though the model captures the localized fine-scale variations in temperature and UHIs as discussed above. In other words, in areas with one or more urban cores (urban islands, UI, types ii and iii), where built-up density rises towards a central area then tapers off, heat islands also exhibit a core pattern. In archipelagos (UA, type iv), on the other hand, the urban density is sustained and relatively uniform over a large swath of land and, in this case, no clear UHI/UHII core can be detected. In such situations, the highest UHII values are often found near the downwind end of the trajectories. This will be discussed further in Section 4.

These general archipelago effects versus local variations in UHI are also seen in other areas. For example, in the San Francisco peninsula region (Figure A18, B18, and D18) the regional maximum UHII is in the Redwood City area, but the model also shows large variations at the smaller scales as well. For example, Downtown San Francisco is 1°C warmer (localized UHI) compared to an area immediately to its west or north (within a distance of 1 km) e.g., North Beach or Russian Hill. Similarly, Redwood City is an 0.7°C localized UHI relative to San

Carlos, about 1.5 km away. Davis (Figures A1, B1, and D1) is an 0.5°C localized UHI relative to immediate surrounding areas that are 1 – 1.5 km away, even though the regional largest UHII is in Woodlands. Vacaville (Figures A2, B2, and D2) is a 1.5°C local UHI relative to urban areas 3 km away. In the Sacramento region, Carmichael is a 0.7°C localized UHI relative to Rancho Cordova about 2.5 km to the south (Figures A4, B4, and D4). Examples such as these can be seen in almost all urban areas analyzed in this study.

While a number of urban climate archipelagos have been identified, e.g., Figure 29, including both the Los Angeles Basin and the San Francisco Bay Area, quantifying their effects on heat islands and urban climate is not standard procedure and not much prior information is available in this respect. Thus the work performed in this study could be considered as one such attempt at characterizing archipelagos in terms of UHI/UHII. Shepherd et al. (2013) solicit ideas from the research community on how to study and characterize urban-climate archipelagos. This will be discussed further in Section 4 as well.

Figure 29: Example archipelagos in U.S. and international locations.
(source: Shepherd et al. 2013)

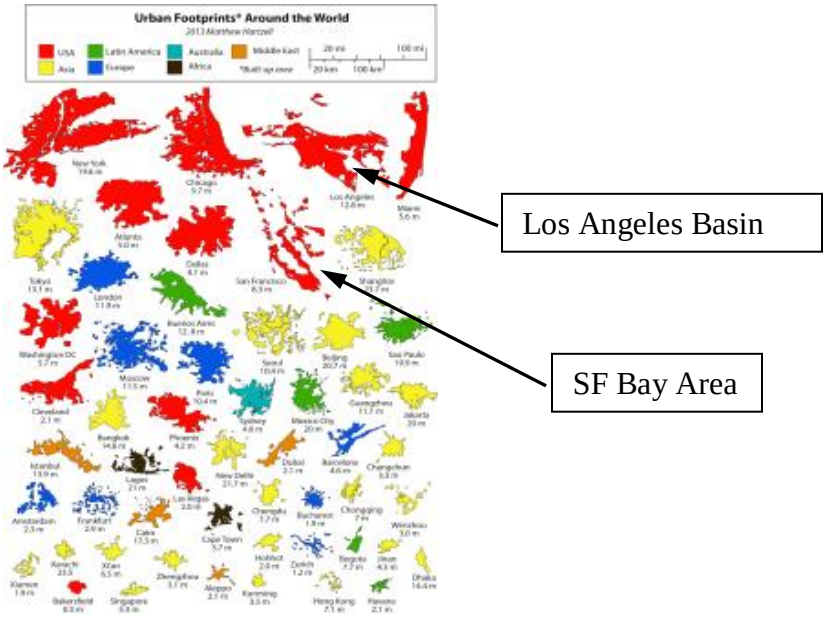

The range of the UHII in each region, e.g., as shown in columns 5 and 6 of Table 16, depends on several factors, including: 1) whether an urban area is an island (UI) or archipelago (UA), 2) the size of the urban area and its built-up density, 3) the characteristics of the surrounding non-urban areas, i.e., whether the surrounds are vegetated, desert, water, etc., 4) whether the area is subject to onshore flow / on-shore warming or damming effects, 5) the length of air-mass trajectories across the urban area, and 6) microclimate characteristics.

It can be seen, in general, that the larger UHII values are associated with larger urban areas and archipelagos (UA). For example, converting UHII into temperature difference (average UHI)

shows that the UA areas have UHIs of up to ~5°C or more caused by the superimposed effects of 1) sustained warming of adverted air masses because of urban heat as well as on-shore heating and 2) the local heat fluxes. The largest UHII values per region associated with the four categories of urban areas defined earlier in this section (based on UHI), are as follows in Table 18. The data suggest that areas with UHI cores (whether single or multiple cores) have generally similar ranges of UHII.

Table 18: UHII ranges

Urban UHI category	UHII range (DH/day)
i small areas	8 - 70
ii single cores	20 - 124
iii multiple cores	45 - 124
iv archipelagos	42 - 270

3.6 DATASETS PROVIDED

In addition to the maps sets in Appendixes A, B, C, and D, datasets resulting from this study were also provided to the CalEPA including calculations of the UHII. The data sets were provided in three main directories:

- Directory **ALL_DATA_182** which contains the results of UHII as total degree-hours over a period of 182 days and the corresponding maps are configured with varying color codes, ranges, and intervals (bins) per each region's specifics.

- Directory **ALL_DATA_DH_Day** which contains maps and datasets of UHII averaged as DH/day and the same color codes, ranges, and bins (intervals) are used across all regions in California.

- Directory **ALL_DATA_DH_Day_2** which contains the same set of maps and datasets as in above directories but with a different and more resolved (expanded scale) color-coding scheme. The purpose of this additional set of data is to provide more detail (better discrimination of UHII variations) within each UHII tile while at the same time using common scale and intervals across all regions in California.

Within each of these main directories, the following sub-directories and data sets were provided. The sub-directories are organized by region name, as follows:

##_<RegionName>, where the number (##) is simply the order of data processing and has no particular meaning. <RegionName> is the name of one of the cities characterized in the corresponding datasets (each contains more than one city) and listed in column 1 of Table 16. Within each directory ##_<RegionName>, the following are provided:

##_<RegionName>_UHII.jpg

This is a JPEG map of the UHII (DH/182 days or DH/day) for the region <RegionName> and other surrounding urban areas in each UHII tile. Each map shows a range (spread) of UHII values and different binning intervals (bin sizes) per the specifics of each region. Each map also shows the census tract boundaries and centroids as well as an inset depicting the location of the map (UHII tile) within the State of California.

<RegionName>_Labels.kmz

This is a Google-Earth-viewable file that projects the census tract code numbers onto a region's map. These codes are study-specific and not FIPS codes. A crosswalk between study-specific codes and FIPS is provided in an Excel spreadsheet for each region (FIPS: Federal Information Processing Standard).

<RegionName>_UHII.kmz

This is an interactive, Google-Earth-viewable script that, when clicking on any census tract in the map, brings up a pop-up window displaying the following information for each tract:

1. Census tract ID (both FIPS and study-specific IDs are provided)
2. Population per km^2 (year 2012)
3. GIS files
4. X- and Y- coordinates of the census-tract centroid both in LCP relative to domain center latitude/longitude (37.0N 120.5W) and in grid points relative to model sub-domain origin (LCP: Lambert Conformal Projection)
5. UHII values (in DH/182 days or DH/day)

<RegionName>_UHII_FIPS_latlon_mask.xlsx

This is an Excel file for each region, containing the following fields for each census tract:

1. ID: Census-tract study-specific ID
2. FIPS: Census-tract FIPS ID
3. Latitude (of tract centroid)
4. Longitude (of tract centroid)
5. LCPx: X-coordinate (m) in Lambert Conformal Projection
6. LCPy: Y-coordinate (m) in Lambert Conformal Projection
7. UHII: UHI Index in DH/182 days
8. UHII in DH/day
9. Average DT for each tract (relative to reference points)

GIS files

Each sub-directory in ALL_DATA_182 also contains various GIS files, shapefiles, and related projection information needed to re-create the maps. In Directory ALL_DATA_DH_Day, the sets are provided within the same directory (no separate sub-directories for GIS files)

4. DISCUSSION

4.1 SPATIAL PATTERNS OF THE UHII

The UHII was calculated based on air-temperature differences that were extracted from dynamically-consistent meteorological fields of an atmospheric model (WRF). As such, the UHII accounts for advection of heat in addition to its local production due to land-use/land-cover properties and interactions with the boundary layer. The model results show that the largest UHIIs are often displaced downwind relative to the urban cores or centers where skin-surface temperature may peak (the latter is often seen in images from airborne or satellite-based thermal sensors). The downwind displacement varies depending on size of urban area, local flow properties, and topographical characteristics. Furthermore, in coastal areas the UHIs (and thus the UHIIs) are also superimposed on the onshore warming of air. Thus the UHIIs in these regions and in urban archipelagos also capture that warming effect. Finally, those urban areas in topographical air basins often have the larger UHIIs closer to downwind physical barriers. All of these factors contribute to differences between the spatial patterns of air-temperature UHII and skin-surface temperature.

In Section 3.5, the modeling results were presented in terms of the UHII, as defined by equation 3. In terms of spatial characteristics, it is possible to qualitatively discern four types of UHII patterns (i to iv), as was alluded to in Section 3.5:

A. Small areas: these are situations where urban areas are relatively small and, thus, UHIs are small and localized. Examples of such small areas can be seen in Figures A8, A16, A17, A24, A27, A31, A35, and A40 (in Appendix A) and their corresponding figures in Appendixes B, C, and D.

B. Single cores: these are relatively larger urban areas where the UHI can develop fully and downwind transport of heat also occurs. However, there is only one core, i.e., one main area where the UHI maximum is defined and thus a single-core UHII can be detected. Examples of such urban areas are seen in Figures A1, A2, A7, A9, A11, A13, A14, A15, A20, A22, A23, A26, A28, A33, A36, A37, A38, and A39 (in Appendix A) and their corresponding figures in Appendixes B, C, and D.

C. Multiple cores: in this case, an urban area is large enough that several UHII cores develop, although each core is still well defined. Examples of such situations can be seen in Figures A4, A5, A6, A10, A12, A21, A29, and A32 (in Appendix A) and their corresponding figures in Appendixes B, C, and D.

D. Archipelagos: In this situation, urban land use covers a large geographical area often demarcated by coastlines or topography (in California). Thus unlike single- or multi-core areas, where there is a clear beginning and end to urban land use with no major topographical barriers (e.g., Fresno, Bakersfield, Sacramento, etc.), archipelagos consist of sustained urban land-use, without interruption. The only discontinuities in the urban expanse occur because of topography. Examples includes the Los Angeles Basin, the Santa Clara Valley (San Jose) and San Fernando Valley, among others. Examples can be seen in Figures A18, A19, A25, A30, A34, and A41 (in Appendix A) and their corresponding figures in Appendixes B, C, and D. Archipelagos produce a different UHII pattern that will be discussed further in Section 4.2.

The UHII is calculated for all selected urban areas and the results are presented in Figures A1-A40, B1-B40, C1-C41, and D1-D40. In each figure, the regional dominant UHII (or maxima, if multiple cores) can be seen representing the largest cumulative effects. However, as discussed in Section 3.5.2, within each UHII tile (within each figure) there are significant variations in the localized UHI and UHII that relate to local variations in land-use/land-cover properties, heat generation and storage, vegetation cover, and so on. The data user can further evaluate these regional and localized variations in the UHI and UHII by clicking on the desired census tracts in the *.kmz files provided with the datasets, as discussed in Section 3.6.

4.2 ARCHIPELAGOS, SURFACE, and AIR TEMPERATURES

Urban archipelagos are continuous, large expanses of urban areas with no discontinuities in urban land use and no downwind urban demarcations, e.g., in the Los Angeles Basin or San Francisco Bay Area, they end at mountains or coastlines. Thus an archipelago acts as one large continuous source of heat and the highest temperatures are generally found downwind.

In the Santa Clara Valley (San Jose), the higher temperatures occur closer to the foothills of the U-shaped valley (Figures A19, B19, and D19). In the Los Angeles area, the higher temperatures are found closer to the northern ranges (e.g., San Gabriel Mountains, San Bernardino Mountains), and further east away from the coastline, i.e., in the east basin (Figures A40, B40, and D40). However, there is also considerable spatial variability in temperature (and variations in UHIs/UHIIs) as discussed in Section 3.5.2.

The archipelago situation is interesting because the spatial pattern of the UHII (no core) can be somewhat counterintuitive. However, while the largest UHII values may occur at the downwind parts of the archipelagos, the model captures the variations in UHI and its change with land use as discussed earlier in Section 3.5. Furthermore, the model also captures variations in skin-surface temperatures. For example, Figure 30 depicts modeled daytime skin-surface temperature in an area of the east Los Angeles Basin for an arbitrary day (August 1st, 2013) at 1400 PDT -- skin-surface heat islands can be seen. The areas of Chino, Pomona, and Fontana are more vegetated relative to some of the higher-density industrial and commercial areas in Ontario and Bloomington. As a result, the latter two areas are warmer (higher skin-surface temperature).

Figure 30: Daytime skin-surface temperature (C°) on arbitrary day, 1 August 2013 at 1400 PDT in the east Los Angeles domain (D10) showing spatial variations in temperature. The dashed line is the location of higher UHII values in this subdomain (see Figures A40, B40, and D40).

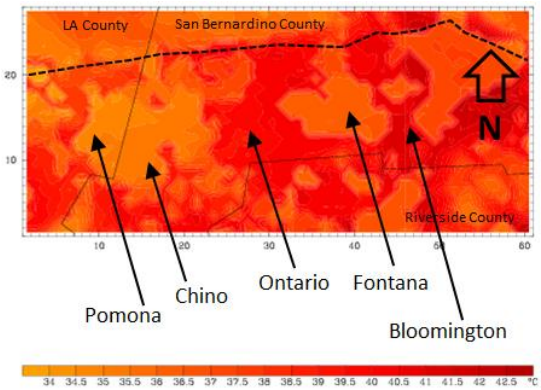

It is clear from Figure 30 that there is no south-to-north gradient in skin-surface temperature UHI (unlike the air-temperature UHII in this area) and that there is considerable spatial variation in all directions. Because air temperature is well-mixed, it peaks downwind, in this case nearer to the mountains (dashed line in Figure 30) and does not reflect the pattern of skin surface-temperature heat islands in this area. Interestingly, other studies (e.g., Sun et al. 2015) indicate that the foothills areas also will experience the higher temperatures in the Los Angeles basin because of climate change through the mid-century.

The model results indicate an average air-temperature difference of 6-8°C (Table 16) between inland areas (e.g., the towns of San Bernardino, Hemet, and Perris) and coastal areas to the east of LAX[5]. Observational and analyzed data from PRISM[6] (Daly et al. 2008), on the other hand, suggest an average temperature difference of 5-7°C between these regions (Figure 31). The reason for the ~1°C discrepancy between modeled and PRISM UHI is the finer resolution of the modeling (1 and 3 km) versus the averaging in the reanalysis of observational data (4 km) as well as the locations of the actual monitors and grids (in PRISM) versus the locations of centroids used in the simulations.

Figure 31. Top: 2006, **bottom:** 2013. Air temperatures at inland and coastal locations based on PRISM data (Daly et al. 2008).

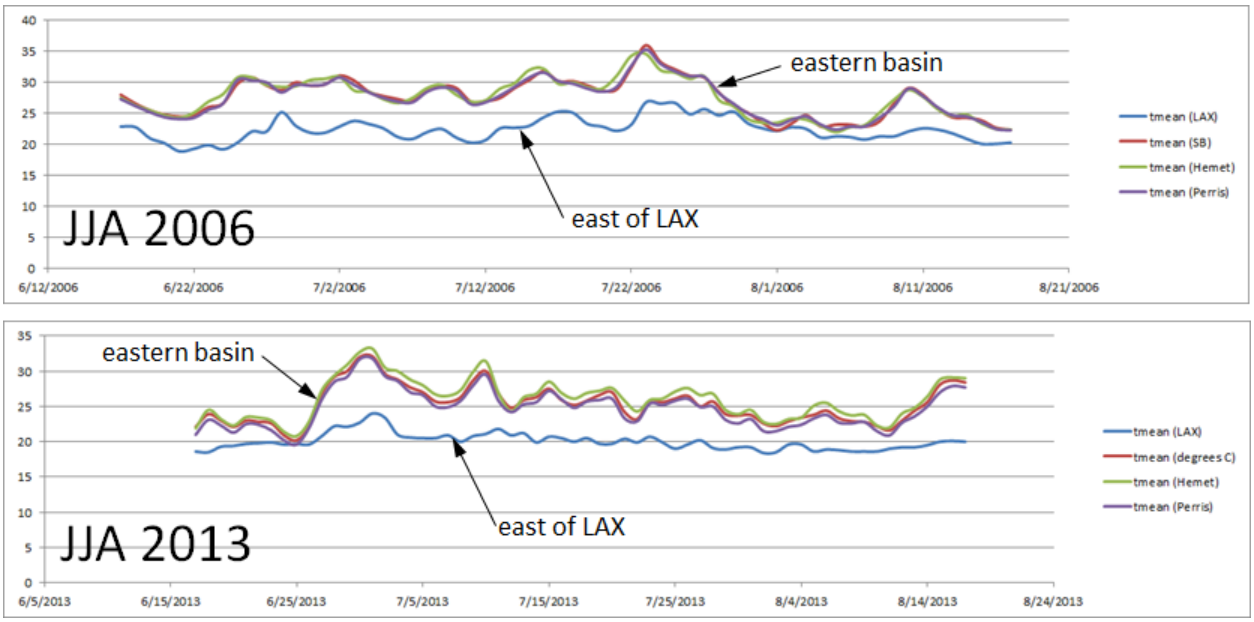

Per Los Angeles Basin climatology, a differential of up to 20°C can exist at times across the basin as a result of varying microclimates and on-shore warming, but differences of 10-15°C are more common. This can be seen, for example, in Figure 31, e.g., around June 27 to July 12 and August 14 to 17, 2013 and between June 22 and July 26, 2006. The average July maximum

[5] The average UHI is computed from the UHII by dividing by 182 days then by 24 hours. Thus the UHI so computed is an average for all hours, day and nighttime, for all days of the simulations.

[6] PRISM: Parameter-elevation Relationships on Independent Slopes Model is based on analysis of observational data based on location, elevation, coastal proximity, topography, and orography (Daly et al. 2008).

temperature in Santa Monica (at the coast) is 24 °C but is 35 °C in Canoga Park, in the San Fernando Valley, a difference of 11°C (WRCC 2015). Thus while the urban archipelago effect on UHII as modeled in this study (6-8°C differential or more) can seem large, it is nevertheless very comparable to the observed temperature differences in the area.

Another factor contributing to inland areas (e.g., east Los Angeles Basin) having larger UHIIs than coastal ones (e.g., west Los Angeles Basin) is fog occurrence in coastal areas during certain times when inland regions are fog-free and thus warmer relative to the UHI reference points than are the coastal areas. It is reiterated again that these effects are important to be accounted for (and are correctly captured by the model) in computing the UHII since the purpose is to characterize the actual heat distribution in each region (Level 1 UHII) as discussed in Section 2.1.

A similar situation also exists in the San Francisco Bay Area. Figure 32 for an arbitrary day (August 1st, 2013) shows the pattern of modeled skin-surface temperature in the San Jose / Santa Clara Valley area (white oval in Figure 32A) as well as the location of the peak UHII values (the U-shaped dashed lines in Figures 32A-32D). It can be seen that, unlike the UHII which is higher at the U-shaped end of the valley (Figures A19, B19, and D19), the core area / downtown San Jose can be warmer during most parts of the day (skin-surface temperature heat island in Figure 32). While skin-surface temperature is relatively uniform early in the day across the valley (figure A), the central area warms up more (Figure B) than surrounding areas and develops a central-core skin-surface UHI. By 1400 PDT (Figure C) the entire valley (corresponding to the oval area) has warmed up (but the core area is still somewhat warmer than its immediate surroundings). By 1700 PDT (Figure D), the U-shaped area (dashed lines) is warmer than some of the central areas in the valley.

On the other hand, air temperature is sustained by transport over the valley and thus the UHII is larger downwind near the U-shaped region. Whereas the UHII indicates that the cities of Cupertino and Milpitas are hotter than central San Jose (Figure A19, B19, and D19), Figure 32 shows that the center core can actually be warmer (skin-surface temperature) at times than the outlying areas (U-shape).

The archipelago versus single/multi-core UHIIs situations are further discussed below and shown schematically in Figure 33. The UHI (ΔT) can be thought of as a having a mean and a deviation (perturbation) component, such that:

$$UHI = \overline{UHI} + UHI' \qquad (16)$$

Figure 32: Daytime skin-surface temperature (C°) on arbitrary day, 1 August 2013, at (A) 0800, (B) 1100, (C) 1400, and (D) 1700 PDT in the Santa Clara Valley (white oval) showing spatial variations in temperature. The dashed, U-shaped lines represent the location of higher UHII values in this subdomain.

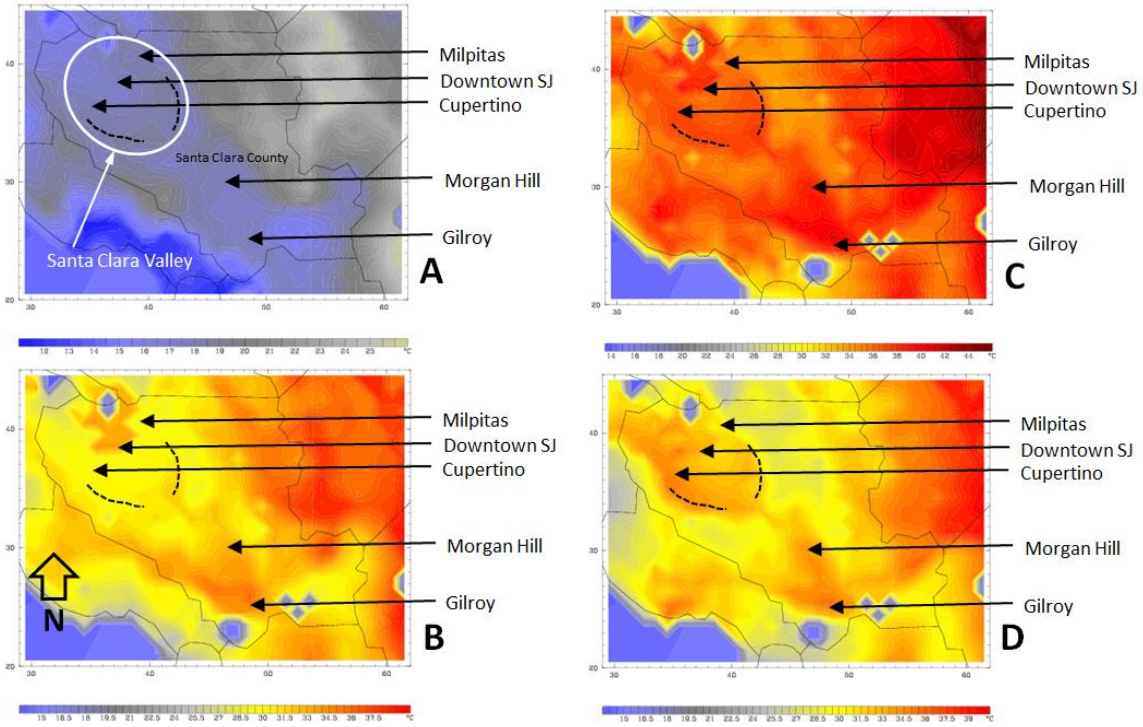

Figure 33: Single/multi core UHIs/UHIIs versus archipelagos

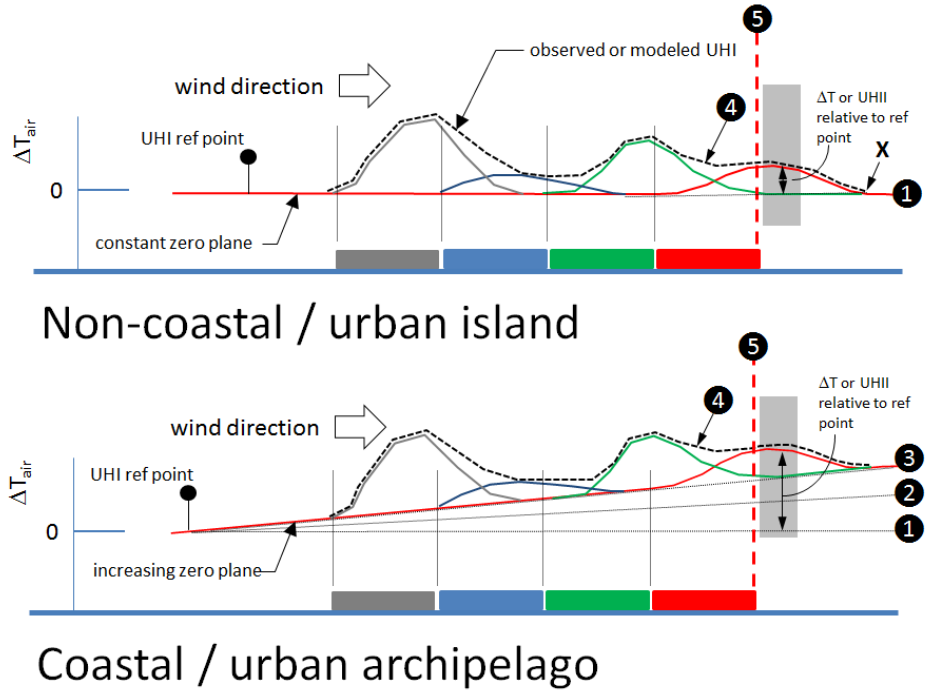

In Figure 33, line 1 in the top graph and line 3 in the bottom graph represent the mean UHI, whereas the multiple colored lines (in both top and bottom graphs) represent the perturbations, that is, the deviations of the local UHI (line 4) from the mean. Relative to the upwind reference temperature (UHI ref point), a "zero plane" is defined (line 1 in top graph, line 3 in bottom graph) which can serve as a reference temperature without urban-archipelago or on-shore warming effects.

In the case of an urban island (UI) as in the top graph, say Fresno, Bakersfield, Sacramento, and other similar areas, the temperature (line 4) returns to the value of the upwind reference point, i.e., the value at the zero plane (line 1) at some distance downwind of the trailing edge of the urban area (the trailing edge is marked with line 5). This tapering-off of the UHI is complete at the point marked with "X" (in the top graph) where conditions are relatively similar to those upwind (i.e., at the UHI ref point). No major topography or other factors exist in this case and the urban area is relatively small. At the trailing edge of the urban area (line 5) there still is a UHI, as seen by the continuous red line and the dashed black line (line 4).

In coastal and/or archipelago situations, such as Los Angeles Basin and Santa Clara Valley (bottom graph of Figure 33), the urban area (archipelago) ends at topographical barriers (thus the archipelago ends at line 5). There is no downwind stretch past this trailing edge of the urban area (line 5) over which temperature can return to upwind values. As a result, the total UHI at that point (line 5 in bottom graph) consists of the following superimposed fields: a) the onshore warming of air from the bay or ocean (line 2 minus line 1), b) upwind urban warming of air by the urban archipelago (line 3 minus line 2)[7] beyond that caused by the local urban land use, and c) the locally-produced UHI (line 4 minus line 3). This explains why the highest UHII values in archipelagos and coastal areas can be found further inland, near the downwind end of the air basin, close to the mountain foothills. Thus at these barriers, which are also the trailing edges of the urban archipelagos (in Los Angeles and San Jose), temperature is larger than in other parts. Thus Line No. 4 (and its increasing reference plane, line 3) in the bottom graph of Figure 33 is what we see in Figure 28, i.e., variations in localized UHIs superimposed on a west-to-east gradient in temperature (line 3).

Thus areas with similar local UHIs (e.g., in the regions highlighted with grey vertical shade in Figure 33) will have a larger UHII in archipelago situations (bottom graph) than in urban islands (top graph) because of the superimposed on-shore warming and archipelago effects. Conversely, an area with a certain UHII in archipelago can have a smaller localized UHI than an area of similar UHII in an urban island situation.

Other implications are that when computing average temperature differences (ΔT) between upwind and downwind parts of urban archipelagos/coastal areas (e.g., last column in Table 16), larger values are obtained than in urban island (UI) situations because they also include the effects of on-shore warming. For example, and as described earlier, the modeled ΔT across the LA basin is 6-8°C. However, and as shown in Figure 33, this ΔT, while correctly characterizing real-world conditions in this area, is not all UHI effect, but includes the effects of onshore warming as well. Only detailed modeling of hypothetical non-urban scenarios can provide an estimate of contributions from different causative factors. This is included in Levels 3 and 4 of

[7] This difference is small in smaller urban islands (and thus may not appear in the top graph) but becomes significantly larger as the length of air-mass trajectory becomes longer (as in archipelagos), thus appears in the bottom graph.

the UHII (Figure 2) and should be addressed in possible follow-on efforts in the future. On the other hand, for example, the average ΔT between upwind and downwind parts in Fresno (1.9°C) is clearly all UHI effect, since the area is inland (no on-shore warming) and also relatively small, thus no archipelago heating exists. This suggests that in UI, the UHII is closer to being a mitigation indicator than in UA where it is solely a characterization of the problem.

The cumulative urban-warming effect of an archipelago is a real part of the UHI and so it is correct to include it in calculating and mapping the Level-1 UHII, as was done in this study. The UHII and the maps produced in this project depict the existing temperature patterns (regardless of causative factors), including the superimposed effects, and thus can help identify areas with relatively larger heat and UHI problems. The UHII, in this case, is proportional to what a thermometer would indicate in the field. However, the on-shore warming component could be subtracted in future efforts (Levels 3 and 4 of the UHII) if the goal is to develop mitigation guidelines and include mitigation potentials in the UHII. The archipelago effect should also be subtracted if the goal is to develop a *localized* mitigation UHII.

4.3 UHII AND THE BACKGROUND TEMPERATURE

The total degree-hours per period (absolute, not differences) at each UHI reference point in each UHII tile were averaged per day and then averaged over all reference points per tile. This produced a single DH/day average for each UHII tile which was then used as an indication to background climate and absolute air-temperature variations in different regions and time periods as shown in Table 19. To conserve space in Table 19, several regions were grouped together by relative proximity or similar geography. In this table, each month is split into two halves (1-15 and 16-30 or 31). The variations in microclimates are evident. From the warmest to coolest, the regions can be crudely ranked as follows:

	DH/day range*
South central valley	600-800
South inland	600-700
South coast	500-650
Center central valley	500-600
San Francisco Bay Area	400-600
North bay	400-500
West central	350-500

* Absolute temperatures (not differences)

In all areas, the 2006 heat wave (second half of July 2006) is seen as the highest temperatures in Table 19 (some areas have other equally hot periods).

Table 19: Absolute-temperature DH/day (°C.hr day^{-1}, averaged over UHI reference points in each UHII tile) for various regions. Each month is divided into two half periods (1-15 and 16-30, or 31).

SF Bay Area

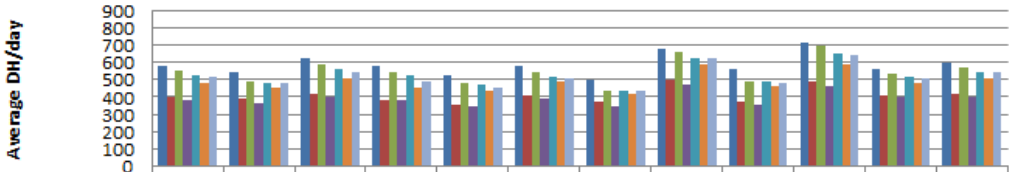

	2013 Jun	2013 Jun	2013 Jul	2013 Jul	2013 Aug	2013 Aug	2006 Jun	2006 Jun	2006 Jul	2006 Jul	2006 Aug	2006 Aug
Antioch	577	540	626	575	527	582	498	674	565	717	563	597
East Bay	403	390	414	381	355	407	372	498	375	486	410	419
Livermore	554	491	588	545	478	540	437	661	488	694	535	572
San Francisco	378	361	404	379	345	390	348	471	354	459	396	404
San Jose	523	476	564	522	468	516	432	621	486	653	520	541
San Rafael	477	458	505	455	432	485	420	586	463	590	480	508
Walnut Creek	517	482	540	487	454	511	438	625	477	641	504	542

South central valley

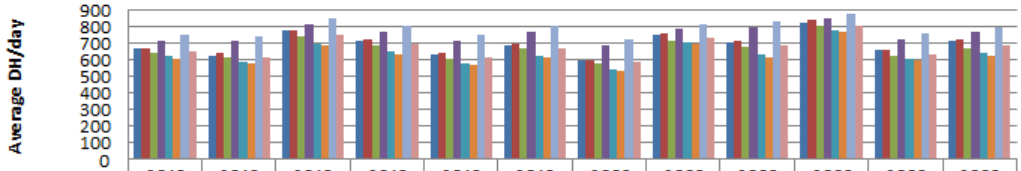

	2013 Jun	2013 Jun	2013 Jul	2013 Jul	2013 Aug	2013 Aug	2006 Jun	2006 Jun	2006 Jul	2006 Jul	2006 Aug	2006 Aug
Bakersfield	669	622	772	711	632	689	596	744	704	824	654	709
Coalinga	670	636	774	719	644	692	596	754	709	839	655	716
Fresno	644	608	738	686	606	667	573	715	671	804	625	669
Lancaster	707	708	815	767	708	770	686	786	796	849	717	761
Los Banos	617	587	696	645	575	624	540	706	628	775	602	635
Newman	606	576	686	633	563	609	529	696	613	762	595	617
Victorville	752	738	843	799	746	803	725	811	828	873	760	796
Wasco	651	612	752	690	613	668	582	726	685	806	634	686

Center central valley

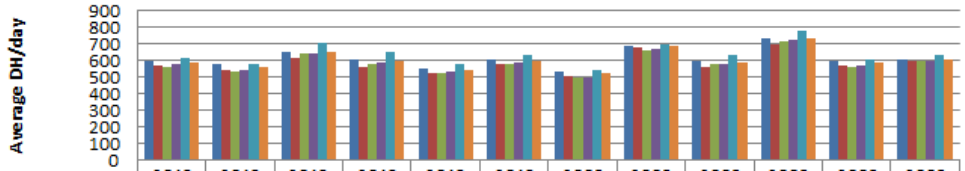

	2013 Jun	2013 Jun	2013 Jul	2013 Jul	2013 Aug	2013 Aug	2006 Jun	2006 Jun	2006 Jul	2006 Jul	2006 Aug	2006 Aug
Davis	589	572	649	601	546	601	526	685	589	732	588	603
Fairfield	566	542	607	554	518	572	498	673	555	695	565	592
Lodi	560	530	635	574	525	570	493	656	571	708	560	588
Manteca	572	541	640	586	530	582	497	663	571	722	563	589
Merced	612	578	703	652	573	627	538	692	630	773	597	626
Sacramento	581	561	650	594	541	594	516	680	586	730	582	605

Table 19: Continued

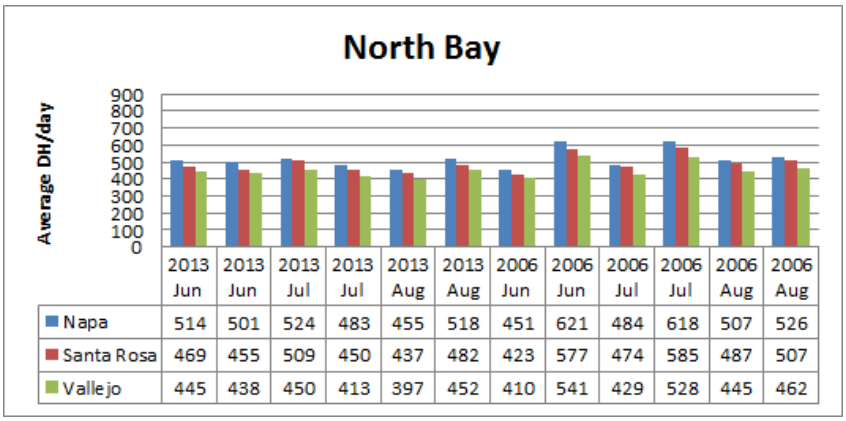

	2013 Jun	2013 Jun	2013 Jul	2013 Jul	2013 Aug	2013 Aug	2006 Jun	2006 Jun	2006 Jul	2006 Jul	2006 Aug	2006 Aug
Napa	514	501	524	483	455	518	451	621	484	618	507	526
Santa Rosa	469	455	509	450	437	482	423	577	474	585	487	507
Vallejo	445	438	450	413	397	452	410	541	429	528	445	462

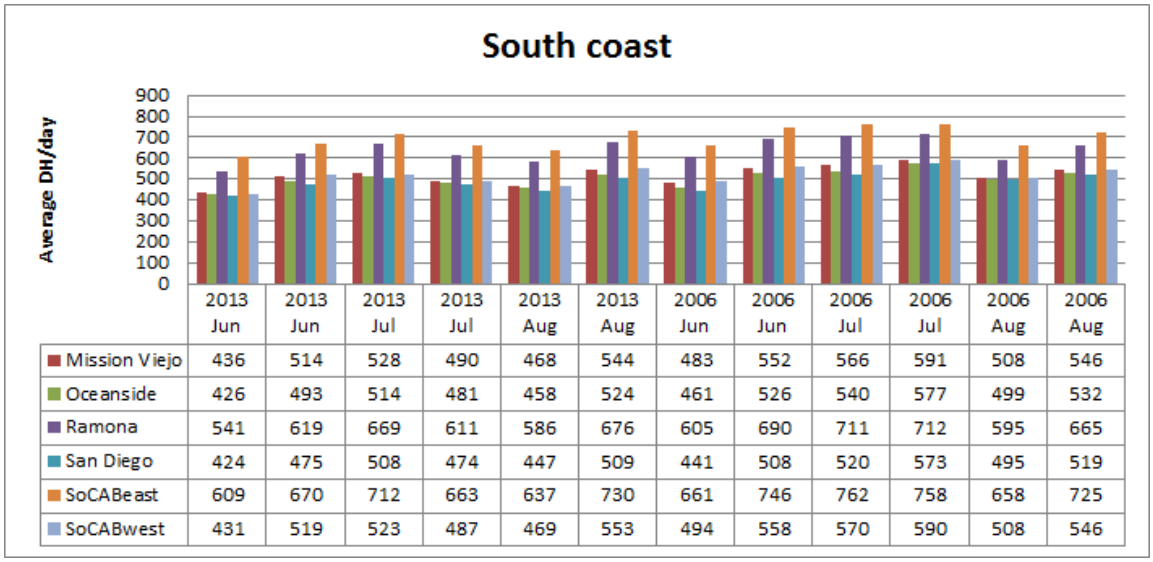

	2013 Jun	2013 Jun	2013 Jul	2013 Jul	2013 Aug	2013 Aug	2006 Jun	2006 Jun	2006 Jul	2006 Jul	2006 Aug	2006 Aug
Mission Viejo	436	514	528	490	468	544	483	552	566	591	508	546
Oceanside	426	493	514	481	458	524	461	526	540	577	499	532
Ramona	541	619	669	611	586	676	605	690	711	712	595	665
San Diego	424	475	508	474	447	509	441	508	520	573	495	519
SoCABeast	609	670	712	663	637	730	661	746	762	758	658	725
SoCABwest	431	519	523	487	469	553	494	558	570	590	508	546

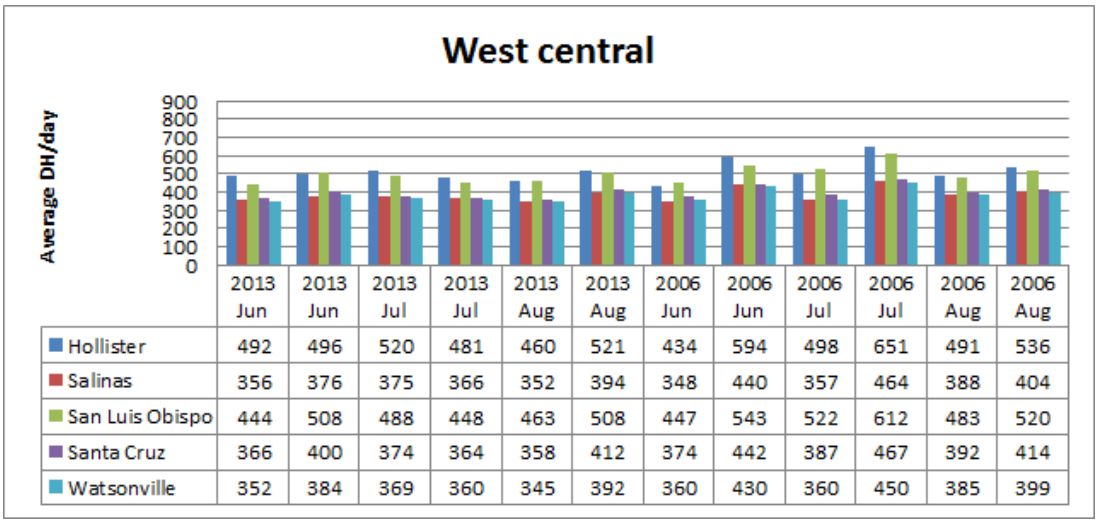

	2013 Jun	2013 Jun	2013 Jul	2013 Jul	2013 Aug	2013 Aug	2006 Jun	2006 Jun	2006 Jul	2006 Jul	2006 Aug	2006 Aug
Hollister	492	496	520	481	460	521	434	594	498	651	491	536
Salinas	356	376	375	366	352	394	348	440	357	464	388	404
San Luis Obispo	444	508	488	448	463	508	447	543	522	612	483	520
Santa Cruz	366	400	374	364	358	412	374	442	387	467	392	414
Watsonville	352	384	369	360	345	392	360	430	360	450	385	399

Table 19: Continued

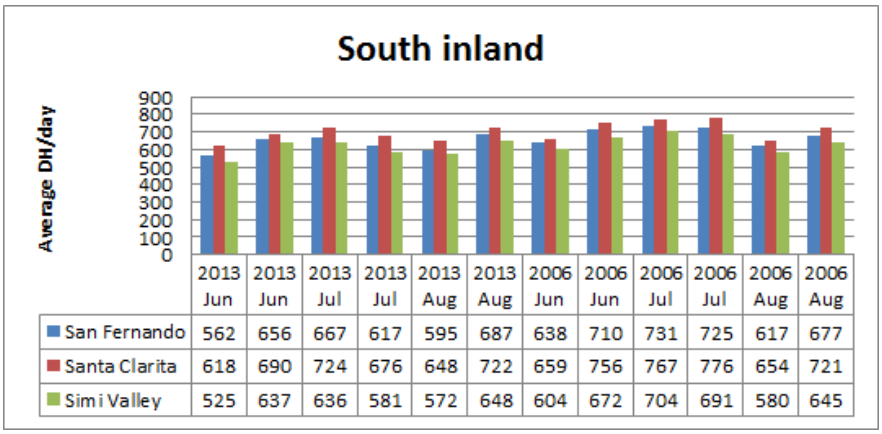

	2013 Jun	2013 Jun	2013 Jul	2013 Jul	2013 Aug	2013 Aug	2006 Jun	2006 Jun	2006 Jul	2006 Jul	2006 Aug	2006 Aug
San Fernando	562	656	667	617	595	687	638	710	731	725	617	677
Santa Clarita	618	690	724	676	648	722	659	756	767	776	654	721
Simi Valley	525	637	636	581	572	648	604	672	704	691	580	645

To evaluate whether the UHII pattern is any different during the hotter weather, model results were evaluated further and an arbitrary sample of regions is presented in Figure 34. In the left part of each of these figures, the average DH/day for each region's reference points is shown for the JJA periods in 2013 and 2006 (from Table 19) and is used here as a cumulative indicator to and in lieu of instantaneous absolute air temperature. The 2006 heat wave can again be seen (red arrows).

On the right side of each figure, two frequency distributions are shown: one for the 2006 heat wave (red line, corresponding to red arrow) and another for the period with lowest average DH/day in each region (blue line, corresponding to blue arrow). Thus the blue frequency-distribution line in the right part of each figure corresponds to the coolest period in each region which is indicated with a blue arrow in the left part of the figure. In the right part of the figures, the horizontal axis represents the UHII bins (in increments of 10 DH/day) and the vertical axis is the frequency distribution of these UHII bins in each region, that is, the percentage of census tracts within given UHII bins. Of note, each of the cooler and heat-wave periods are 2 weeks long and the coolest periods differ across the regions (see blue arrows in Figure 34). Thus there is sufficient variability in the selected sample and should be statistically representative of a range of conditions.

It can be seen in Figure 34 that the warmer weather shifts the UHII distribution towards larger values compared to the cooler periods. For example in Fresno, about 30% of tracts in the UHII bin of 20 DH/day are shifted to the 30 DH/day bin. The 50 DH/day bin containing 5% of tracts in the cooler weather contains 18% of the tracts during the heat wave.

In Livermore, the 40 DH/day bin contained 14% of tracts during the cooler period, but 22% during the heat wave. This was shifted from the lower bin of 30 DH/day which contained 24% of tracts in cooler weather but decreased to 17% of tracts in the heat wave. In Sacramento, significant shifts occur such that the bin at 70 DH/day contained 0% of tracts during the cooler period but increased to 19% of tracts during the heat wave. The distribution of tracts in other bins also changed with some increasing and others decreasing.

In San Diego, the shift occurs through a range of bins but noticeably the number of tracts in the 20 DH/day is reduced and shifted to the higher bins. Those bins of 110-140 DH/day contained 0% census tracts in the cooler period that increased to 4% of the tracts (in each of these bins)

during the heat wave. In San Francisco, the census tracts in bin 10 DH/day were reduced from 72% to 54% and shifted to higher bins, such that bins 110-180 DH/day, containing 1% of tracts during the cooler periods, increased to 3-5% of the tracts during the heat wave. In Vallejo, census tracts in bins 40-60 DH/day were shifted to bins 70 and 80 DH/day, and the bins 90-120 DH/day that contained 0% of the tracts in the cooler period increased to 8-18% of the tracts during the heat wave.

In Antioch, bins were shifted upwards such that bin 50 DH/day, containing 0% of tracts during the cooler weather, contained 14% of tracts during the heat wave. In the East Bay, all bins smaller than 50 DH/day were shifted to bins higher than 50 DH/day. Furthermore, bins 120-170 DH/day containing 0% of tracts during cooler periods increased to contain 2-4% of the tracts in heat-wave conditions. In Fairfield, most tracts in the 10 DH/day bin were shifted to the 20 DH/day bin during the heat event. In addition, bins 90-140 DH/day with 0% tracts in cooler weather, increased so as to contain 2-6% of the tracts during heat wave conditions. In Manteca, tracts in bins 10 and 20 DH/day were shifted to higher bins, such that bins 30-60 DH/day contained larger numbers of census tracts under the heat wave conditions. Significant changes and shifts in the UHII are also seen in other regions, including the Lancaster and Mission Viejo areas. See Figure 34 and Table 20.

In the Los Angeles urban archipelago, the hotter weather also increases the number of census tracts affected by high UHII, but the pattern is slightly different from those in the regions discussed above. For example, in east Los Angeles Basin, the heat wave causes an increase in the number of census tracts in the mid-range bins of 150–210 DH/day, but a decrease in census tracts at both tail ends of the main distribution (the smaller distribution between 0 and 20 DH/day does not change). The number of census tracts in bins greater than 210 DH/day and in those bins smaller than 120 DH/day is reduced, such that the frequency distribution has a slightly smaller spread. That is, the archipelago has a slightly more uniform temperature field (a smaller temperature differential across the basin).

Coastal regions with deep basins and large catchment areas, such as Los Angeles and the Santa Clara Valley, are more complex than inland or other smaller coastal areas. The slight reduction in the higher UHII values in Los Angeles (discussed above) can be attributed to an effect similar to “reverse coastal cooling”, a term coined by Bornstein and co-workers (Lebassi et al. 2011). This occurs when inland areas, particularly basins, warm up (e.g., during heat waves) and thus strengthen the sea breeze to some extent. The stronger venting, in turn, decreases the temperature differential across the archipelago/basin. A similar effect is also seen in Santa Clara Valley (San Jose). Prior studies have identified and quantified a reverse coastal cooling effect albeit on longer time scales, e.g., Lebassi et al. (2011), in both the Los Angeles Basin and the San Francisco Bay Area / Santa Clara Valley. A more recent study of Texas (Liu et al. 2015) found that warming caused by climate change has increased venting in the Houston region.

In this UHII study, however, it is not being suggested that the area becomes cooler (absolute temperatures are predominantly higher during the heat wave), but that the temperature becomes slightly more uniform across the archipelago/basin, that is, a smaller temperature differential across the region results because of the stronger venting. While this may only be a non-dominant, temporary mechanism, it can still affect the shape of the frequency distributions somewhat in these coastal areas.

Table 20 summarizes the changes presented in Figure 34 and includes other regions as well. In the table, the light orange-colored columns are the UHII bins (in DH/day), CP: cooler period, HW: heat-wave period, and the percentages in the tables are the percentages of census tracts in a region that fall in the given UHII bins. The SoCAB East region is split into two columns because of the greater range of UHII values.

The results examined in this section suggest that the warmer weather can increase the UHI and shifts the UHII to larger values. This a result of 1) reduced winds and mixing under high pressure systems (except in coastal basins to some extent) as explained above, 2) lower urban moisture content than in non-urban areas, which under such conditions allows urban areas to warm up more, and 3) reduced cloudiness / increased solar radiation (Taha 2007,2011).

Larger UHIs in warmer weather have also been reported in other regions. For example, Li and Bou-Zeid (2013) used observational data from Baltimore, MD, to show that heat waves increase the UHI intensity because of low urban surface moisture and wind speeds. Their data show that the 2008 heat wave increased the nighttime UHI from 0.5°C to 2.5°C and the daytime UHI from 0.25°C to 1.5°C. Li et al. (2015) also use observational data from China to show that heat waves increase the UHI. Thus if warmer weather increases the UHI, then mitigation measures such as cool cities will become more important in the future (Georgescu et al. 2014) when heat waves are expected to become more frequent.

On the other hand, other studies seem to suggest that UHIs could decrease with higher background temperatures on the long term, e.g., Lemonsu et al. (2013). Thus, again, this highlights the region-specific nature of urban climates and heat-island response to changes in background weather and synoptic conditions.

Figure 34. Left: DH/day average at UHI reference points (each month is divided into two halves: 1-15 and 16-30 or 31). **Right:** frequency distribution of census tracts in UHII bins for the selected periods.

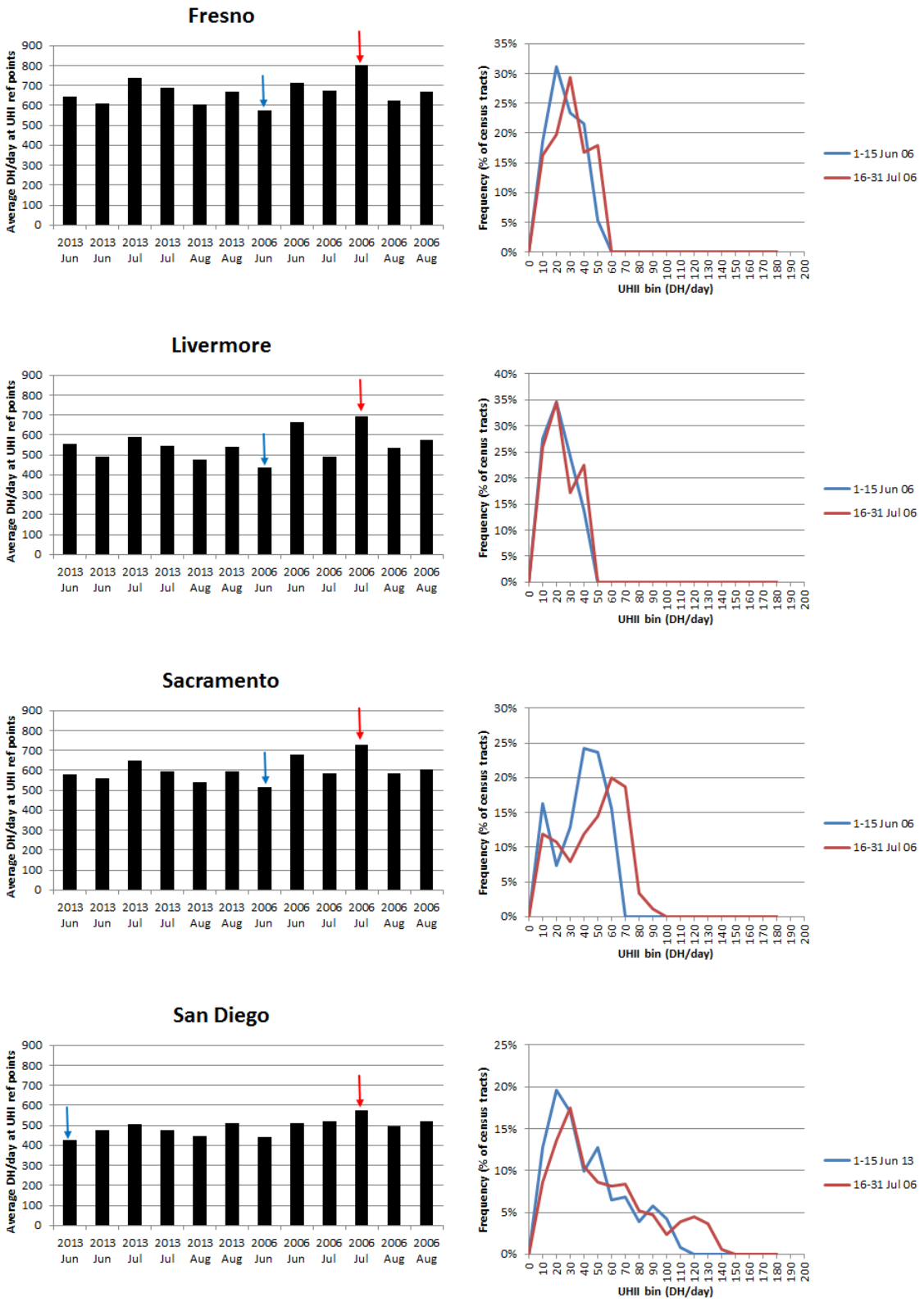

Figure 34: Continued

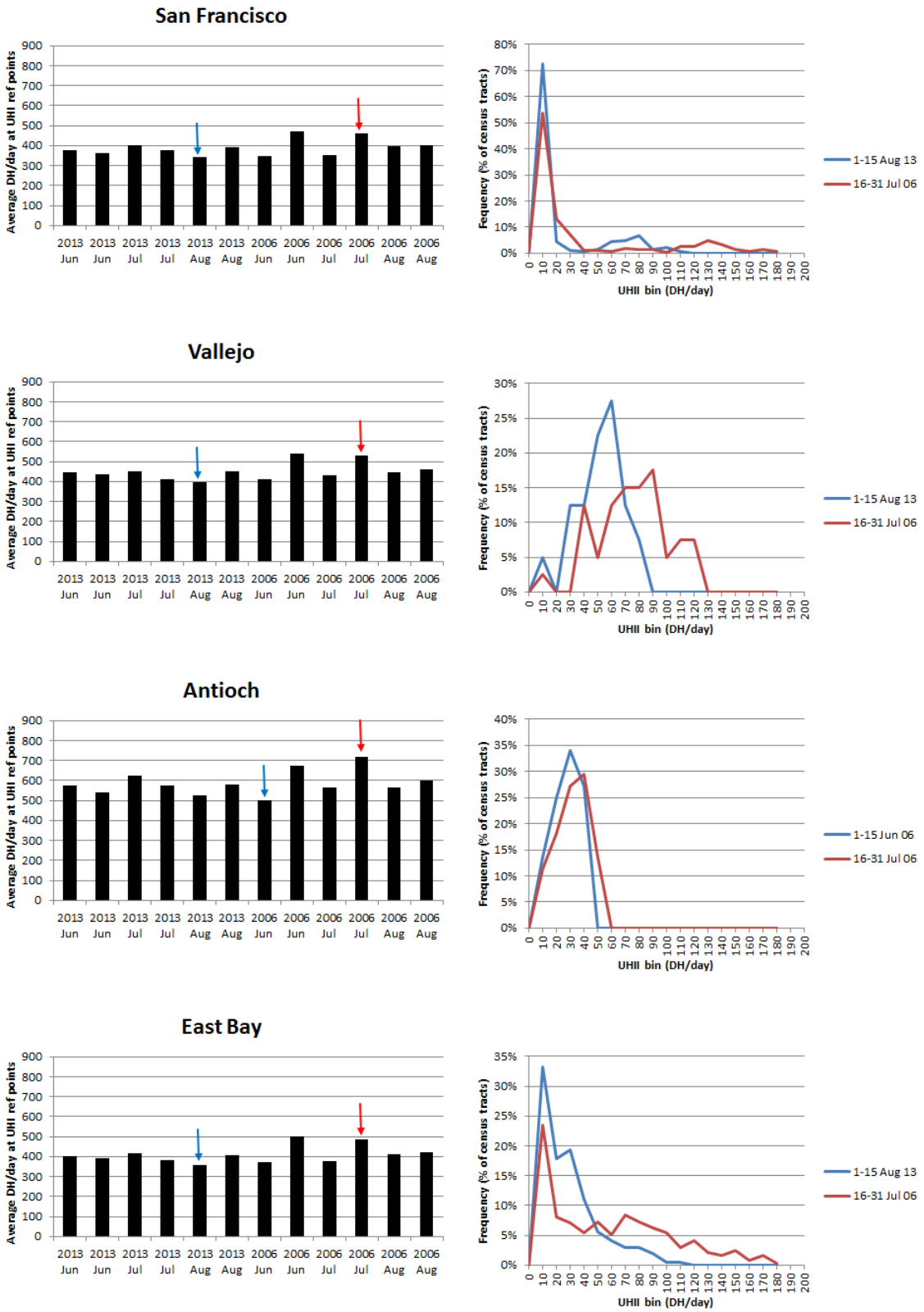

Figure 34: Continued

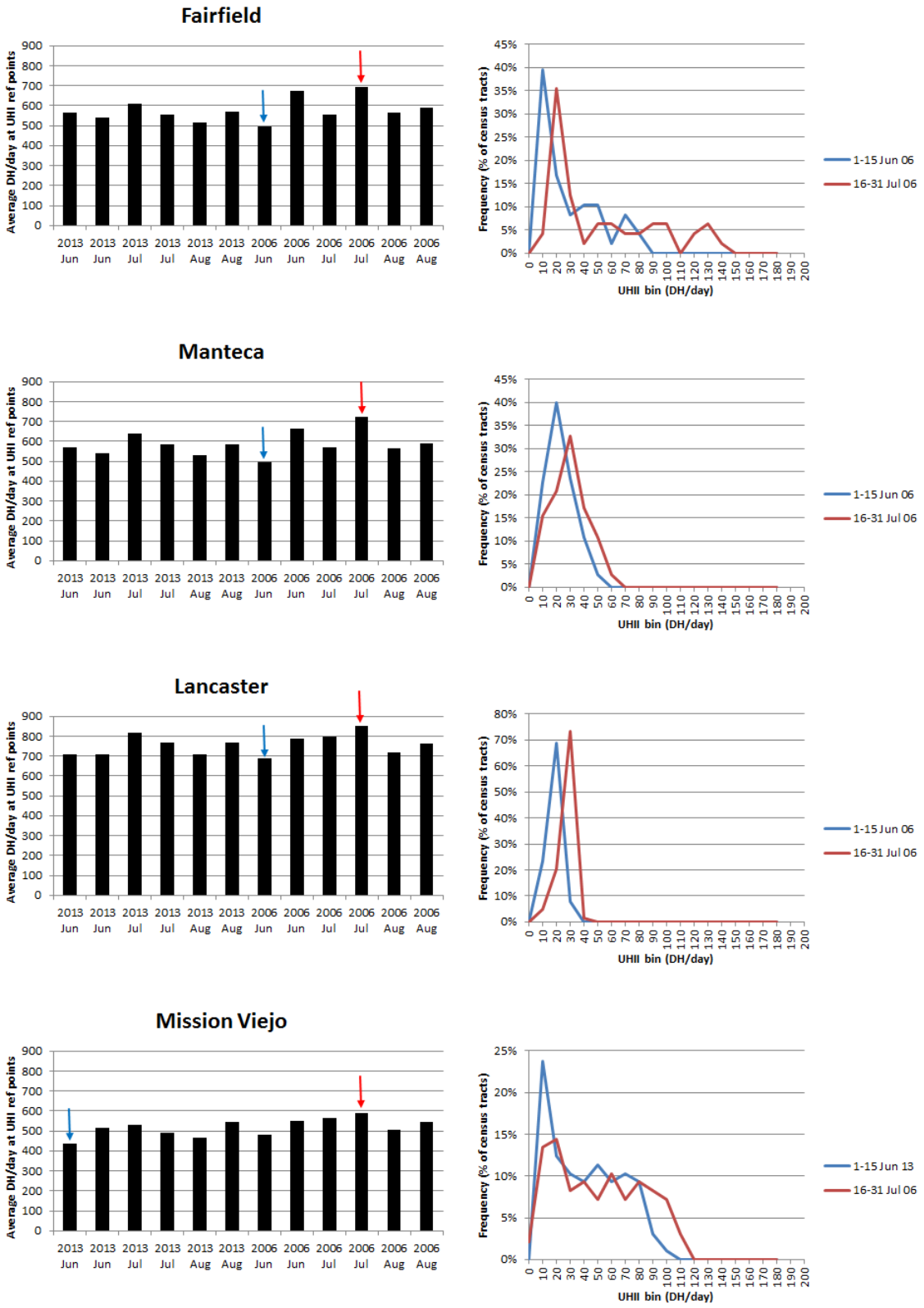

Figure 34: Continued

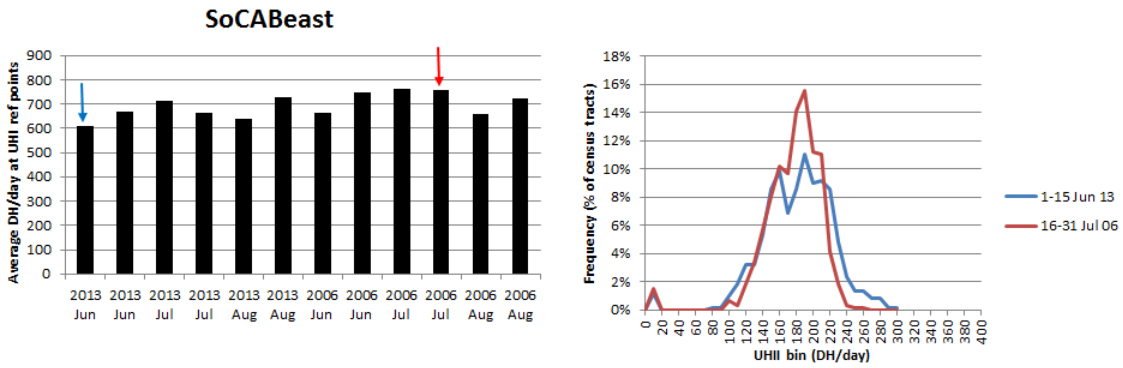

Table 20: DH/day average at UHI reference points (orange) and frequency distribution of census tracts (% of tracts) in UHII bins. CP: coolest period (blue arrow), HW: heat wave period (red arrow).

UHII bin (DH/day)		Antioch		East Bay		Fairfield		Fresno		Lancaster	
		CP	HW	CP	HW	CP	HW	CP	HW	CP	HW
0		0%	0%	0%	0%	0%	0%	0%	0%	0%	0%
10		14%	11%	33%	23%	40%	4%	19%	16%	23%	5%
20		25%	18%	18%	8%	17%	35%	31%	20%	69%	20%
30		34%	27%	19%	7%	8%	13%	23%	29%	8%	73%
40		27%	30%	11%	5%	10%	2%	22%	17%	0%	2%
50		0%	14%	6%	7%	10%	6%	5%	18%	0%	0%
60		0%	0%	4%	5%	2%	6%	0%	0%	0%	0%
70		0%	0%	3%	8%	8%	4%	0%	0%	0%	0%
80		0%	0%	3%	7%	4%	4%	0%	0%	0%	0%
90		0%	0%	2%	6%	0%	6%	0%	0%	0%	0%
100		0%	0%	1%	5%	0%	6%	0%	0%	0%	0%
110		0%	0%	1%	3%	0%	0%	0%	0%	0%	0%
120		0%	0%	0%	4%	0%	4%	0%	0%	0%	0%
130		0%	0%	0%	2%	0%	6%	0%	0%	0%	0%
140		0%	0%	0%	2%	0%	2%	0%	0%	0%	0%
150		0%	0%	0%	2%	0%	0%	0%	0%	0%	0%
160		0%	0%	0%	1%	0%	0%	0%	0%	0%	0%
170		0%	0%	0%	2%	0%	0%	0%	0%	0%	0%
180		0%	0%	0%	0%	0%	0%	0%	0%	0%	0%

Table 20: Continued.

UHII bin (DH/day)	Livermore		Manteca		Mission Viejo		Sacramento		San Diego	
	CP	HW	CP	HW	CP	HW	CP	HW	CP	HW
0	0%	0%	0%	0%	0%	2%	0%	0%	0%	0%
10	28%	26%	23%	15%	24%	13%	16%	12%	13%	9%
20	34%	34%	40%	21%	12%	14%	7%	11%	20%	14%
30	24%	17%	24%	33%	10%	8%	13%	8%	17%	17%
40	14%	22%	11%	17%	9%	9%	24%	12%	10%	10%
50	0%	0%	3%	11%	11%	7%	24%	14%	13%	9%
60	0%	0%	0%	3%	9%	10%	16%	20%	7%	8%
70	0%	0%	0%	0%	10%	7%	0%	19%	7%	8%
80	0%	0%	0%	0%	9%	9%	0%	3%	4%	5%
90	0%	0%	0%	0%	3%	8%	0%	1%	6%	5%
100	0%	0%	0%	0%	1%	7%	0%	0%	4%	2%
110	0%	0%	0%	0%	0%	3%	0%	0%	1%	4%
120	0%	0%	0%	0%	0%	0%	0%	0%	0%	4%
130	0%	0%	0%	0%	0%	0%	0%	0%	0%	4%
140	0%	0%	0%	0%	0%	0%	0%	0%	0%	1%
150	0%	0%	0%	0%	0%	0%	0%	0%	0%	0%
160	0%	0%	0%	0%	0%	0%	0%	0%	0%	0%
170	0%	0%	0%	0%	0%	0%	0%	0%	0%	0%
180	0%	0%	0%	0%	0%	0%	0%	0%	0%	0%

UHII bin (DH/day)	San Francisco		San Jose		Vallejo		SoCAB East				
	CP	HW	CP	HW	CP	HW	CP	HW	DH/day	CP	HW
0	0%	1%	0%	0%	0%	0%	0%	0%	190	11%	16%
10	72%	54%	7%	33%	5%	3%	1%	2%	200	9%	11%
20	4%	13%	30%	19%	0%	0%	0%	0%	210	9%	11%
30	1%	7%	36%	18%	13%	0%	0%	0%	220	9%	4%
40	1%	1%	24%	9%	13%	13%	0%	0%	230	5%	2%
50	1%	1%	4%	12%	23%	5%	0%	0%	240	2%	0%
60	4%	1%	0%	5%	28%	13%	0%	0%	250	1%	0%
70	5%	2%	0%	3%	13%	15%	0%	0%	260	1%	0%
80	7%	2%	0%	1%	8%	15%	0%	0%	270	1%	0%
90	1%	1%	0%	0%	0%	18%	0%	0%	280	1%	0%
100	2%	0%	0%	0%	0%	5%	1%	1%	290	0%	0%
110	1%	3%	0%	0%	0%	8%	2%	0%	300	0%	0%
120	0%	3%	0%	0%	0%	8%	3%	2%			
130	0%	5%	0%	0%	0%	0%	3%	3%			
140	0%	4%	0%	0%	0%	0%	5%	6%			
150	0%	2%	0%	0%	0%	0%	9%	8%			
160	0%	1%	0%	0%	0%	0%	10%	10%			
170	0%	2%	0%	0%	0%	0%	7%	10%			
180	0%	1%	0%	0%	0%	0%	9%	14%			

5. SUMMARY AND CONCLUSIONS

Urban heat islands (UHIs), where and when they occur, can *locally* exacerbate the effects of regional and global climates on environmental aspects impacting public health including heat, emissions, and air quality. This exacerbation can have further detrimental implications during heat events and heat waves. UHIs cause increased cooling-energy demand, increased emissions of anthropogenic and biogenic gaseous air pollutants and particulate matter, accelerated photochemical production of ozone, and deterioration of air quality.

Because of these potential negative effects, cities and states are considering the development of policies and tools to mitigate UHIs, beginning with a more accurate assessment of their spatio-temporal properties. This effort was commissioned by the CalEPA with the goal of characterizing the UHI via detailed meteorological modeling of various regions in California. The UHI Index (UHII) was then computed based on dynamically-consistent model output. The objective of this study is to develop the UHII as a measure to quantify the impacts of urban areas on air temperature, among other meteorological variables, relative to background, non-urban conditions. That is, the proposed UHII is an indicator to the exacerbation of heat by urban areas, as measured by the urban-nonurban temperature differential.

The scope of the study was to characterize the problem as is, i.e., to characterize and quantify the UHI and compute the UHII with no additional indicators to potentials for mitigation or deployment of control measures; nor does the Level-1 UHII calculated in this study indicate whether mitigation measures will result in positive (beneficial) or negative (inadvertent) effects locally. The latter issues can be addressed with implementation-oriented modeling (UHII Levels 3-4 discussed in this report) and are left for possible follow-up efforts in the future.

In this study, a definition of the UHII was first developed. Following Cal/EPA's approval of the definition, the modeling system was prepared for this application. Several stages and tasks were completed in this study including 1) preparing and generating the needed surface and atmospheric input data, 2) characterizing the land use and land cover at fine resolutions, 3) updating, modifying, and customizing the model parameterizations and urban representations in meteorological models, 4) performing quantitative evaluation of model performance, 5) applying the models and calculating the UHII for every census tract in selected urban areas, and 6) analyzing the results and characterizing and mapping the UHII.

The UHI (and hence the UHII) was computed for each tract relative to dynamically-selected UHI reference points in each region. That is, the UHI temperature-reference points were allowed to vary in time depending on wind approach direction for each hour in each region. The UHII was calculated for each census in terms of 1) total degree-hours (DH) over the modeled seasons (June, July, August 2013 and 2006), 2) DH per day averages, and 3) other metrics. In addition, the UHII spatial patterns were analyzed and grouped into small, large, inland, urban archipelago, and coastal areas, as well as single or multiple-core UHIs. The UHII was also characterized under typical summer conditions during the selected periods as well as during excessive heat events such as the 2006 heat wave to evaluate whether the hotter weather modifies the UHI intensity and the UHII distribution.

Because of the large number of census tracts analyzed and because of the varying microclimates in California, there is correspondingly a large range of UHI and UHII values in different regions. At the lower end of the scale, in smaller urban regions, the UHII ranges from 2 to 20 DH/day (°C.hr/day) whereas in larger urban areas (archipelagos), it reaches up to 125 DH/day or more.

The largest averaged temperature difference (UHI) in each region, ranges from 0.5 – 1.0°C in the smaller urban regions and up to 5°C or more in the largest ones (up to 8-10°C in eastern Los Angeles basin). The larger values typically occur across large urban archipelagos / coastal areas and are caused by the combined effects of 1) sustained warming of advected air because of urban heat as well as on-shore warming and 2) the local heat production.

The range of UHII in each region depends on several factors, including: 1) whether an urban area is an island (UI) or archipelago (UA), 2) the size of the urban area and its built-up density, 3) the characteristics of the surrounding non-urban areas, 4) whether the area is subject to onshore flow / on-shore warming or damming effects, and 5) microclimate characteristics. The modeling shows that, in general, the larger UHII values are associated with larger urban areas and coastal archipelagos (UA).

To evaluate whether hotter weather imparts any effects on the UHI intensity (and UHII), frequency distributions of census tracts in UHII bins (DH/day) were evaluated under heat wave conditions (July 15-31, 2006) and cooler periods in each region. The results of the analysis indicate that hotter weather shifts the distribution towards higher UHIs (and UHIIs) compared to the cooler periods.

For example in Fresno, the hotter weather impacts the UHI such that about 30% of tracts in the UHII bin of 20 DH/day in cooler periods are shifted to the 30 DH/day bin. The 50 DH/day bin contained 5% of tracts in the cooler weather but that increased to 18% of the tracts during the heat wave. In Livermore, the 40 DH/day bin contained 14% of tracts in the cooler period, but 22% of tracts during the heat wave. This was shifted from a lower bin of 30 DH/day which contained 24% of tracts in cooler weather but decreased to 17% of tracts in the heat wave. In Sacramento, significant shifts occur, such that the bin at 70 DH/day contained 0% of tracts during the cooler weather but increased to 19% of tracts during the heat wave. In the San Francisco Peninsula, the census tracts in bin 10 DH/day are reduced from 72% to 54% and shifted to higher bins, such that bins 110-180 DH/day, that contained 1% of tracts during the cooler periods, contain 3-5% of the tracts during the heat wave. In coastal archipelagos and basins, such as the Los Angeles Basin and the Santa Clara Valley, the hotter weather causes stronger venting in the area and thus a more uniform UHII distribution across the basin during the heat wave. In the report, these and other regions are discussed in detail.

Results from this study are presented in maps, time series, tabulations, as well as 3-dimensional meteorological model output. One set of maps includes UHII for each region in units of DH/182 days, that is, the UHII totalized over the entire modeled periods in 2013 and 2006. The range, intervals (bins), and color coding differ from one region to another to allow for better discrimination of the fine-scale UHII variations within each region (at the census tract scale). A second set contains maps of UHII in units of DH/day average (rather than a total of DH/182 days), and similar color codes, ranges, and intervals (bins) were applied to all regions. A third set includes maps from CalEnviroScreen 2.0 to allow for qualitative comparison of the UHII spatial characteristics and intensities against scores form CalEnviroScreen 2.0 for each region. A fourth set includes maps similar to the second set but with an extended color-coding scale for better discrimination of the UHII.

Datasets were provided electronically including the UHII data, Google-earth-compatible data files, Excel spreadsheets, GIS shapefiles, and 4-dimensional meteorological model output in GRIB format.

6. RECOMMENDATIONS AND FUTURE RESEARCH

The modeling completed in this study was for the sole purpose of characterizing the UHI under existing conditions and quantifying the UHII accordingly (Level – 1 characterization, discussed in the report) including superimposed effects of onshore warming and urban archipelagos where they occur. As such, the UHII presented in this report simply is a characterization of the UHI in various urban areas in California and does not include indicators to technical or mitigation potentials or information on whether mitigation measures will result in net positive (beneficial) or negative effects in each region. This study does not propose mitigation measures or suggest certain control strategies, nor does it assess their effectiveness.

The analysis shows that the UHI and UHII are shifted to larger values under conditions of warmer weather (heat wave). Thus the potentially more frequent occurrences of heat waves in future climates could enhance UHIs and further exacerbate the health effects of hot weather. From this perspective, it is important to continue research in 1) evaluating and quantifying the synergies between background weather, urban climates, and heat islands, 2) quantifying the potential exacerbation of UHIs by regional climate change, 3) evaluating the implications in terms of heat and air quality health, and 4) assessing the potential of mitigation measures (such as cool cities) in offsetting some or all of these negative effects, and evaluating the added importance of such measures in future years.

Some of the recommendations that can be made for possible future follow-up efforts include:

a) Build upon the methodologies, models, and modeling techniques developed and applied in this study to carry out modeling of Levels 2 through 4 of the UHII to determine local potentials for mitigation and develop area-specific control measures. These higher UHII levels were defined and discussed in the report.

b) Refine the modeling of coastal basins / urban archipelagos, namely, the Los Angeles Basin and the Santa Clara Valley, by increasing the resolution of the simulations further, e.g., 200 – 500 m, and using specialized techniques and urbanized modules of the atmospheric models discussed in this report. The goal is to isolate the localized UHI signal from the compounding effects of on-shore warming and upstream urban areas so as to develop a correlation between UHI and land-use/land-cover properties at the site-specific, sub-kilometer scale. This will also be important for Levels 3 and 4 UHII characterizations for implementation purposes and assignment of mitigation potentials among various census tracts and cities.

c) Apply the study-updated fine-resolution urban parameterizations data to characterize the urban heat island length scales (fetch effects of urban areas) for use in developing deployment-specific UHII.

d) Further evaluate and study the synergies and dynamics between UHI and heat waves, or hot weather in general, e.g., exacerbation of UHI, and quantify the shift to higher UHII during heat wave conditions and under potential climate change scenarios. This is to ensure that a larger sample (than used in this study) of diverse warmer and cooler periods is considered when developing such correlations and formulating related conclusions.

7. REFERENCES

Adachi SA, Kimura F, Kusaka H, Inoue T, Ueda H, 2012. Comparison of the impact of global climate changes and urbanization on summertime future climate in the Tokyo metropolitan area. Journal of Applied Meteorology and Climatology, 51, 1441-1454 doi: 10.1175/JAMC-D-11-0137.1

Akbari H, Rose S, Taha H, 1999. Characterizing the fabric of the urban environment: A case study of Sacramento, California. Lawrence Berkeley National Laboratory report LBNL-44688, Berkeley, California.

Anderson JR, Hardy EE, Roach JT, Witmer RE, 2001. A land use and land cover classification system for use with remote sensor data. USGS Professional Paper 964, U.S. Government Printing Office, Washington, DC.

Ban-Weiss GA, Woods J, Levinson R, 2014. Using remote sensing to quantify albedo of roofs in seven California cities, Part 1: Methods. Solar Energy. In Press.

Bornstein RD, 1968. Observations of the urban heat island effect in New York City. Journal of Applied Meteorology, 7, 575-582.

Bornstein RD, Johnson DS, 1977. Urban-rural wind velocity differences. Atmospheric Environment, 11, 597-604.

Bornstein RD, 1995. Wind climate in cities. Book Review, American Meteorological Society, 76, 1826-1828.

Bornstein R, Lin Q, 2000. Urban heat islands and summertime convective thunderstorms in Atlanta. Atmospheric Environment, 34**,** 507-516.

Boucouvala D, Bornstein D, 2003. Analysis of transport patterns during an SCOS97 NARSTO episode. Atmospheric Environment, 37, 73-94.

Bougeault P, Lacarrere P, 1989. Parameterization of orography-induced turbulence in a mesobeta-scale model. Monthly Weather Review, 117, 1872 – 1890.

Burian SJ, Han WS, Velugubantla SP, Maddula SRK, 2003a. Development of gridded fields of urban canopy parameters for Models-3/CMAQ/MM5. Department of Civil and Environmental Engineering, University of Utah.

Burian S, Han WS, Brown M, 2003b. Morphological analyses using 3-D building databases: Houston Texas. Department of Civil and Environmental Engineering, University of Utah.

Carter M, Shepherd M, Burian S, Jeyachandran I, 2012. Integration of Lidar Data into a Coupled Mesoscale–Land Surface Model: A Theoretical Assessment of Sensitivity of Urban–Coastal Mesoscale Circulations to Urban Canopy Parameters. Journal of Atmospheric and Oceanic Technology, 29, 328-346 doi: 10.1175/2011JTECHA1524.1

Chen F, Kusaka H, Bornstein R, Ching J, Grimmond CSB, Grossman-Clarke S, Loridan T, Manning K, Martilli A, Miao S, Sailor D, Salamanca F, Taha H, Tewari M, Wang X, Wyszogrodzki A, Zhang C, 2010. The integrated WRF/urban modeling system: development, evaluation, and applications to urban environmental problems. International Journal of Climatology doi:10.1002/joc.2158.

Ching J, Brown M, Burian S, Chen F, Cionco R, Hanna A, Hultgren T, McPherson T, Sailor D, Taha H, Williams D, 2009. National urban database and access portal tool, NUDAPT. Bulletin of the American Meteorological Society doi:10.1175/2009BAMS2675.1

Daly C, Halbleib M, Smith JI, Gibson WP, Doggett MK, Taylor GH, Vurtis J, Pasteris PP, 2008. Physiographically sensitive mapping of climatological temperature and precipitation across the conterminous United States. International Journal of Climatology doi: 10.1002/joc.1688

Dudhia J, 1993. A non-hydrostatic version of the Penn State/NCAR mesoscale model: Validation tests and simulation of an Atlantic cyclone and cold front. Monthly Weather Review, 121, 1493-1513.

DuPont S, Mestayer PG, Guilloteau E, 2005. Parameterization of the urban water budget with the submesoscale model. Journal of Applied Meteorology and Climatology, 45, 624 – 648.

Dupont S, Otte T, Ching J, 2004. Simulation of meteorological fields within and above urban and rural canopies with a mesoscale model. Boundary-Layer Meteorology, 113, 111-158

Fan H, Sailor DJ, 2005. Modeling the Impacts of Anthropogenic Heating on the Urban Climate of Philadelphia: A comparison of implementations in two PBL schemes. Atmospheric Environment, 39, 73-84.

Georgescu M, Morefield PE, Bierwage BG, Weaver CP. 2014. Urban adaptation can roll back warming of emerging metropolitan regions. Proceedings of the National Academy of Sciences 111, 2909-2914 doi: 10.1073/pnas.1322280111

Gershunov A, Cayan DR, Iacobellis SF, 2009. The great 2006 heat wave over California and Nevada: Signal of an increasing trend. Journal of Climate 22, 6181-6203.

Goggins WB, Chan EYY, Ng E, Ren C, Chen L. 2012. Effect modification of the association between short-term meteorological factors and mortality by urban heat islands in Hong Kong. PLoS ONE 7: e38551 doi: 10.1371/journal.pone.0038551

Grell GA, Kuo YH, Pasch R, 1991. Semi prognostic test of cumulus parameterization schemes in the middle latitudes. Monthly Weather Review, 119, 5-31.

Grell GA, Dudhia J, Stauffer DR, 1994. A description of the fifth generation PSU/NCAR mesoscale modeling system (MM5). Technical Note NCAR/TN—379+STR, NCAR.

Grimmond CSB, Oke TR, 1999. Aerodynamic properties of urban areas derived from analysis of surface form. Journal of Applied Meteorology, 38, 1262-1292.

Hong SH, Pan HL, 1996. Nonlocal boundary layer vertical diffusion in a medium-range forecast model. Monthly Weather Review, 124, 2322-2339.

Jacobson M, TenHoeve JE, 2011. Effects of urban surfaces and white roofs on global and regional climate. Journal of Climate doi: 10.1175/JCLI-D-11-00032.1

Janjic ZI. 2002. Nonsingular implementation of the Mellor–Yamada Level 2.5 scheme in the NCEP Meso model. NCEP Office Note, No. 437, 61 pp.

Kalkstein L, Sailor D, Shickman K, Sherdian S, Vanos J. 2013. Assessing the health impacts of urban heat island reduction strategies in the District of Columbia. Report DDOE ID#2013-10-OPS, Global Cool Cities Alliance.

Kalnay E, 2003. Atmospheric modeling, data assimilation, and predictability. Cambridge University Press, 341 p.

Kim Y-H, Baik J-J, 2005. Spatial and temporal structure of the urban heat island in Seoul. Journal of Applied Meteorology, 44, 591-605.

Kistler R, Kalnay E, Collins W, et al., 2001. The NCEP-NCAR 50-year reanalysis: Monthly means CDROM and documentation. Bulletin of the American Meteorological Society, 82, 247-267

Kusaka H, Kondo H, Kikegawa Y, Kimura F, 2001. A simple single-layer urban canopy model for atmospheric models: Comparison with multi-layer and slab models. Boundary-Layer Meteorology, 101, 329-358

Lebassi-Habtezion B, Gonzalez J, Bornstein RD, 2011. Modeled large-scale warming impacts on summer California coastal-cooling trends. Journal of Geophysical Research – Atmospheres, 116 D20, doi: 10.1029/2011JD015759

Lemonsu A, Kounkou-Arnaud R, Desplat J, Salagnac J-L, Masson V. 2013. Evolution of the Parisian urban climate under a global changing climate. Climatic Change 116, 679–692 doi: 10.1007/s10584-012-0521-6

Li D, Bou-Zeid E. 2013. Synergistic interactions between urban heat islands and heat waves: The impact in cities is larger than the sum of its parts. Journal of Applied Meteorology and Climatology 52, 2051-2064 doi: 10.1175/JAMC-D-13-02.1

Li D, Sun T, Liu M, Yang L, Wang L, Gao Z, 2015. Contrasting responses of urban and rural surface energy budgets to heat waves explain synergies between urban heat islands and heat waves. Environmental Research Letters, 10: 054009 doi: 10.1088/1748-9326/10/5/054009

Liang X-Z, Xu M, Yuan X, et al., 2012. Regional climate-weather research and forecasting model. Bulletin of the American Meteorological Society, 93, 1363 – 1387.

Liu L, Talbot R, Lan X, 2015. Influence of climate change and meteorological factors on Houston's air pollution: Ozone case study. Atmosphere, 6: 623 doi: 10.3390/atmos6050623

Lombardo MA. 1985. Ilha de calor nas petropoles o example de Sao Paulo. Editora Hucitec, 244 pp.

Macdonald RW, Griffiths RF, Hall DJ, 1998. An improved method for estimation of surface roughness of obstacle arrays. Atmospheric Environment, 32, 1857–1864

Martilli A, Clappier A, Rotach MW, 2002. An urban surface exchange parameterization for mesoscale models. Boundary-Layer Meteorology, 104, 261-304

Millstein D, Menon S, 2011. Regional climate consequences of large-scale cool roof and photovoltaic array deployment. Environmental Research Letters 6 034001 doi: 10.1088/1748-9326/6/3/034001

Multi-Resolution Land-Characteristics Consortium (MRLC). National Land Cover Databases. http://www.mrlc.gov/nlcd2006.php

OEHHA 2013. California Communities Environmental Health Screening Tool, Version 1 (CalEnviroScreen 1.0) Guidance and Screening Tool. Office of Environmental Health Hazard Assessment Report, Sacramento, California, April 2013, 116 pp. http://oehha.ca.gov/ej/pdf/042313CalEnviroScreen1.pdf

Oke TR, Hannell FG, 1970. Urban Climates. WMO Technical Note 108, 113-126.

Oke TR, 1973. City size and the urban heat island. Atmospheric Environment, 7, 769-779.

Oke TR, 1978. Boundary-Layer Climates. Methuen & Co., Ltd., London.

Pan HL, Mahrt L, 1987. Interaction between soil hydrology and boundary-layer development, Boundary Layer Meteorology, 38, 185-202.

Pleim J, Xiu A, Finkelstein P, Otte T, 2001. A coupled land-surface and dry deposition model and comparison to field measurements of surface heat, moisture, and ozone fluxes. Water, Air, and Soil Pollution, 1, 243-252.

Rose S, Akbari H, Taha H, 2003. Characterizing the fabric of the urban environment: A case study of Greater Houston, Texas. Lawrence Berkeley National Laboratory report LBNL-51448, Berkeley, California.

Rosenfeld A, Akbari H, Taha H, Pomerantz M, 1996. Cool roofs and pavements to help hot smoggy cities. Presented at the ASCE Annual Convention, Washington DC, November 11, 1996.

Rosenzweig C, Solecki WD, Slosberg RD, 2006. Mitigating New York City's heat island with urban forestry, living roofs, and light surfaces, NYSERDA Report 06-06 (June 2006), Albany, New York.

Sailor DJ, Lu L, 2004. A Top-Down Methodology for Developing Diurnal and Seasonal Anthropogenic Heating Profiles for Urban Areas. Atmospheric Environment, 38**,** 2737-2748.

Salamanca F, Martilli A, Tewari M, Chen F, 2011. A Study of the Urban Boundary Layer Using Different Urban Parameterizations and High-Resolution Urban Canopy Parameters with WRF. Journal of Applied Meteorology and Climatology, 50, 1107–1128. doi: http://dx.doi.org/10.1175/2010JAMC2538.1

Shepherd JM, Bounoua L, Mitra C, 2013. Urban climate archipelagos: A new framework for urban impacts on climate. Earthzine http://earthzine.org/2013/11/29/urban-climate-archipelagos-a-new-framework-for-urban-impacts-on-climate/

Skamarock W, Klemp J, Dudhia J, et al., 2008. A description of the Advanced Research WRF. NCAR Technical Note NCAR/TN-475+STR, National Center for Atmospheric Research, Boulder, Colorado.

Stensrud DJ, 2007. Parameterization schemes: Keys to understanding numerical weather prediction models. Cambridge University Press, 459 p.

Stewart I, Oke T, 2009. Newly developed thermal climate zones for defining and measuring urban heat island magnitude in the canopy layer. 8th Symposium of the urban environment, January 10-15, 2009, Phoenix, AZ.

Stoelinga M, 2009. RIP: A program for visualizing mesoscale model output. University of Washington, March 2009.

Sun F, Walton D, Hall A, 2015. A hybrid dynamical-statistical downscaling technique, Part 2: End-of-century warming projections predict a new climate state in the Los Angeles region. Journal of Climate, doi: http://dx.doi.org/10.1175/JCLI-D-14-00197.1

Taha H, 1999. Modifying a Mesoscale Meteorological Model to Better Incorporate Urban Heat Storage: A Bulk-Parameterization Approach. Journal of Applied Meteorology, 38, 466-473.

Taha H, 2001. Potential impacts of climate change on tropospheric ozone in California: A preliminary assessment of the Los Angeles basin and the Sacramento valley. Lawrence Berkeley National Laboratory Report LBNL-46695, Berkeley, California http://escholarship.org/uc/item/5s41x609

Taha H, 2005. Urban surface modification as a potential ozone air-quality improvement strategy in California -- Phase 1: Initial Mesoscale Modeling, Final report prepared by Altostratus Inc. for the California Energy Commission, Sacramento, California, PIER Environmental Research, 169 pp. http://www.energy.ca.gov/2005publications/CEC-500-2005-128/CEC-500-2005-128.PDF

Taha H, 2007. Urban surface modification as a potential ozone air-quality improvement strategy in California -- Phase 2: Fine-resolution meteorological and photochemical modeling of urban heat islands. Final report prepared by Altostratus Inc. for the California Energy Commission, Sacramento, California, PIER Environmental Research. http://www.energy.ca.gov/2009publications/CEC-500-2009-071/CEC-500-2009-071.PDF

Taha H, 2008a. Meso-urban meteorological and photochemical modeling of heat island mitigation. Atmospheric Environment, 42, 8795–8809 doi:10.1016/j.atmosenv.2008.06.036.

Taha H, 2008b. Episodic performance and sensitivity of the urbanized MM5 (uMM5) to perturbations in surface properties in Houston TX. Boundary-Layer Meteorology, 127, 193-218 doi:10.1007/s10546-007-9258-6.

Taha H, 2008c. Urban surface modification as a potential ozone air-quality improvement strategy in California: A mesoscale modeling study. Boundary-Layer Meteorology, 127, 219-239 doi:10.1007/s10546-007-9259-5.

Taha H, 2013a. Meteorological, emissions, and air-quality modeling of heat-island mitigation: Recent findings for California, U.S.A. International Journal of Low Carbon Technologies, doi: 10.1093/ijlct/ctt010

Taha H, 2013b. Multi-episodic and seasonal meteorological, air-quality, and emission-equivalence impacts of heat-island control and evaluation of the potential atmospheric effects of urban solar photovoltaic arrays. Final report prepared by Altostratus Inc. for the California Energy Commission, PIER Environmental Research Program, Sacramento, California. http://www.energy.ca.gov/2013publications/CEC-500-2013-061/CEC-500-2013-061.pdf

Taha H, 2015. Meteorological, air-quality, and emission-equivalence impacts of urban heat island control in California. Invited Paper, Sustainable Cities and Society, doi: 10.1016/j.scs.2015.03.009

Taha H, Wilkinson J, Bornstein R, 2011. Urban forest for clean air demonstration in the Sacramento Federal Non-Attainment Area: Atmospheric modeling in support of a voluntary control strategy. Project final report prepared by Altostratus Inc. for the Sacramento Metropolitan Air Quality Management District (SMAQMD), Sacramento, California.

Tan J, Zheng Y, Tang X, Guo C, Li L, Song G, Zhen X, Yuan D, Kalkstein AJ, Li F, 2010. The urban heat island and its impact on heat waves and human health in Shanghai. International Journal of Biometeorology 54, 75-84 doi: 10.1007/s00484-009-0256-x

Trent RB, 2007. Review of July 2006 heat wave related fatalities in California. California Department of Health Services. http://www.cdph.ca.gov/HealthInfo/injviosaf/Documents/HeatPlanAssessment-EPIC.pdf

Tesche TW, McNally DE, Emery CA, Tai E, 2001. Evaluation of the MM5 model over the Midwestern U.S. for three 8-hour oxidant episodes, Prepared for the Kansas City Ozone Technical Workgroup. Alpine Geophysics LLC and Environ Corp.

Vanos JK, Cakmak S, Kalkstein LS, Yagouti A. 2014. Association of weather and air pollution interactions on daily mortality in 12 Canadian cities. Air Quality, Atmosphere, and Health doi: 10.1007/s11869-014-0266-7

Western Regional Climate Center. http://www.wrcc.dri.edu/narratives/CALIFORNIA.htm. Accessed January 2015.

Zhou L., Dickinson, R.E., Tian, Y., et al. (2003) Comparison of seasonal and spatial variations of albedos from moderate-resolution imaging spectroradiometer (MODIS) and Common Land Model. Journal of Geophysical Research 108: D15 4488 doi:10.1029/2002JD003326

8. GLOSSARY OF ABBREVIATIONS and ACRONYMS

AGL	Above Ground Level
AMSL	Above Mean Sea Level
ARB	Air Resources Board
Archipelago	Urban archipelago is a continuous, very large expanse of urban land use
ARW	Advanced Research WRF
CalEPA	California Environmental Protection Agency
CDPH	California Department of Public Health
Crosswalk	A statistical correlation among different land-use/land-cover categories
DH	Degree-Hours
FDDA	Four Dimensional Data Assimilation
FIPS	Federal Information Processing Standard
hPa	hecto Pascal
JJA	June, July, and August
LBNL	Lawrence Berkeley National Laboratory
LCP	Lambert Conformal Projection
LSM	Land Surface Model
LULC	Land Use / Land Cover
mb	millibar
MPE	Model Performance Evaluation
NCAR	National Center for Atmospheric Research
NCDC	National Climatic Data Center
NLCD	National Land Cover Data
NOAA	National Oceanic and Atmospheric Administration
NOx	Oxides of nitrogen
NUDAPT	National Urban Database and Access Portal Tool
NWS	National Weather Service
O3	Ozone
OEHHA	Office of Environmental Health Hazard Assessment
OPR	Governor's Office of Planning and Research
PM	Particulate Matter
POW	Project Oversight Workgroup
UA	Urban Archipelago
UCI	Urban Cool Island
UCM	Urban Canopy Model
UHI	Urban Heat Island
UHII	Urban Heat Island Index
UI	Urban Island
USGS	United States Geological survey
UTC	Coordinated Universal Time
uWRF	Urbanized WRF model
VOC	Volatile Organic Compound
WRF	Weather Research and Forecasting model

9. APPENDICES

Appendices A, B, C, and D are in separate files.